THE UNIVERSITY OF CHICAGO

MANIPULATING SURFACES AND ARCHITECTURES IN BLOCK COPOLYMER SELF-ASSEMBLY FOR NANOLITHOGRAPHY AND THERMOPLASTIC ELASTOMERS

A DISSERTATION SUBMITTED TO
THE FACULTY OF THE PRITZKER SCHOOL OF MOLECULAR ENGINEERING
IN CANDIDACY FOR THE DEGREE OF
DOCTOR OF PHILOSOPHY

BY
CODY THOMAS BEZIK

CHICAGO, ILLINOIS
JUNE 2021

For Amanda

Constantly regard the universe as one living being, having one substance and one soul; and observe how all things have reference to one perception, the perception of this one living being; and how all things act with one movement; and how all things are the cooperating causes of all things which exist; observe too the continuous spinning of the thread and the contexture of the web.

- Marcus Aurelius, *Meditations*

TABLE OF CONTENTS

LIST OF FIGURES

LIST OF TABLES

ACKNOWLEDGMENTS

Among the many people I am grateful to for supporting me in all the work contained in this dissertation, chief among them is my advisor, Professor Juan de Pablo. Juan has taught me what an ideal researcher looks like - generous, curious, hard-working, and tenacious. I have never left a conversation with Juan feeling like there are no more questions to answer - indeed, I have most often had my eyes opened to just how many more questions could be asked than I previously thought. This spirit of constant inquiry is something I hope to take with me forward into new places and endeavors.

It is also to Juan's credit that he has built a group of so many excellent people. Among the current and former members of the de Pablo group, I am especially grateful to Alec Bowen, Grant Garner, Ashley Guo, Nick Jackson, Joshua Moller, Viviana Palacio-Betancur, and Emre Sevgen. I am very lucky to count all of them among my friends and teachers. In addition, I have learned a great deal from Marat Andreev, Lucas Antony, Yamil Colon, Su-Mi Hur, Elizabeth Lee, Joshua Lequieu, Joshua Mysona, Brandon Peters, Abelardo Ramirez-Hernandez, Phil Rauscher, Daniel Reid, Artem Rumyantsev, Ludwig Schneider, Vikram Thapar, Michael Webb, and Jon Whitmer. I am, once again, extraordinarily lucky to have learned so much from so many.

I have also had the pleasure of closely collaborating with many other groups. Professor Paul Nealey and his group, including Moshe Dolejsi, Jiaxing Ren, and Chun Zhou, have all helped deepen my understanding of the experimental aspects of our work. I was also fortunate to spend several months at IMEC in Leuven, Belgium, where I learned from and worked with Jan Doise, Dustin Janes, and Paulina Rincon-Delgadillo. During this time I also received support from Mentor Graphics, especially Gurdaman Khaira and Andres Torres. Professor Marcus Müller and Professor Ken Schweizer have closely examined much of the work in this dissertation, and I am very grateful for their insight. Professor Stuart Rowan has kindly served on the committee for the defense of this dissertation, and has previously

served on the committee for the defense of my master's thesis at Case Western Reserve University.

This work would not have been possible without the diligent support of many capable administrators at the University of Chicago, including Novia Pagone, Rovana Popoff, Janet Boland, Sandra Marijan, and Heather Crews.

Lastly, my friends and family have been with me throughout this journey, for which I am once again deeply grateful. My mom and dad, Marilyn and Tom Bezik, have always believed in me and given me every opportunity to succeed. I have had many good friends to lean on, especially Jason Ginn, Zachary Kellicut, Nathan Kong, Sonny Li, Adam Schrecengost, and Lucas Service. Most of all, my wife, Amanda Bezik, has made everything I have done possible; without her strength, kindness, and support, I would be lost.

ABSTRACT

The self-assembly of classic diblock copolymers has been known to produce ordered mesophases at the nanoscale. Tailoring this self-assembly for engineering applications, however, requires more than relying on the natural behavior of these systems. The careful manipulation of the geometry and chemistry of surfaces can help guide diblock self-assembly into application relevant morphologies, leading to the potential for the use of block copolymers in nanolithography to produce semiconductor devices. Furthermore, the architecture of the polymer itself can be manipulated beyond the classic diblock to include multi-block and nonlinear motifs, leading to mesophases with larger domains and less regular structure. Such mesophases open the potential for extremely tough yet flexible thermoplastic elastomers. Using simulations, we probe key examples of these phenomena, including the use of diblock copolymers to pattern contact-hole morphologies for lithography and the critical influence of surface chemistry, the role of surface geometry and chemistry in determining the formation and annihilation of defects in line-and-space patterns for lithography, and the behavior of block copolymer thermoplastic elastomers formed from blends of star miktoarm copolymers and homopolymer assembled into the unique "bricks-and-mortar" mesophase.

CHAPTER 1

INTRODUCTION

Linear diblock copolymers (essentially two linear polymer chains of different chemistries covalently bonded together) have a rich phase behavior, by which the balance between the enthalpic incompatibility between the A and B constituents of the chains repel each other, but the overall chain resists adopting overly extended or constrained configurations. This results in microphase separation, typically featuring a periodic structure with a nanoscale dimension. By tailoring the degree of incompatibility and the relative proportion of A and B, different morphologies can be obtained, including spheres, cylinders, gyroids, and lamellae. While this phase behavior is relatively well understood, additional constraints (such as the block copolymers assembling in a thin film and/or in the presence of a surface with its own chemistry) or features (such as multi-block or nonlinear copolymers) can rapidly expand the range of possible phase behavior. Simulations of the phase behavior provide a way to obtain detailed information about the self-assembly process, and help predict or explain possibly experimental behavior, or help design surfaces or architectures to achieve a particular engineering goal. In this dissertation, we explore a variety of specific problems relating to the assembly of block copolymers, and also highlight the phase behavior of nonlinear block copolymers. In particular, we focus on problems of block copolymer self-assembly in or over a pattern defined by optical lithography, a key problem for semiconductor device manufacturing, as well as the problem of making block copolymer thermoplastic elastomers out of nonlinear block copolymers.

In Chapter 2, we explore the thermodynamics and kinetics of block copolymer self-assembly in a cylindrical confinement, often known as a "contact-hole". In the patterning of semiconductor devices, a frequent motif necessary to pattern is a vertical metal connection between two horizontal layers. The adaptation of block copolymer materials to this task involves using conventional lithography to pattern a large "hole", filling the hole with block

copolymer, and letting the block copolymer form a cylinder of much reduced dimensions (the "shrink"). As in most block copolymer lithography, defectivity is of chief concern, as semiconductor devices can tolerate almost no mistakes in the patterning process in order to function properly. Experimental observations, however, suggested that, dependent particularly on the chemical patterning of the substrates of the "hole", defectivity could persist at high rates during the block copolymer assembly process. We explored both thermodynamic aspects (in particular, what type of defective structure might be expected to form based on the patterning of the substrates of the "hole") and kinetic aspects of the assembly process in contact holes. The analysis reveals that tailoring the chemistry of contact hole sidewalls play a dominant role over influencing the likelihood of observing defects after self-assembly. Furthermore, we also find that the most likely transition pathway from a disordered state to an assembled cylinder may contain defects at certain substrate conditions, emphasizing the critical role of designing substrates for avoiding defect formation and subsequent annihilation opposed by large free energy barriers. This work is reproduced from [10]; additionally, portions of the work have been reproduced in the dissertation of co-author Grant Garner [29]. Reproduced figures are noted in the main text here; I place particular emphasis on Figures 2.7-2.9 as my original work of particular novelty.

In Chapter 3, we study the uniquely defective "stitched" morphology formed from lamellae-forming diblock copolymers. When diblock copolymers are self-assembled over some lithographic guiding pattern, small misalignments to the underlying pattern are not uncommon. By contrast, the stitched morphology consists of lamellae completely misaligned to the underlying substrate, and not uniformly aligned throughout the film (see Chapter 3 for a visual representation). We explore both the annihilation and formation of this unique defective morphology. In particular, we emphasize that the annihilation of these misaligned grains is significantly enhanced by contact with aligned lamellae, corroborating experimental observations that large regions of stitched lamellae annihilate primarily from their edges, where

they contact aligned lamellae, and less frequently from their interior. From pseudo-dynamic Monte Carlo simulations where we place upon the system only the assumption that the early dynamics are strongly surface dominated, we find that morphologies strongly resembling the experimentally observed stitched morphology appear naturally. Thus we highlight the importance of surface design in avoiding the appearance of complex defects. This work is reproduced from [9].

In Chapter 4, we explore the unique "bricks-and-mortar" phase. Prior experimental and theoretical work has claimed that a blend of $A-b-(BA')_3$ miktoarm star block copolymers and A homopolymers will, at certain blend fractions and molecular weights, form a phase combining discrete, irregularly shaped and sized, aperiodic A domains in a continuous matrix of B. We utilize three dimensional dynamic simulations to expand upon the understanding of the structure of this phase and is mechanical properties. While we do find a phase closely resembling the bricks-and-mortar phase at conditions matching experiment and theory, we predict the A domains to form a single percolating cluster, which can be disrupted into multiple clusters with the application of shear. However, the phase also displays many of the properties expected of a non-entangled rubber phase, confirming the prominent role molecular bridging between portions of the A domain plays on the mechanical properties. This work serves as a deeper understanding of the morphology of the "bricks-and-mortar" phase while also serving as a platform for future dynamic calculations incorporating the role of glassy A-domains, which our dissipative-particle dynamics simulations do not capture. This work is reproduced from [11] (in preparation).

CHAPTER 2

MECHANISMS OF DIRECTED SELF-ASSEMBLY IN CYLINDRICAL HOLE CONFINEMENTS

2.1 Abstract

The directed self-assembly of block copolymers in cylindrical holes is a promising technology for lithographic patterning, particularly in the context of vertical interconnect accesses. While the hole-shrink process for single cylinders has been extensively explored, the proliferation of morphological defects remains a significant technological barrier. We use a coarse-grained model to explore morphologies that form within cylindrical confinements for combinations of template surface energies. We identify metastable defect morphologies, in addition to the desired cylindrical morphology, in majority-wetting sidewall templates. We use our coarse-grained model and the string method to identify transition pathways between defective morphologies and the cylindrical morphology to elucidate the mechanism of defect annihilation within the confinements; the transition pathway from a disordered state is also identified. This work demonstrates that the minimum free energy path for the formation of a cylinder goes through defective morphologies, and that designing confinements can eliminate these undesirable transition states.

2.2 Introduction

As conventional optical lithographic techniques reach their resolution limit, and with many of the proposed replacements growing in cost, the directed self-assembly (DSA) of block copolymers has attracted considerable industrial interest as a means to achieve cost-efficient, high-resolution patterning at the nanoscale[49, 13, 14, 52, 114, 77]. The DSA process relies on utilizing confinement design and chemically functionalized surfaces, referred to as

graphoepitaxy [113, 111, 112, 110] and chemoepitaxy [121, 122, 55, 106, 73], respectively, in order to coerce a block copolymer morphology into a desired structure. These strategies have proven capable of yielding the assembly of lines[12] and cylinders [94] over large patterned areas [96]. Of particular interest for the fabrication of device-oriented structures is the assembly of cylindrical-phase block copolymers within cylindrical confinements (or "holes"), known as the hole-shrink process [136]. Such a process offers an inexpensive route towards efficient production of vertical interconnect accesses (VIAs) or cut masks [128, 130].

Cylindrical confinements have two unique surfaces: the sidewall of the holes and the circular bottom. The interfacial energy between each surface and each copolymer block needs to be carefully tuned, in concert with the template diameter, to induce the assembly of a desired cylinder. It has been demonstrated that cylinders can successfully form in smaller template diameters if the sidewall preference is for the majority block [129, 34]. However, most theoretical work has focused on cylindrical templates where the sidewall surface is preferentially wet by the minority block of a cylinder-forming block copolymer [47, 46, 59, 135]. Peters et al., using a theoretically informed coarse-grained model, demonstrated that increasing the affinity of the sidewall for the minority block leads to a stabilization of the desired through-film cylinder morphology over other metastable structures[99]. Laachi et al., utilizing a field-theoretic model, have also provided insights into the morphological, kinetic, and thermodynamic differences that exist between non-preferential sidewalls and sidewalls that are preferentially wet by the minority block [57]. These studies collectively support the conclusion that a sidewall that is preferentially wet by the minority block provides a critical boundary condition for obtaining the desired cylindrical morphology. However, given that smaller template diameters have been found to stabilize well ordered cylinders when the sidewall is preferentially wet by the majority block - a reduction from approximately twice the bulk domain spacing to a single bulk domain spacing - additional theoretical study is needed in order to understand assembly under such conditions.

Previous theoretical and simulation studies on such systems has confirmed the stability of a through-film cylinder at templates of approximately one bulk domain spacing in diameter [137, 67, 68, 75], though in general little attention has been paid to optimizing the strength of the sidewall attractiveness for the majority block to produce DSA relevant morphologies. There has also been extensive work on characterizing the phase diagram of block copolymers confined to cylindrical holes with respect to varying strength of sidewall interactions [69], though at template dimensions larger than a single bulk domain spacing.

Recent experimental work by Doise et al. has shown that it is possible to experimentally control the wetting behavior of both the sidewalls and the bottom substrate independently, through random block copolymer brushes [20]. This control has allowed for the modification of the wetting behavior of the sidewalls and bottom of the cylindrical confinements separately; furthermore, the random block copolymer brushes allowed for the surfaces to be preferential for either the majority block or the minority block. Through manipulation of the brush composition, these authors demonstrated the ability to use prepattern holes with smaller and larger critical dimensions (confinements with diameters of approximately one and two times the natural domain spacing, respectively) to drive the assembly of cylindrical morphologies. Doise et al. achieved successful assembly at an open hole rate greater than 95% in some cases (as verified via top down SEM after pattern transfer); this relatively high threshold, however, does not meet the defectivity requirements for industrial applications, prompting further questions about how to optimize a prepattern to reduce or avoid defect formation in contact hole-shrink experiments.

The results reported by Doise et al. were generally in good agreement with predictions by Peters et al. but, at the experimental level, confinement still led in some cases to defective assembly. The work of Peters et al. provided a qualitative understanding of which design rules are necessary for stabilizing a cylindrical morphology, but only considered the final -equilibrium- states reached in a simulation, without addressing how defective states form

and remain stable, or how transitions between defective states occur. Recent work by Li et al., Hur et al. and Laachi et al. has shown that a string method can be used in coarse grained [66, 44] and field theoretic models [57, 58, 46], respectively, to analyze transition pathways in block copolymer systems. These works provided an understanding of transitions between competitive structures in thin films and in cylindrical confinement, but did not address how the formation of competitive, metastable states might interfere with morphology formation. In addition, in the context of exploring the transition between defective states and through film cylinders in contact holes, the work of Laachi et al. only explored a limited number of pre-pattern configurations, and did not consider how optimization of the prepattern might influence defectivity.

Here, we utilize a theoretically informed coarse grained model for block copolymers, which has been shown to be in good agreement with experiment in past work, to explore the emergence of metastable states within cylindrical confinements with a critical dimension of approximately one domain spacing. Subsequently, we use the string method to analyze the transition between competitive states, uncovering the free energy barriers opposing the transition from metastable defects to through-film cylinders. The influence of the strength of the affinity of the sidewall and bottom substrates on these free energy barriers is also considered. Additionally, the transition from a disordered state to a through-film cylinder is investigated at varying template conditions.

We find that in a large sample of simulations repeated at the same set of conditions, different final morphologies appear, including defects and through film cylinders, indicating template conditions which stabilize various morphologies. Transition pathways calculated at prepattern conditions in the vicinity of these regions, where several different morphologies occur, reveal that significant free energy barriers exist that oppose the annihilation of defects, even if the defective states have a significantly higher free energy. The formation of these defects is associated with the fact that they are part of the most probable transition pathway

from a disordered state to a through film cylinder; that is, at certain conditions, a "direct" pathway from order to disorder is less favored than one in which defects occur.

2.3 Results and discussion

The cylindrical confinement for guiding the DSA process utilizes chemoepitaxy and graphoepitaxy to drive the assembly of cylindrical features that span the height of the confinement. The simulations in this work focus on perfectly cylindrical confinements that are filled with poly-styrene-b-(methylmethacrylate), PS-b-PMMA, with a styrene volume fraction of $f_{PMMA} = 0.3$. The match between the simulated polymer and real PS-b-PMMA is provided by confirming that the simulated polymer reproduces the bulk periodicity of PS-b-PMMA; additionally, the chosen χN value is commensurate with PS-b-PMMA. We assume that the surfaces that produce the confinement, the vertical sidewall and the circular bottom, are unique in terms of their affinity for the polymer; thus, the block copolymer that is deposited inside the hole is assumed to have an independent interfacial energy with each surface. The strength of these interfacial energies is governed by the constants Λ_{SW} and Λ_B for the sidewall and bottom surfaces, respectively, and the surfaces interact with the polymer via the potential described below, where z is the distance between a polymer bead and the closest (normal) point on the given surface. A negative value indicates a preference for the minor block, poly-(methyl methacrylate), PMMA, and a positive value indicates a preference for the major block, poly-styrene, PS.

We performed a number of independent Monte Carlo simulations to investigate the impact of the combination of these parameters on a predicted morphology for constant confinement dimensions. A height of 62 nm, $1.67L_0$ and diameter of 43 nm, $1.16L_0$, were chosen in order to be in agreement with the experimental conditions used by Doise et al.[20]. These values were well in the region of the design space that resulted in the desired cylindrical morphology (at least when viewed from a top down perspective, experimentally). Using this

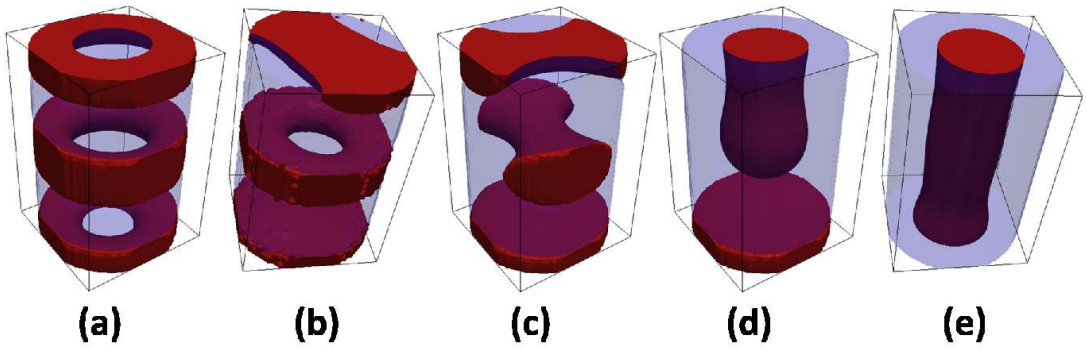

Figure 2.1: A compilation of the well-defined morphologies that were stabilized from independent Monte Carlo simulations of cylinder forming block copolymers. The dark, red phase represents the minority-block rich domain, while the light blue phase is the majority-block rich domain. The morphologies observed were (a) the double donut, 2D, (b) the donut-bar, DB, (c) the double bar, 2B, (d) the disconnected cylinder, DC, and (e) the cylinder. Also reproduced in [29].

Table 2.1: Stable morphologies that exist at intersections in design space

Λ_{SW}	Λ_B	**Stable Morphologies**
0.1	-0.1	2B, 2D
0.1	-0.6	DB, 2B
0.4	-0.2	2B, C, DC
0.3	-0.6	2B, DC
0.6	-0.5	C, DC

geometrical confinement, we set the interfacial energy constants to be $0.0 \leq \Lambda_{SW} \leq 1.0$ and $-1.0 \leq \Lambda_B \leq 0.0$. In this work, the sidewall is assumed to be preferential for PS (or neutral) and the bottom for PMMA (or neutral); again, this is in qualitative agreement with the experimental setup of Doise et al. [20] The simulations were run for 500,000 Monte Carlo sweeps to find the stable morphologies at each interfacial energy combination.

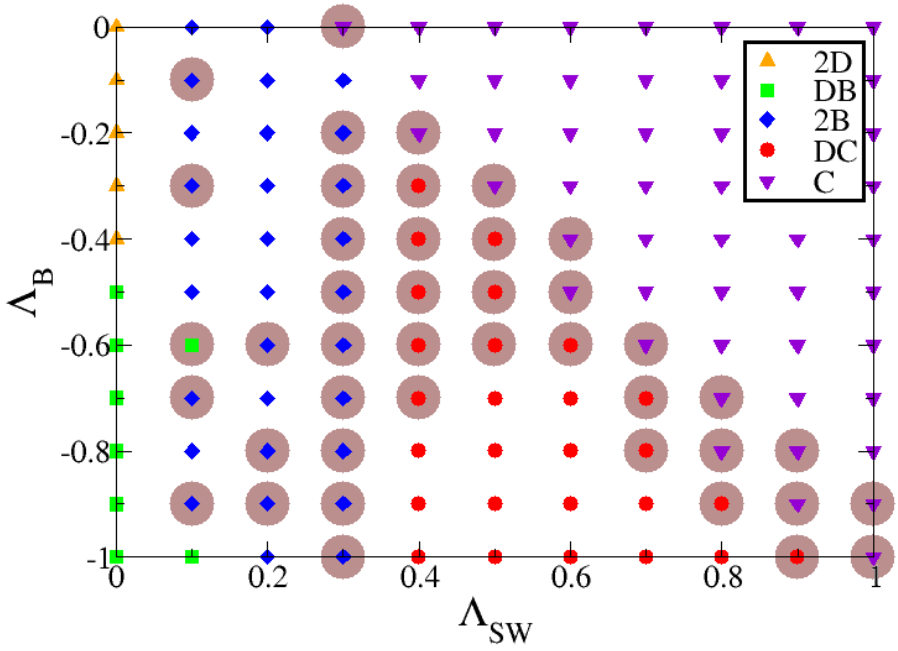

Figure 2.2: A phase diagram that shows which morphologies were most likely to form at a given combination of sidewall preference for the majority block, Λ_{SW}, and bottom preference for the minority block, Λ_B. Each combination of interfacial energies is given a marker that identifies which morphology was observed most often after 10 independent Monte Carlo simulations. The large beige circles denote interfacial energy combinations that resulted in multiple stable morphologies. The absence of a beige circle means that only one type of morphology was stabilized. The morphologies observed can be seen in Figure 2.1, and include the double donut (2D) denoted by orange upward pointing triangles, the donut-bar (DB) denoted by green squares, the double bar (2B) denoted by blue diamonds, the disconnected cylinder (DC) denoted by the red circles, and the cylinder (C) denoted by the violet downward facing triangles. Also reproduced in [29].

The results of these simulations revealed that five unique, well-defined morphologies were stable within this range of parametric combinations. A 3D rendering of those morphologies can be seen in Figure 2.1, which includes the double donut (2D), the donut-bar (DB), the double bar (2B), the disconnected cylinder (DC), and the full cylinder (C). In some confinements, only one of these morphologies was stable across the set of simulations; however, there were many cases where more than one morphology was stable. This implies that either the states have comparable free energies, or that the stabilized morphologies represent kinetically trapped metastable states. Figure 2.2 shows a diagram that illustrates which morphologies were stable at each parametric combination of interfacial energies. The in-

terfacial energy combinations that stabilize multiple morphologies are denoted by the large beige circles surrounding the markers in Figure 2.2 - these combinations are seen at the intersection of the areas of parameter space that stabilize only one structure. The points at these intersections have as potentially stable states the morphologies that are singularly stable in the adjacent areas of design space. Examples of these intersections exist at the combinations of $(\Lambda_{SW}, \Lambda_B)$ listed in Table 2.1. One of the interesting combinations of interfacial energies occurs around the "triple point", where the conditions that stabilize the double bar, the disconnected cylinder, and the cylinder morphologies coincide. At the values of $\Lambda_{SW} = 0.4, \Lambda_B = -0.2$ the Monte Carlo simulations yield formation of all three of the aforementioned morphologies.

At this "triple point", where multiple possible stable states result arise in simulations, we can extract useful thermodynamic and kinetic information about their relative stability using the string method. We chose to analyze the transition pathway between a defective morphology and a cylinder beginning at the "triple point" ($\Lambda_{SW} = 0.4$ and $\Lambda_B = -0.2$), then subsequently in its immediate vicinity in parameter space. This provided the opportunity to analyze the annihilation pathway for two different defects, the double-bar and the disconnected cylinder within a single confinement design.

First, we investigated the transition pathway between the double-bar and cylindrical morphologies using the string method. Figure 2.3 shows the MFEP calculated from the string between a double-bar structure ($\alpha = 0$) and the through-film cylinder ($\alpha = 1$) within a cylindrical confinement with $\Lambda_{SW} = 0.4$ and $\Lambda_B = -0.2$. Two clear transition states can be identified along this pathway. The first transition state is approximately $30 k_B T$ higher in free energy compared to the metastable defect, and it corresponds to the formation of a PMMA bridge linking the upper and middle bars. For this bridge to form, a certain number of PMMA chains must diffuse through a layer of PS, a highly unfavorable and unlikely event - hence, the large barrier. Following the initial bridge formation, however, polymer can diffuse

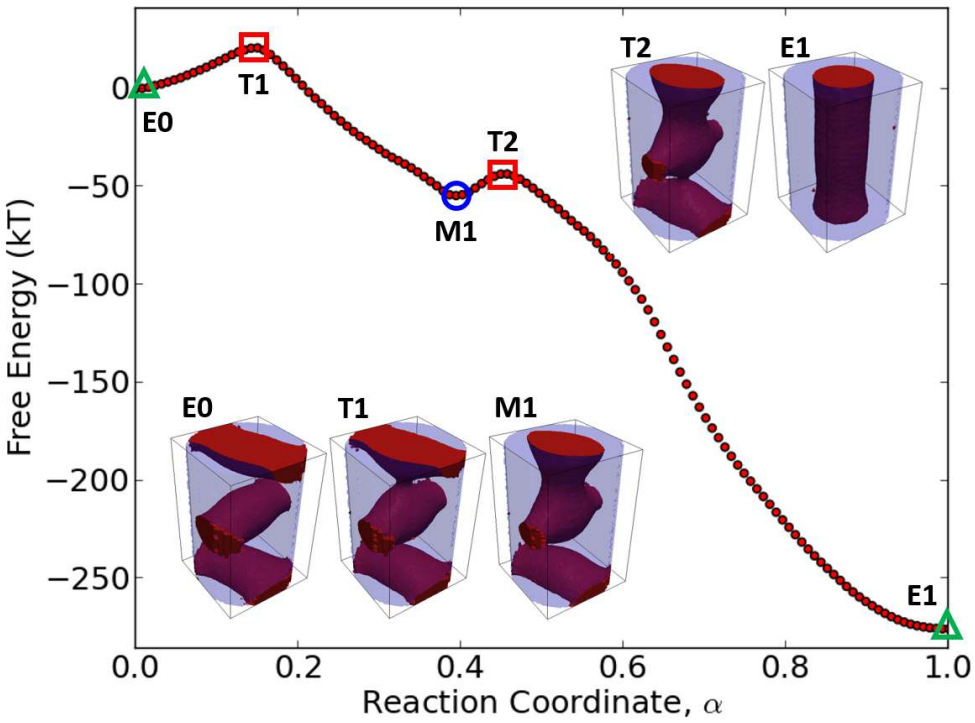

Figure 2.3: The transition pathway along the reaction coordinate α between a double bar morphology and a cylinder with $\Lambda_{SW} = 0.4, \Lambda_B = -0.2$. The green triangles identify the end nodes of the string, the red squares identify the nodes of the string where the transition states occur, and the blue circles identify the location of the metastable states along the pathway. Graphics of the morphologies corresponding to the labeled nodes are included. Also reproduced in [29].

more easily through the bridge, corresponding to the downhill descent in free energy. The second transition state is approximately $15k_BT$ higher in free energy compared to the nearby metastable state, and it corresponds to the formation of a second PMMA bridge between the layer of polymer at the bottom and the growing PMMA structure in the middle. Just as was the case for the first bridge, the diffusion of the first few PMMA chains through the layer of PS is unfavorable, and so the free energy barrier is large. Once that process is initiated, however, there are no more free energy barriers, and polymer simply diffuses through the established bridges to form a well-ordered, complete cylinder. We note the similarity in the connection of these domains to the merging of disconnected lamellae observed in previous studies of defect annihilation [66, 64, 44].

It is of interest to consider why the opposite pathway is not favored - that is, the bottom

bridge forming first, followed by the upper bridge. If the bottom bridge formation occurred first, it is expected that the first free energy barrier would be even higher because, in addition to requiring the same number of chains to diffuse the same distance, PS would be forced (due to the volume-filling nature of the model) to occupy space near the bottom substrate, a situation that is enthalpically unfavorable. This presumably large free energy barrier is circumvented when the system first forms the upper bridge; this also creates a bulge in the PMMA in the center of the system. Thus, when the bottom bridge does form, it need not traverse as great a distance, making up for the enthalpic penalty of forcing PS onto the bottom substrate. While this effect would likely be observed in the opposite pathway as well, it is the avoidance of the first very large barrier that is expected to be most critical.

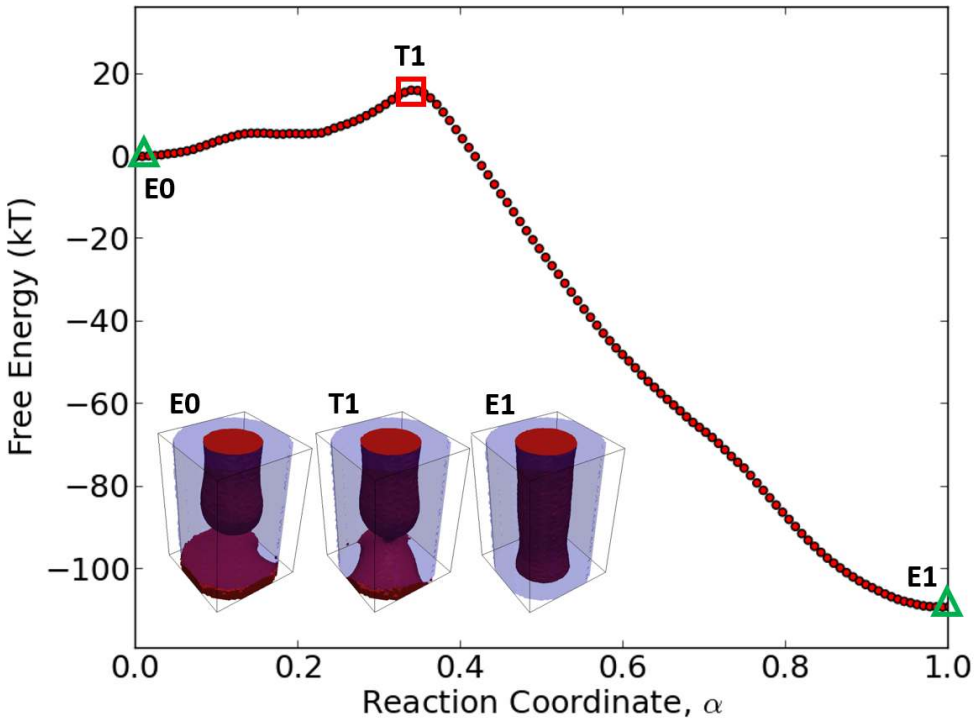

Figure 2.4: The transition pathway along the reaction coordinate α between a disconnected cylinder morphology and a cylinder with $\Lambda_{SW} = 0.4, \Lambda_B = -0.2$. The green triangles identify the end nodes of the string, the red squares identify the nodes of the string where the transition states occur, and the blue circles identify the location of the metastable states along the pathway. Graphics of the morphologies corresponding to the labeled nodes are included. Also reproduced in [29].

Next, we fixed the end states of the string to be the disconnected cylinder and the

complete cylinder morphologies. The calculated MFEP for the annihilation of this defective morphology can be seen in Figure 2.4. The MFEP for annihilation of the disconnected cylinder is similar to the last half of the annihilation of the double-bar, including a transition state that is approximately $20k_BT$ higher than the metastable defect. Likewise, this free energy barrier corresponds to the formation of a PMMA bridge between the bottom layer and the disconnected cylinder, requiring the unfavorable diffusion of PMMA through a PS layer. Indeed, it can be observed in Figure 2.3 that a metastable morphology very much like that corresponding to the disconnected cylinder exists in the middle of the pathway.

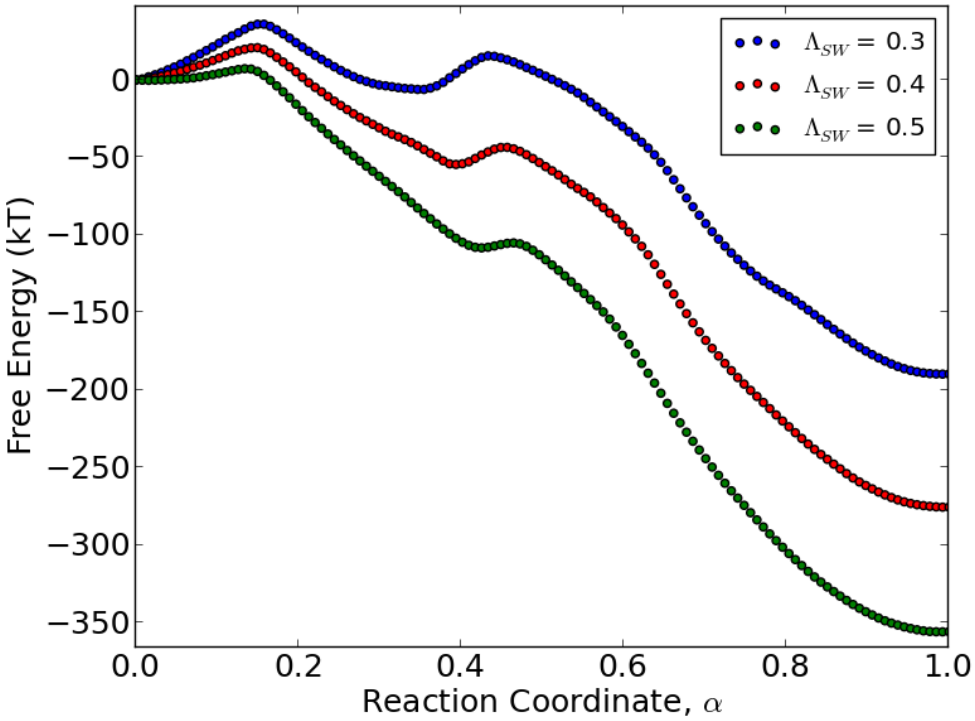

Figure 2.5: Three transition pathway along the reaction coordinate α between a double bar morphology and a cylinder with $\Lambda_B = -0.2$ where the sidewall interfacial energy is varied between $\Lambda_{SW} = \{0.3, 0.4, 0.5\}$. Also reproduced in [29].

It is now clear that these defective morphologies are not competitive at equilibrium, but instead represent long lived kinetically trapped states. Despite the fact that a confinement design can be conceived to thermodynamically favor formation of a complete cylinder, there can simultaneously exist significant barriers that must be overcome if the assembly process

initially leads to an undesirable, meta-stable structure. In an attempt to understand how design parameters affect these barriers, we performed string calculations for several interfacial energy combinations.

Figure 2.5 shows the effect that the sidewall interfacial energy has on the transition barriers by varying the value of $\Lambda_{SW} = \{0.3, 0.4, 0.5\}$ while $\Lambda_B = -0.2$. There is a significant reduction in the free energy barriers associated with both transition states as the sidewall becomes more preferential for the majority block, PS. Meanwhile, the free energy barriers grow much larger if the interaction parameter on the sidewall becomes more weakly preferential for PS.

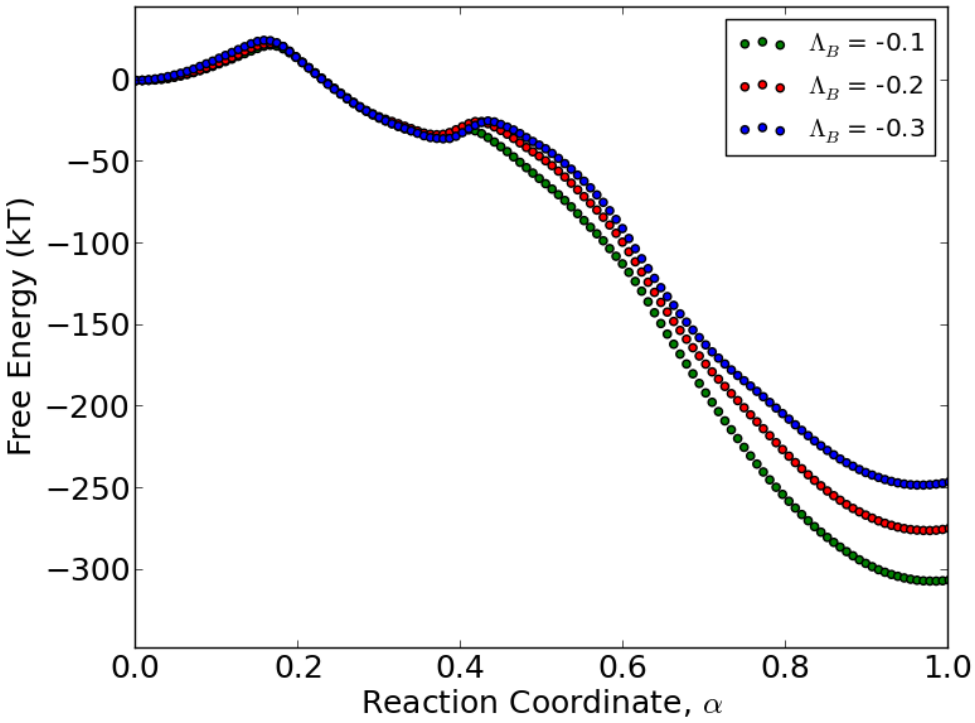

Figure 2.6: Three transition pathway along the reaction coordinate α between a double bar morphology and a cylinder with $\Lambda_{SW} = 0.4$ where the bottom interfacial energy is varied between $\Lambda_B = \{-0.1, -0.2, -0.3\}$. Also reproduced in [29].

Figure 2.6 also shows how the MFEP changes when the interfacial energy corresponding to the interaction between the bottom of the confinement and the polymer changes if we use $\Lambda_B = \{-0.1, -0.2, -0.3\}$ while $\Lambda_{SW} = 0.4$. In contrast to the sidewall interfacial

energy, the bottom of the confinement has only a small effect on the barrier heights of the transition states. The first transition is virtually unaffected, and there is a minor influence on the height of the second free energy barrier. As discussed previously, part of the barrier associated with this latter transition is the forcing of PS to the bottom substrate as PMMA diffuses to the center. If the bottom substrate is less hostile to PS, there is less of a penalty associated with this transition. Furthermore, this observation also explains the reduction in the thermodynamic free energy difference between the two-bar structure and the full cylinder. The volume of PS wetting the bottom surface is greater in the full cylinder morphology than the two-bar morphology; increasing the preference for PMMA of the bottom surface therefore causes a greater perturbation to the free energy of the full cylinder morphology, resulting in the reduction in thermodynamic preference.

The simulation results in Figure 2.5 and Figure 2.6 show that the two unique surfaces comprising the guiding confinement have different effects on the thermodynamics and kinetics of the hole shrink process. These results indicate that it is more important to control the sidewall surface characteristics when trying to minimize the kinetic barriers that exist between defective states such as the two-bar structure and the desired full cylinder morphology. This follows intuition, as the full cylinder morphology needs the majority phase to wet the entirety of the sidewalls of the confinement for the cylinder to exist.

The previous discussion helps us understand why, for a given set of conditions, defective morphologies such as the double-bar or disconnected cylinder structures might persist in a cylindrical confinement; however, it does not completely clarify why such structures may appear in the first place, especially given the thermodynamic free energy difference between the defective structure and the through film cylinder. To address this issue, a series of strings were calculated that connect a disordered state and a through-film cylinder in confinements having varying sidewall energy strengths; the resulting MFEPs are shown in Figures 2.7, 2.8, and 2.9. The disordered states were produced by performing Monte Carlo simulations of a

block copolymer with identical parameters to the polymer used for all other calculations in this work, except with $\chi N = 0.0$. This provided a realistic configuration corresponding to a disordered state, as the MC simulation allowed bond lengths to equilibrate, while the lack of any driving force for segregation between the polymers allowed them to mix freely.

Unsurprisingly, the free energy difference between the disordered state and the through film cylinders is large, on the order of $2000k_BT$, regardless of sidewall wetting behavior (these differences do grow larger as the sidewall preference grows stronger for PS). However, the MFEP for the neutral sidewall ($\Lambda_{SW} = 0.0$), shown in Figure 2.7 has eight distinct transition states, labeled by the red squares along the plotted transition pathway, with barriers on the order of $10k_BT$. Each of these transition states can be linked to a diffusion event that results in a compression of an existing minority-rich domain, as seen in T1, T5, T6, and T8, or the bridging of two nearby minority-rich domains, as seen in T2, T3, T4, and T7. The relative magnitudes of the energy barriers associated with these two types of phenomena show that the diffusion events that bridge two domains require more energy. This can be explained by the increase in interfacial area resulting from the bridging event, and the reduction of interfacial area of a compression event. A larger interfacial area simultaneously increases the entropy and enthalpy of the system, resulting in a considerable activation barrier for the event. These large barriers, along with the fact that a number of the metastable states along this path are lower in free-energy than the desired cylinder structure, provide insights into the difficulty of assembling cylinders within confinements that are not preferentially wet by the majority block.

At a greater sidewall preference for the majority block ($\Lambda_{SW} = 0.3$) the transition states such as the donut morphologies disappear from the MFEP towards a cylinder structure, as shown in Figure 2.8. This increased preference for the majority block also stabilizes the desired morphology relative to the other metastable states, making the cylinder the lowest energy structure along the pathway. However, there still exist multiple barriers - on the

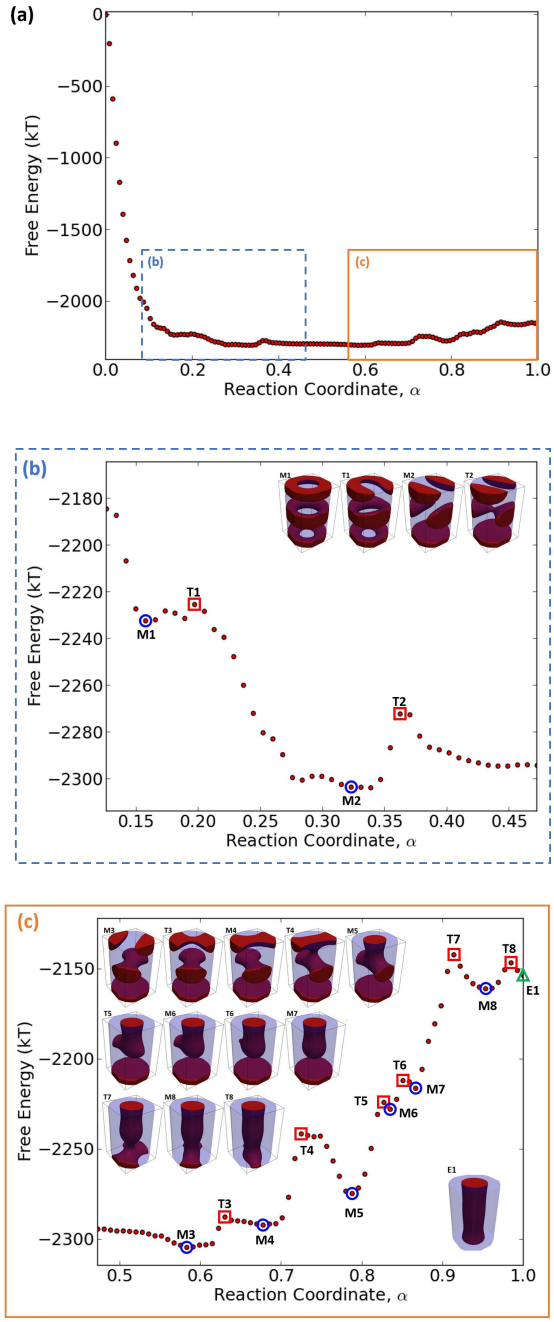

Figure 2.7: The transition pathway along the reaction coordinate α between a disordered block copolymer and a cylinder with $\Lambda_{SW} = 0.0, \Lambda_B = -0.2$. (b) and (c) are zoomed-in segments of the pathway that are included to visualize the features of the calculated minimum free-energy pathway. The green triangle identifies the end node of the string that corresponds to the cylindrical morphology, the red squares identify the nodes of the string where the transition states occur, and the blue circles identify the location of the metastable states along the pathway. Graphics of the morphologies corresponding to the labeled nodes are included.

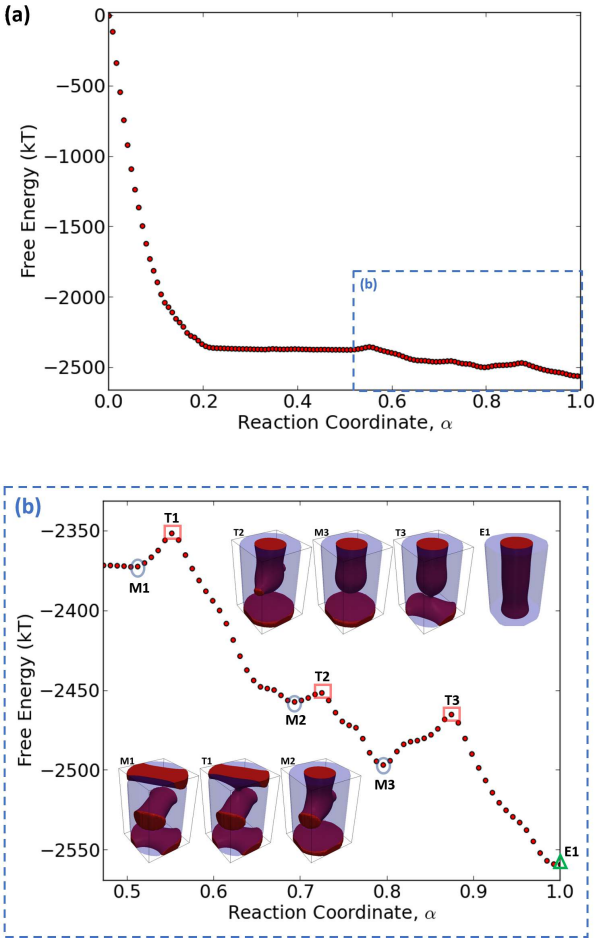

Figure 2.8: The transition pathway along the reaction coordinate α between a disordered block copolymer and a cylinder with $\Lambda_{SW} = 0.3, \Lambda_B = -0.2$. (b) is a zoomed-in segment of the pathway that is included to visualize the features of the calculated minimum free-energy pathway. The green triangle identifies the end node of the string that corresponds to the cylindrical morphology, the red squares identify the nodes of the string where the transition states occur, and the blue circles identify the location of the metastable states along the pathway. Graphics of the morphologies corresponding to the labeled nodes are included.

order of $10k_BT$ - that must be overcome to assemble the cylinder.

These barriers and transition states can be completely eliminated from the transition pathway to a cylinder by further increasing the interfacial energy of the sidewall, as shown in Figure 2.9 where $\Lambda_{SW} = 0.5$. In fact, for this more strongly preferential sidewall, the path from disorder to a cylindrical structure proceeds downhill for the entirety of the formation of a cylinder, with no transition states or metastable states along the way.

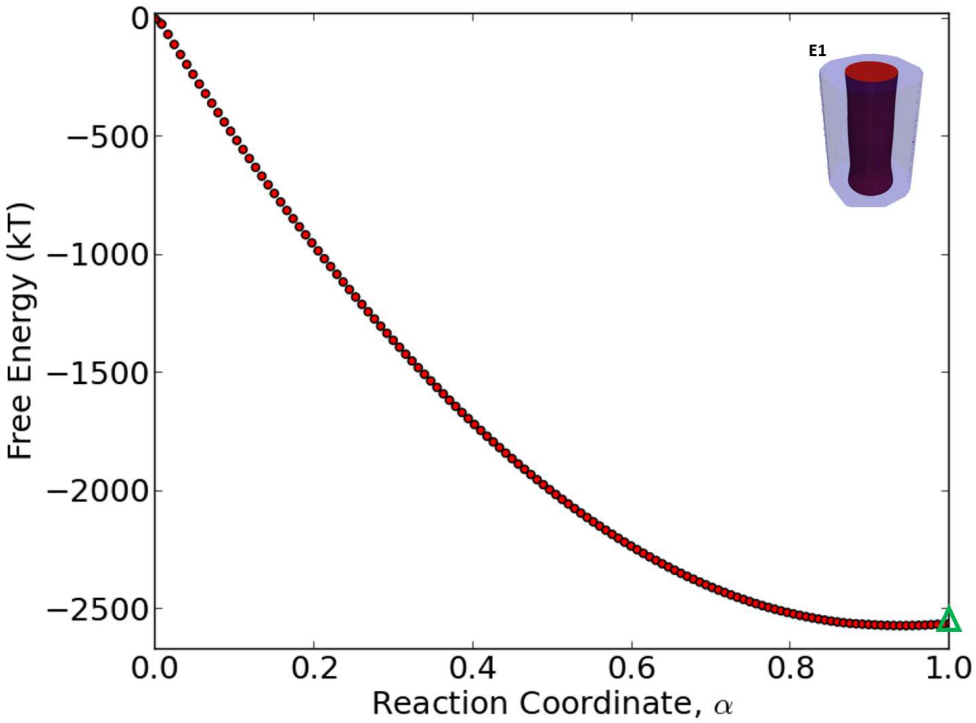

Figure 2.9: The transition pathway along the reaction coordinate α between a disordered block copolymer and a cylinder with $\Lambda_{SW} = 0.5, \Lambda_B = -0.2$. There is no zoomed-in segment of the pathway included as the calculated minimum free-energy pathway is absent of other metastable sates. The green triangle identifies the end node of the string that corresponds to the cylindrical morphology. A graphic of the cylindrical morphology corresponding to the labeled node is included.

This provides evidence that if a sidewall surface can be designed that exhibits a sufficiently strong preference for the majority block, then the MFEP towards the desired cylindrical morphology is void of unwanted meta-stable morphologies. It is likely that continuing to increase the sidewall preference for the majority block will improve dynamics of assembly, as well as the thermodynamics. It is our belief that many pathways, including those that

pass through defects and those which do not, remain competitive regardless of which is most probable. Therefore, continued increase of the sidewall preference for the majority block is likely to give rise to defect-free pathways progressively less probable. Quantifying this effect is a future direction of interest.

Furthermore, we acknowledge that increasing the wetting behavior within a simulation is different than what can be done in experimental systems. While there are kinetic and thermodynamic benefits to using highly preferential sidewalls for the majority block, there is no guarantee that an experimental confinement can be designed to be selective enough to realize the elimination of metastable states along the most probable path for cylinder formation. Lastly, we acknowledge that experimental assembly may not begin entirely from disorder; assembly may already have begun at an earlier stage of an experimental assembly process.

2.4 Conclusions

The systematic study of the single-hole shrink process where the sidewalls are wet by the majority block of a cylinder forming block copolymer have allowed for the identification of the metastable states that may arise depending on confinement design. Subsequent application of the string method has enable a detailed analysis of the transition pathways between defective states and the desirable through-film cylindrical morphology; specifically, the study of a single design chemistry where three different morphologies were stabilized in independent Monte Carlo simulations: a double-bar, a disconnected cylinder, and a complete cylinder. The complete cylinder was identified to be the morphology with the lowest free-energy of the three; however, the transition pathway between the desired morphology and the defects was found to exhibit significant energetic barriers of approximately $30k_BT$. This finding provides insights into the challenges associated with reaching industrial defect standards, as the diffusion events necessary to transition from a defect to a cylinder are unlikely to

occur if the system ends up in a defective state. Altering the sidewall chemistry has been shown to have a much more significant impact on these pathways than the chemistry of the bottom surface. To complete the understanding of defectivity, we demonstrated a method to identify the most likely transition pathway for forming a cylinder from a disordered melt. In confinements with low preference for the majority block, the minimum free-energy path for forming a cylinder goes through numerous metastable states separated by large barriers. We demonstrated that this MFEP is fundamentally changed in confinements with preferential sidewalls. As the sidewall becomes more preferential for the majority block, the number of metastable states that exist in the pathway is reduced until, for a sufficiently strong preference, the MFEP proceeds downhill, going straight to the desired cylindrical morphology. We note that the string method used to find this pathway is only able to identify a single, most probable transition path, and does not speak to the relative probability of proceeding down this path. However, the demonstrated ability to fundamentally change the most probable path using confinement design is promising, as it implies that if the sidewalls of these confinements can be created to be highly preferential for the majority block, the resulting hole-shrink process will be better suited to meet industrial defect standards.

2.5 Methods

The simulation results presented in this work are based on the standard theoretically informed coarse-grained model[83, 27, 19], which represents n block copolymer Gaussian chains discretized into N beads connected by harmonic springs in a fixed volume V at a fixed temperature T. This model has previously been shown to be in quantitative with experimental results [17, 18]. In this model, the energy associated with the polymer bonds is expressed as

$$\frac{H_b[\{\mathbf{r}_i(s)\}]}{k_B T} = \frac{3}{2b^2} \sum_{i=1}^{n} \sum_{s=1}^{N-1} [\mathbf{r}_i(s+1) - \mathbf{r}_i(s)]^2 \tag{2.1}$$

where the s^{th} bead on the i^{th} chain has position $\mathbf{r}_i(s)$. R_e is the end-to-end distance of the polymer chains; typically, a unit system is adopted for the simulations where the end-to-end distance is unity. Additionally, k_B is the Boltzmann constant. The energy associated with non-bonded interactions is given as

$$\frac{H_{nb}[\phi_A, \phi_B]}{k_B T} = \frac{\sqrt{\overline{N}}}{R_e^3} \int_V d\mathbf{r}[\chi_{AB} N \phi_A \phi_B + \frac{\kappa N}{2}(1 - \phi_A - \phi_B)^2] \tag{2.2}$$

where $\sqrt{\overline{N}} = \frac{\rho_0 R_e^3}{N}$, the interdigitation number, is an estimate of the number of chains a given chains interacts with (ρ_0 is the average bulk number density of beads). The parameter χN is the Flory-Huggins parameter governing the incompatibility of the two blocks, and κ^{-1} is proportional to the melt compressibility. Each term $\phi(r)$ is a function of the local density of each type of bead; these densities are calculated by a particle-to-mesh (PM_0) scheme, where the underlying grid is comprised of cubic cells with side length ΔL.

The cylindrical confinement is imposed by hard walls; the sidewall and bottom substrate interact with the polymer according to

$$\frac{H_S}{k_B T} = \sum_{i=1}^{nN} f_s(x, y, K) \frac{\Lambda^K}{N d_s} \exp(\frac{-z^2}{2 d_s^2}) \tag{2.3}$$

where K is the type of monomer bead; the term $f_s(x, y, K)$ adopts a value of either -1 or 1, depending on the value of K and the position of the bead. Λ^K defines the strength of interaction between the surface and the bead; when a bead of type A is in a position preferable to type B, the overall energy contribution should be positive, and $\Lambda^A = -\Lambda^B$. Lastly, z is the distance to the surface, and d_s is the decay length of the potential. Both the sidewall and the bottom surface contribute a term of this form. The model is implemented in the context of a Monte Carlo simulation. Configurations are sampled according to the Metropolis criterion, where the probability of accepting a trial configuration is given by

$p_{acc} = \exp(-\Delta H/(k_B T))$. Trial configurations are proposed using two different Monte Carlo moves; single bead displacement and chain reptation.

To find the minimum free energy pathways between two states of interest, we make use of the string method as described by Maragliano et al. [22, 24, 23, 131, 78, 79, 85, 15, 127, 90, 66] A string of points is constructed to connect two end states; each point along the string, or image, represents a unique morphology. The string is mathematically described as $\mathbf{m}(\alpha)$ where α is the reaction coordinate ($0 \leq \alpha \leq 1$). The images are vectors, each component m_i of which is a function of an order parameter constructed from the local densities on a grid. At each point r_i in the grid, $m_i = \frac{\phi_A(r_i) - \phi_B(r_i)}{\phi_A(r_i) + \phi_B(r_i)}$. This quantity represents the normalized density differences between beads of type A and B in a volume ΔL^3 around each point r_i in a grid that spans the entire simulation box.

The condition for the string to be the MFEP is that the perpendicular component of the gradient of the mean force along the string must be zero everywhere. The potential of mean force on the string, defined at each image, is given by

$$F(\mathbf{m}) = -k_B T \ln \int d\{\mathbf{r}^{nN}\} \exp(-\frac{H}{k_B T}) \delta[\mathbf{m} - \hat{\mathbf{m}}]. \tag{2.4}$$

In this equation, $\hat{\mathbf{m}}$ indicates the order parameter vector constructed from the particle coordinates $\{\mathbf{r}^{nN}\}$. The MFEP satisfies $\nabla_\perp F(\mathbf{m}) = 0$, which means that the variation perpendicular to the path is zero everywhere along the path. The mean force is numerically calculated via umbrella sampling with a harmonic restraint; the total Hamiltonian has the additional term

$$\frac{H_c}{k_B T} = \frac{\lambda}{2} \int_V d\mathbf{r} [\mathbf{m} - \hat{\mathbf{m}}]^2 \tag{2.5}$$

where λ is a spring constant that controls the strength of the restraining potential. In the limit of an infinitely large spring constant, the free energy of the restrained system converges to the free-energy functional $F(\mathbf{m})$. Using a spatial grid to evaluate the integral

in the umbrella potential, the differential of free energy with respect to $\mathbf{m}$ goes to $\frac{\delta F}{\delta \mathbf{m}} = \lambda \Delta L^3 k_B T[\mathbf{m} - \langle \hat{\mathbf{m}} \rangle_c]$, where $\langle \hat{\mathbf{m}} \rangle$ is averaged over many MC steps. Therefore, the string is updated every iteration according to $\mathbf{m}_{k+1} = \mathbf{m}_k - \tau \lambda \Delta L^3 [\mathbf{m}_k - \langle \hat{\mathbf{m}} \rangle_c]$, where τ is a time constant controlling the frequency at which the string is updated. As described in Maragliano et al., the images are redistributed after every iteration to keep them from falling into the minima of the free energy landscape [78].

In our work the string is discretized into 128 nodes, each of which is an independent MC simulation used to estimate the mean force along the string. Note that preliminary calculations showed that 64 images are insufficient, and more than 128 images do not change the final pathway appreciably. The free energy along the string can be determined from the free energy estimation method outlined in Maragliano et al. [78] The strings were initialized as linear interpolations in collective variable space between a defective morphology (or a disordered melt), $\alpha = 0$, and a perfect, through-film cylinder, $\alpha = 1$. These states were chosen from independent MC simulations. When calculating pathways between defects and ordered cylinders, the ends of the string are free to move, ensuring the ends represent local minima. When calculating pathways between disorder and ordered cylinders, the first string node is fixed, while the others move in accordance with the string method (in anticipation that the disordered state will not represent a local free energy minimum, but instead an unstable state).

CHAPTER 3

FORMATION, STABILITY, AND ANNIHILATION OF THE STITCHED MORPHOLOGY IN BLOCK COPOLYMER THIN FILMS

3.1 Abstract

The directed self-assembly of block copolymer thin films offers promise for next generation lithography, providing access to small feature dimensions for electronic devices. Defective assembly, wherein the block copolymer does not assemble in alignment with an underlying template, is a well known and enduring problem facing this technology. Resolving this challenge requires detailed understanding of the kinetics of defective assembly as well as the three-dimensional structure of defects. Recent experiments in this direction have revealed the existence of a unique "stitched" morphology and have examined the kinetics of its assembly and annihilation. However, a computational perspective has not yet been provided. In this work we analyze the formation of the stitched morphology from a disordered state, provide understanding as to its genesis and stability, and explore its annihilation into aligned lamellae. We find that the topography of the guiding template in conjunction with the thickness of the film provide stability to this unique morphology. Furthermore, we find that the stitched morphology's annihilation is significantly enhanced by the presence of nearby aligned lamellae, consistent with experiments. Lastly, we demonstrate that the stitched morphology is predicted to form from unbiased simulations, lending validity to experimental observations of this peculiar morphology.

3.2 Introduction

Block copolymers consist of two or more chemically distinct polymer blocks joined to one another by covalent bonds. A melt of block copolymers is driven to phase separate by unfavorable enthalpic interactions between the different blocks, but is unable to macrophase separate because of the ensuing entropic penalties associated with stretching the block copolymer chains. Consequently, block copolymers microphase separate into a rich variety of ordered nanostructured phases [60, 25]. The scale of the resulting microdomains (on the order of 10 nm) has led to their consideration as an approach to templating lithographic patterns for electronic device fabrication [95, 123, 16, 54, 50, 6, 51].

The production of such devices demands control over the long-range orientational order of the nanostructures, achieved through *directed* self-assembly (DSA) of the block copolymers. In DSA, the block copolymer melt is assembled atop a lithographically defined template which may exhibit chemical preference for one of the blocks (chemoepitaxy [55, 121, 122, 106, 73, 72]), a topographic contrast with the background substrate (graphoepitaxy [113, 111, 112, 110, 124]), or both. The lithographic template may exhibit a lower resolution than the desired final pattern; in this case, the block copolymer material serves to interpolate between the template features, resulting in a process of "pattern multiplication" or "density multiplication", and achieving the target resolution [14, 71].

In this context, any feature of the self-assembled nanostructure that is not "guided" by the underlying lithographic template is deemed a defect. A significant challenge facing DSA is the extremely low defect density ($0.01/\text{cm}^2$) that must be attained for industrial device fabrication. Previous theoretical and simulation studies of defects in DSA indicate they represent kinetically trapped metastable structures [93, 66, 44, 65, 64, 63, 45]. Consequently, insight into the kinetics of the formation and annihilation of defects in DSA is critical to reducing defect density in block copolymer thin films. Recent reports have provided a deeper understanding of the kinetics of DSA through high-speed atomic force microscopy (AFM)

measurements, to visualize the pattern evolution in real time[103] and using TEM (transmission electron microscope) tomography to visualize the three-dimensional structures that form during DSA[104].

These studies have revealed that a unique defective morphology emerges when a block copolymer melt is assembled over a common type of lithographic template combining chemo- and grapho-epitaxy, and when the block copolymer thin film is coated to certain thicknesses, roughly corresponding to 1.25 to 1.5 L_0 (where L_0 is the bulk lamellar periodicity of the block copolymer). This morphology, termed the "stitched" morphology, is defective and does not occur in bulk assembly of block copolymers, yet is also metastable and appears to be an integral part of the pathway of evolution towards aligned lamellae. This complex morphology has not been investigated computationally before.

Here, we utilize a theoretically informed coarse-grained model for block copolymers to probe the nature of the stitched morphology. We compare the free energies of a variety of structures under different constraints (including the film thickness, the template topography, and the chemical guiding stripes), finding that the template topography alone helps stabilize orthogonal and "sandwich" type morphology, while the introduction of chemical guiding stripes dominate these interactions and stabilize aligned lamellae at equilibrium, suggesting the appearance of the stitch morphology is a fundamentally kinetic phenomenon. Further, we use the string method to reveal the kinetic pathways of assembly under the aforementioned constraints, seeking to understand the annihilation of the stitched morphology into aligned lamellae. We find that the stitched morphology may annihilate into lamellae directly, but that free energy barriers to annihilation are reduced when the system is in contact with already formed lamellae, consistent with the experimental results of Raybin et. al[103]. Lastly, we perform unbiased Monte Carlo simulations - making only the assumption that the early dynamics are surface driven - and find that a morphology greatly resembling the stitched morphology emerges, helping validate experimental observations of this unique state.

Overall, we conclude that the influence of the guiding template in the earliest stages of assembly not only guides the overall assembly to aligned lamellae, but can produce such metastable states as the stitched morphology, and suggest that more complex template design may achieve the desired goal of aligned phases while avoiding spurious defects.

3.3 Results and discussion

We begin with a brief summary of experimental observations relevant to the stitched morphology from the recent literature[103, 104]. The stitched morphology is observed for a lamellae-forming polystyrene-*block*-poly(methyl methacrylate) (PS-*b*-PMMA) block copolymer melt (L_0 = 28 nm) when assembled over a lithographic template at small thicknesses. The chemical pattern consists of cross-linked polystyrene guiding stripes that also exhibit a slight topographic contrast with the substrate; the contrast can be varied, and the stitched morphology was first observed for a guiding stripe height of 0.14 L_0. Subsequent processing causes these guiding stripes to retain sidewalls that become oxidized. The background region consists of a random PS-PMMA brush. Consequently, the template is three-toned - the tops of the guiding stripes are PS-preferential, while the sidewalls of the guiding stripes as well as the background region are PMMA-preferential; the sidewalls are more strongly preferential to PMMA than the background is. The fine details of the patterns have been characterized in recent X-ray measurements [53]. The pattern is designed for 3X density multiplication - there is a stripe present on the substrate every $3L_0$, with the block copolymer expected to interpolate the intermediate lamellae. When the block copolymer is coated at a thickness of 1.25 L_0, the stitched morphology is observed. In Ren et. al, various aspects of the film thickness and template topography were varied, exploring the impact of these parameters on the stitched morphology stability; in this work, we focus on the condition where the geometry of the template and film are fixed, to better understand the fundamental origins of the stitched morphology.

The expected, ideal morphology would consist of alternating PS-PMMA lamellae aligned perfectly to the guiding stripes. The stitched morphology, which is observed over large portions of the thermally annealed samples after a few minutes of annealing, is instead composed of a region of lamellae oriented orthogonally to the guiding stripes, laying atop those guiding stripes, and a region of lamellae oriented parallel to the substrate in a "sandwich" structure, laying atop the background region. Interestingly, it is observed that PS wets the nominally PMMA-wetting substrate over the background region. The boundary of these two regions resembles a Scherk's first surface[104], which has been observed at lamellar grain boundaries in the past [31, 74]. We include STEM images representing the stitched morphology in Figure 3.1.

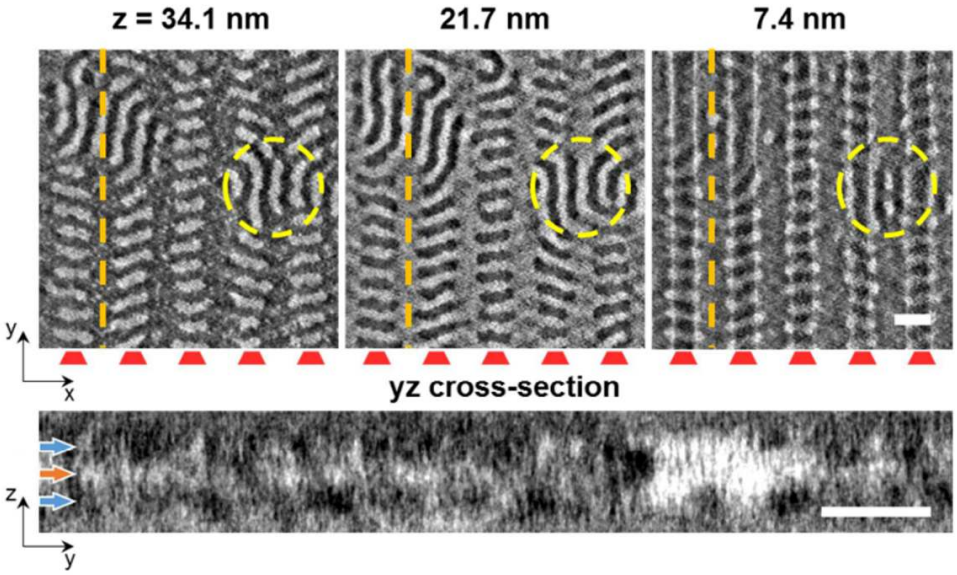

Figure 3.1: STEM tomography of the 3D structure formed after 3 minutes of annealing at 190 °C. PS domains appear dark, while PMMA domains appear light. Three cross sections taken at different film heights are represented. The location of guiding stripes is indicates with red trapezoids. The propagation of the stitched grains over the guiding stripes can be seen clearly. A cross section taken over the background region (indicated by the orange dashed lines) shows the PS-PMMA-PS parallel lamellae formed over the background, with the small inset arrows pointing out the different domains. The yellow dashed circle indicates a region of oriented lamellae already formed. The scale bar in both images represents 50 nm. Reprinted (adapted) with permission from Ren et al.[104]. Copyright 2018 American Chemical Society.

In this work we study the behavior of a coarse-grained polymer melt, with model parame-

ters (specifically, L_0 and χN) chosen to match PS-b-PMMA, assembled under the constraints as described above; see below for further detail. The guiding stripes are parameterized such that the three-toned nature of the experimental template is captured, with the top surface weakly PS-preferential, the substrate weakly PMMA-preferential, and the sidewall strongly PMMA-preferential, following experimental descriptions[104]. Representations of the lamellae and stitched morphologies as density fields (using the order parameter Φ; see below) are shown in Figure 3.2.

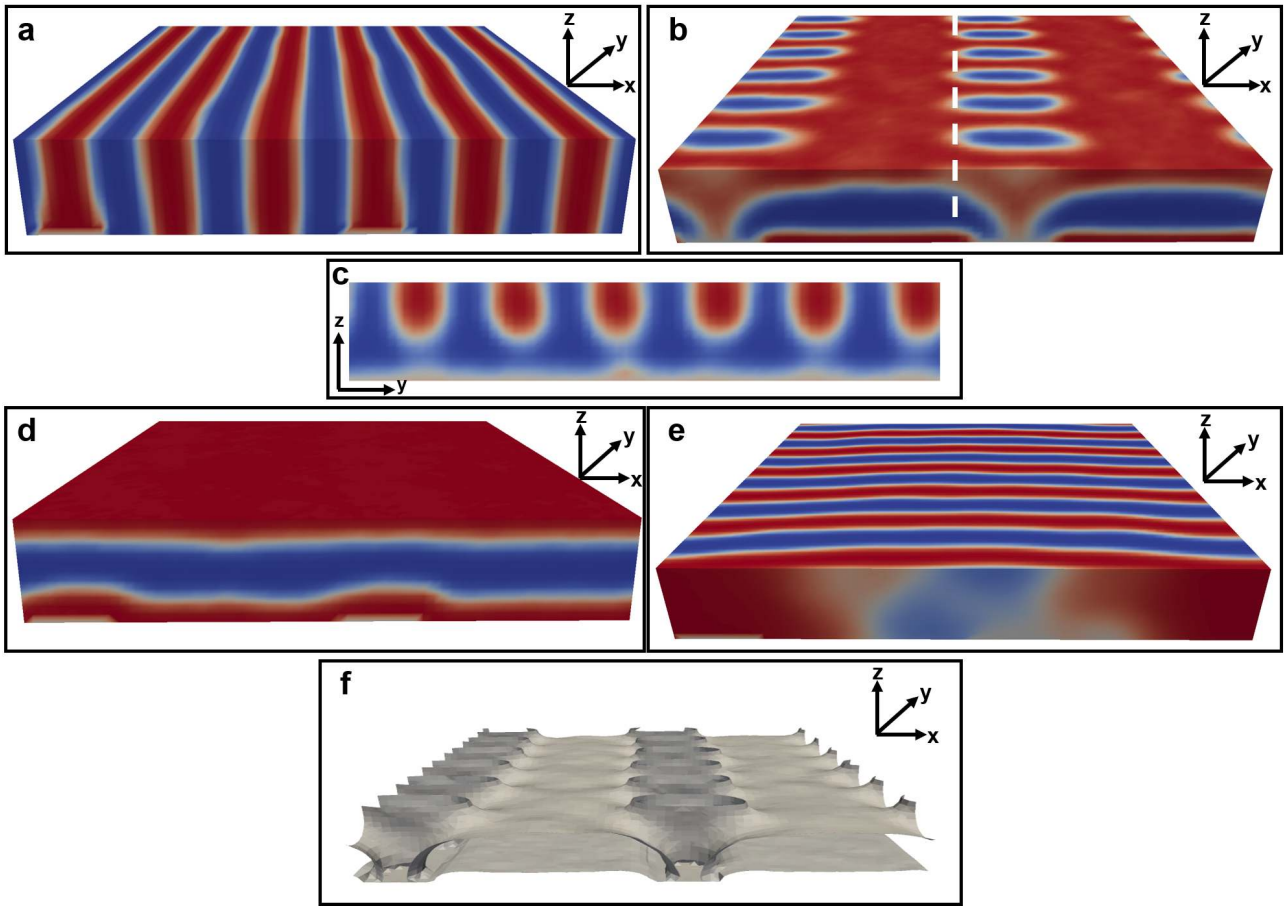

Figure 3.2: Density field visualizations of the key morphologies of relevance - in **a** the lamellar morphology is represented, and in **b** the stitched morphology is represented, from a view looking down the y-axis from a slight angle, so that the top of the film can also be observed. From the same angle, a full film of parallel lamellae is represented in **d** and a full film of lamellae oriented orthogonally to the guiding stripe is represented in **e**. In **c** the interface between the lamellae oriented orthogonally to the guiding stripe and the lamellae oriented parallel to the substrate is shown, with the x-axis coming out of the plane of the image (the white dashed line in **b** corresponds to this slice). This interface resembles Scherk's first surface. In **f**, the internal AB interface of the stitched morphology is presented. In all images, red domains are PS and blue domains are PMMA, and interfaces are colored gray. In **a** and **b** the elevated guiding stripe is weakly visible as a region where the order parameter Φ is zero (and therefore colored gray), visible under the first and fourth PS lamella (from the left) in **a** and under the domains oriented orthogonally to the guiding stripe in **b**; the guiding stripes are visible at the same corresponding locations in **d** and **e**.

As has been noted, the stitched morphology is only observed under confinement and under the influence of a 3X density multiplication guiding pattern. The specific nature of how each of these factors contributes to stabilizing the stitched morphology has not yet been made clear. We consider first the relative free energy of different morphologies in systems which possess different aspects of the experimental confinement. To do so, we use the string

Structure 1	Structure 2	Constraints	$\Delta F/k_BT$ (per chain)
Parallel	"Aligned"	Confined, no topography, nonpreferential substrate	-0.14 ± 0.016
Orthogonal	Aligned	Confined, with topography, nonpreferential substrate	0.021 ± 0.017
Parallel	Aligned	Confined, with topography, nonpreferential substrate	-0.023 ± 0.018
Stitched	Aligned	Confined, with topography, lamellae-guiding substrate	-0.18 ± 0.012
Stitched	Parallel	Confined, with topography, lamellae-guiding substrate	-0.094 ± 0.049
Stitched	Orthogonal	Confined, with topography, lamellae-guiding substrate	-0.14 ± 0.0059

Table 3.1: The free energy differences, $\Delta F = F_2 - F_1$, between states under particular geometric and chemical constraints. ΔF is reported as the averaged value across a number of iterations of the string method, with the error reported as one standard deviation from the mean. Note that in the system without topography there is slightly more available volume, and so free energies are reported per chain in the simulation box.

method only to find the free energy difference between states, not yet being concerned with pathways between metastable morphologies. Using the string method in this way (as opposed to conventional thermodynamic integration[88, 18, 92]) yields a thermodynamically reversible path along with one can obtain free-energy differences.

In addition to the system analogous to the experimental case described above, we consider a system which has a flat, non-preferential substrate, confined to a specific thickness, as well as a system which has the topography of the guiding stripes but no chemical preference at the substrate. In the system with a flat substrate we compare a parallel lamellae structure, with three lamellae layers stacked parallel to the substrate. Since there is no chemical preference at any substrate, it is immaterial which block wets the bottom surface. We also consider lamellae oriented as if they were aligned to the guiding stripes, though the stripes are not actually present. Since the substrate is flat and non-preferential, this structure is invariant to any rotation of the lamellar orientation about the z-axis. The structures used are identical to those in Figure 3.2, with the exception that there are no guiding stripes, and therefore the bottom substrate is flat and homogeneous. In Table 3.1, we show the free energy difference; the "aligned" lamellae are lower in free energy than the parallel structure, consistent with theoretical predictions[81, 102, 30].

Next we consider a system that is confined to the experimental thickness and has the guiding stripes, but in which the guiding stripes have no preference for either block. In this case, the only additional interaction comes from the excluded volume of the stripes. We com-

pare the parallel lamellae to the aligned lamellae, as well as to lamellae oriented orthogonally to the guiding stripes. Theoretical results suggest that orthogonally oriented lamellae ought to be lower in free energy, as polymer chains must stretch to align to the topographically contrasted guiding stripes[101]. Indeed, we find that the orthogonally oriented morphology is lower in free energy than the aligned morphology. Interestingly, free energy difference between the "sandwich" morphology and the aligned lamellae has been reduced by an order of magnitude; within error, the two states are approximately equal in free energy. The free energies are all somewhat close, suggesting that, experimentally, a film assembled under such conditions could be expected to, at least transiently, feature all three morphologies to some degree in a mixed morphology.

Next, we consider directly the free energy of the stitched morphology compared to aligned lamellae. It is clear from Table 3.1 that, despite the mitigating influence of the confinement and the template topography, the lamellae-guiding substrate interactions make the aligned lamellae morphology preferred over the stitched morphology at equilibrium. We also directly compare the stitched morphology to a sample of fully orthogonal lamellae and a sample of fully parallel lamellae; the stitch is higher in free energy than both of theses, suggesting it is a purely metastable state. The free energy difference in Table 3.1 comes from a converged string method calculation; the full minimum free energy pathway (MFEP) resulting from this calculation is presented in Figure 3.3. Taken together, these calculations suggest that in general the guiding substrate introduces a fairly strong preference for producing morphologies aligned to the template. Later, we will turn toward dynamically observing the formation of ordered phases under the expected real conditions of assembly to understand how, therefore, a stitched morphology may form.

From the MFEP between a stitched morphology and aligned lamellae, we seek an understanding of the kinetic pathway leading to the annihilation of the stitched morphology into aligned lamellae; however, from observation of the in-situ AFM data in Raybin et. al [103],

we note that one generally observes stitched grains annihilating in contact with already aligned lamellae. Setting aside for the moment the question of how stitched and aligned grains might come to coexist during the assembly process, we focus on understanding the difference between annihilation of stitched grains in contact with and not in contact with aligned lamellae. We therefore compute the MFEP starting from a box which contains half a stitched morphology and half an aligned lamellae morphology; this starting morphology is represented in Figure 3.5, which shows all the key morphologies along the MFEP for the half-stitched to fully aligned annihilation.

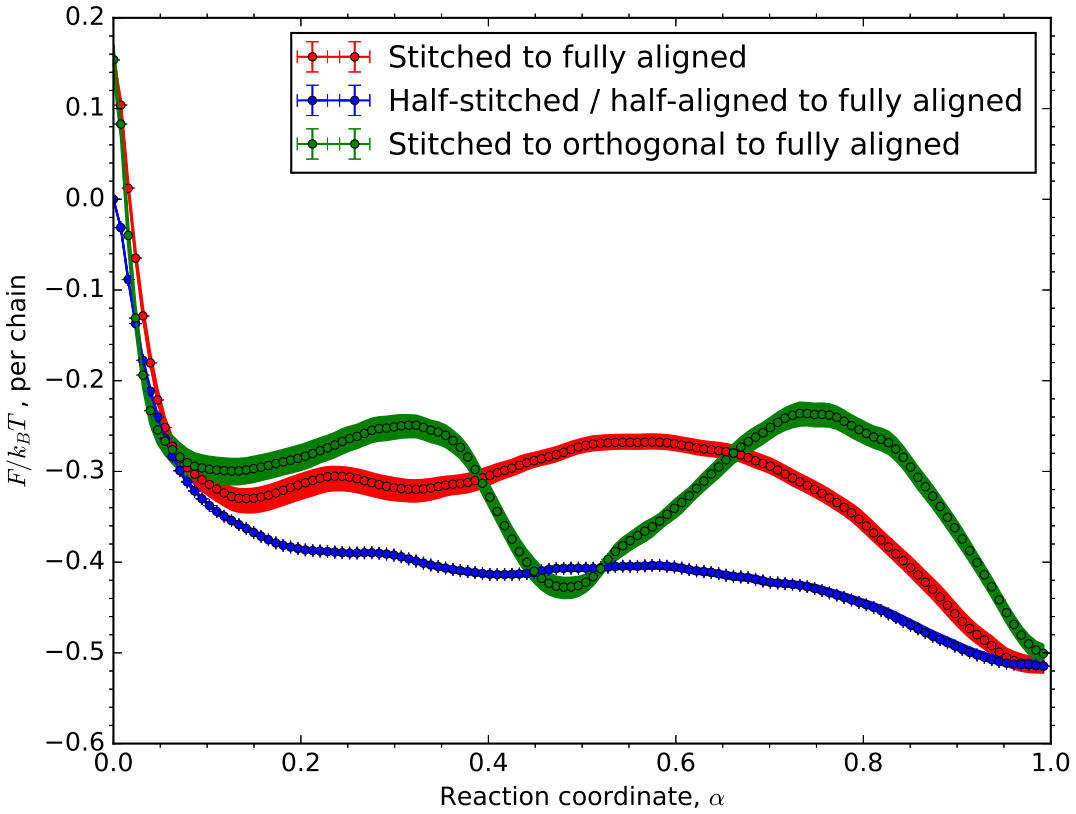

Figure 3.3: The minimum free energy pathways from the fully stitched to the fully aligned lamellae morphology (red), from the half-stitched / half-lamellae morphology (blue), and from the fully stitched to the fully aligned lamellae morphology with an intermediate state at $\alpha = 0.5$ of the orthogonally aligned lamellae (green). The value F at each value of α sampled from several iterations of the string method after convergence is averaged; the shaded region represents the region in which the strings included in the averaging lie.

First, we note that in both cases, the provided initial morphology is not strictly speaking the metastable stitched morphology, and the provided state at $\alpha = 0$ relaxes into the appropriately metastable morphology by $\alpha \approx 0.14$ for the stitched to fully aligned pathway (the stitched morphology in Figure 3.2 corresponds to $\alpha = 0$; the morphology at $\alpha = 0.14$ undergoes some minor rearrangements); for the half-stitched to fully aligned pathway, as discussed below, the provided half-stitch does not have an exactly metastable analog. It is important to emphasize that the large free energy declines in the early stages of the pathway are not considered a physical part of the true pathway, but are an artifact of our choice to not allow the first image of the string to move – as described below, this improves the accuracy of the calculation without changing the physical pathway after this initial rearrangement. From this point forward, however, the MFEP represents the (most likely) pathway that each metastable morphology takes toward annihilation.

The fully stitched morphology begins annihilating by first displacing PMMA directly in contact with the guiding stripe, leading to the stripe being fully wet by PS. Despite the presence of the preferential guiding stripe, the growth of PS bridges between the orthogonal lamellae over the stripe is associated with a free energy barrier of $0.024 \pm 0.0082\ k_BT$ per chain; the top of this barrier occurs at $\alpha \approx 0.24$. The system reaches a local free energy minimum at $\alpha \approx 0.34$, associated with the upward propagation of the layer of PS wetting the guiding stripe. By this point, one can also observe a degree of "buckling" in the middle PMMA layer of the parallel lamellae over the background region. The buckling becomes more pronounced until the PMMA layer breaks through to the top of the film in several places, associated with the second, larger free energy barrier of $0.049 \pm 0.011 k_BT$ per chain; the top of this barrier occurs at $\alpha \approx 0.56$. After a sufficient amount of PMMA has broken through to the surface of the film, it becomes possible for those layers to begin merging with one another, while at the same time the orthogonal PMMA domains over the guiding stripe begin to divide and merge with buckling domains of PMMA nearby. After the transition

state at $\alpha \approx 0.56$, there are no (significant) free energy barriers or local free energy minima; representative snapshots of the system at $\alpha \approx 0.64, 0.72$, and 0.79 are provided. Finally, at $\alpha = 1$, through-film aligned lamellae are formed. The events are depicted in Figure 3.4. The animations are presented from the full-film view, looking down the y-axis at a slight angle, as well as a view over a guiding stripe and from a slice over the middle of a background region, looking down the x-axis.

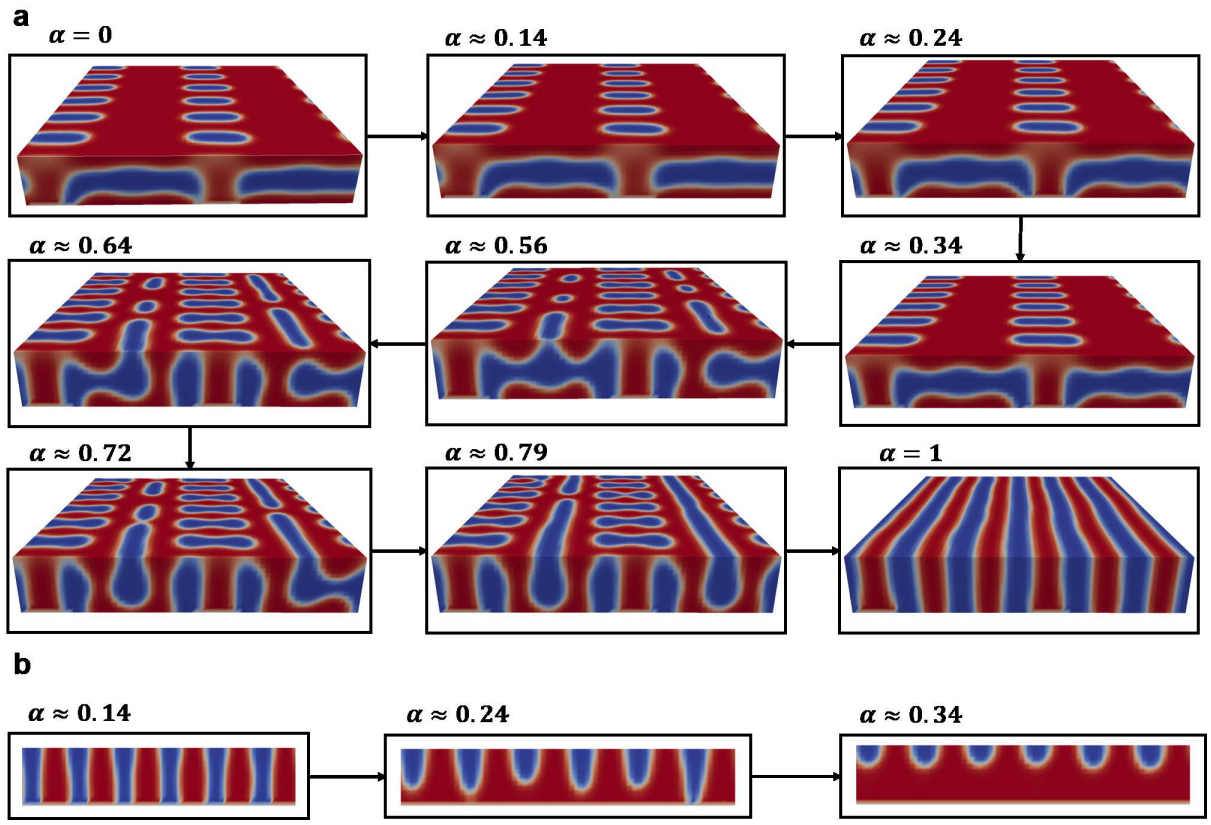

Figure 3.4: Representative morphologies of the MFEP from a fully stitched morphology to a fully aligned morphology. In **a** the view is looking down the y-axis at a slight angle, so that the top of the film in addition to a representative side view may be seen simultaneously. The transition that occurs from $\alpha \approx 0.14$ to $\alpha \approx 0.34$ cannot be adequately visualized from this view, so a representative slice of the image over a guiding stripe is represented in **b**. This view looks down the x-axis.

The half-stitched, half-lamellar morphology follows a similar mechanism, beginning its pathway of annihilation by displacing PMMA directly in contact with the guiding stripe so that PS will wet the guiding stripe entirely. Likewise, before further significant rearrange-

ments take place, this PS-layer grows upward. In contrast to the fully-stitched to fully aligned pathway, however, this process occurs with no significant free energy barriers. In the fully stitched to aligned pathway, the displaced PMMA must enter the horizontal PMMA layers over the background regions; however, when in contact with already formed lamellae, some of the displaced PMMA may instead enter a fully aligned PMMA lamellae. Furthermore, in the fully stitched to aligned case, the growth of the aligned PS-regions over the guiding stripes suggests the growth of interfacial area in contact with the horizontal PMMA-layers, and since it occurs throughout the entire film, four such interfaces grow simultaneously. By contrast, only one such interface grows when the half-stitch annihilates in contact with the aligned lamellae. Consequently this process occurs with far less significant free energy barriers. After the growth of an aligned PS region at the guiding stripe, the system enters a local free energy minimum at $\alpha \approx 0.41$. At this point, the horizontal PMMA domain has buckled, similar to the fully stitched system, and a small amount of PMMA has broken through to the free surface. The remainder of the buckling event entails climbing up a modest free energy barrier until the transition state at $\alpha \approx 0.57$; the barrier is of height $0.0099 \pm 0.005\ k_B T$ per chain. During this time, the buckling motion continues, while simultaneously orthogonal lamellae break up over the guiding stripe and begin to merge into nascent aligned lamellae. After sufficient growth in the direction of aligned lamellae has occurred, the process is entirely downhill in free energy, similar to the previous case, with representative snapshots of the system at $\alpha \approx 0.64, 0.72$, and 0.79 provided in the figure. As before, at $\alpha = 1$, through-film aligned lamellae are formed. Snapshots of the process are included in Figure 3.5.

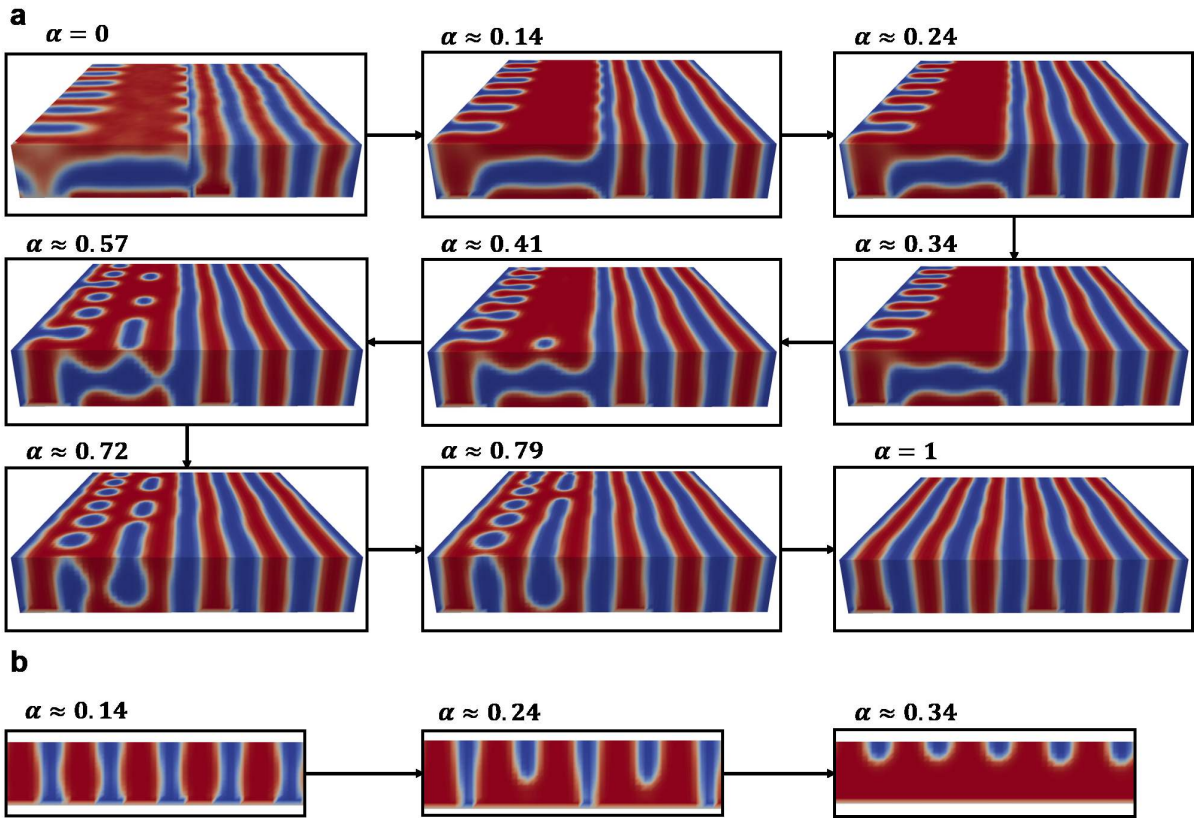

Figure 3.5: Representative morphologies of the MFEP from a half-stitched, half-aligned morphology to a fully aligned morphology. In **a** the view is looking down the y-axis at a slight angle, so that the top of the film in addition to a representative side view may be seen simultaneously. The transition that occurs from $\alpha \approx 0.14$ to $\alpha \approx 0.34$ cannot be adequately visualized from this view, so a representative slice of the image over a guiding stripe is represented in **b**. This view looks down the x-axis.

We now consider one additional pathway. Recent work[45] in the space of block copolymer defect annihilation has highlighted the importance of the initial path on determining the resulting MFEP. We therefore consider an additional string which has been initialized in the following way. The first half of the string is initialized as a linear interpolation in CV-space between the stitched morphology and orthogonally-oriented lamellae. The second half is initialized as a linear interpolation in CV-space between orthogonally-oriented lamellae and aligned lamellae. The two halves are joined together and updated as one string to an MFEP which includes as an intermediate state the orthogonally-oriented lamellae. The results suggest that more than one pathway competes by which stitches can annihilate into

aligned lamellae, with the possibility of forming a long-lived orthogonally oriented lamellae state via a barrier of similar size to the main barrier on the pathway proceeding directly from a stitched to fully aligned state. The presence of a larger barrier separating orthogonally oriented lamellae suggests this state would be long-lived once formed. The MFEP also presents different transition states as it annihilates (Figure 3.6). Of particular interest is that the first free energy barrier ($0.047 \pm 0.01 k_B T$ per chain) is of comparable value, or perhaps slightly smaller, than the main free energy barrier present on the pathway directly linking the stitched morphology to the fully aligned morphology. This first barrier is associated with the merging of stitched grains into orthogonal lamellae at the top of the film, as opposed to the buckling motion evident in the pathway proceeding directly from a stitched morphology to lamellae. The orthogonal lamellae, however, is quite stable compared to other metastable minima, and a free energy barrier of $0.19 \pm 0.014 k_B T$ per chain separates it from the aligned lamellae. This second, larger barrier is associated with connections forming between the orthogonal lamellae and slowly reorienting into aligned lamellae. Considering that there are at least two pathways with similar free energy barriers, we should expect the possibility of the stitched morphology annihilating via more than one mechanism. The experimental results also support this notion, as there is evidence for the stitch converting first into orthogonal lamellae before converting into aligned lamellae in the in-situ AFM data [103].

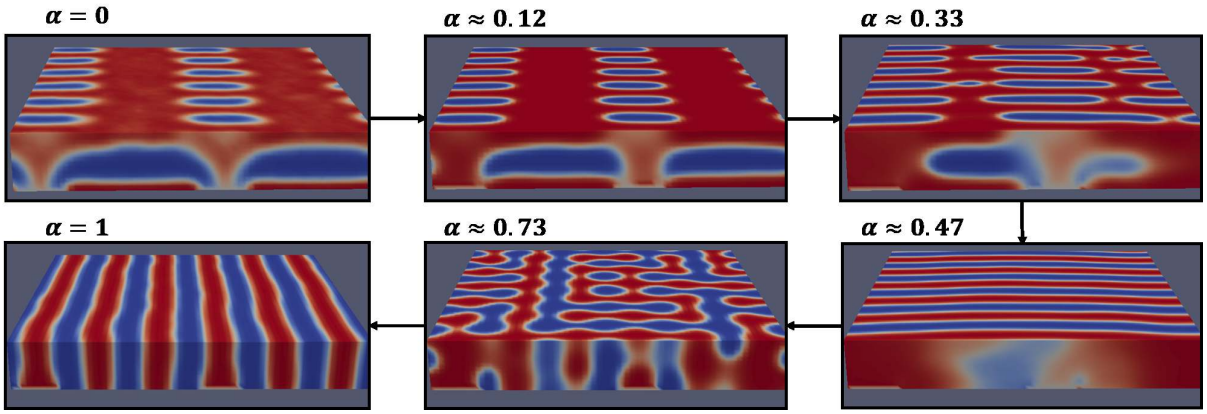

Figure 3.6: Representative morphologies of the MFEP from a fully stitched morphology to a fully aligned morphology, with an orthogonally-oriented lamellae intermediate at $\alpha \approx 0.5$. The view is looking down the y-axis at a slight angle, so that the top of the film in addition to a representative side view may be seen simultaneously.

From this detailed view, we can briefly comment on the in-situ AFM data presented in Raybin et. al[103]. First, we note that at the experimental temperature of 210 °C, the only (apparent) energy barrier on the half-stitched to fully-aligned MFEP can be converted to a value of 730 ± 370 kJ/mol (to convert, we take the numerical value of the energy barrier in absolute k_BT, substitute the numerical value of Boltzmann's constant in kJ/K, multiply by the temperature in Kelvin, and multiply by Avogadro's number). We note the order-of-magnitude agreement between our obtained average value and the experimental barrier of 360 ± 80 kJ/mol. Furthermore, we believe the detailed view of the qualitative nature of the transition sheds light on how aligned grains grow in experimental films. It is not immediately clear from the AFM data if each lamellae must grow one by one, each catalyzing the formation of the next; from the obtained MFEP, it seems that cooperative growth can occur at least one period into the stitched region, although of our observation of the cooperative growth is limited by the finite size of our periodic simulation box. Lastly, we note that the free energy barriers of a fully stitched morphology annihilating to a fully aligned morphology are an order of magnitude higher than if the system is already in contact with aligned lamellae, supporting the experimental observation that the stitched regions always annihilate from the

edges in contact with already aligned regions, never spontaneously from within.

At this point, we consider the formation of a stitched morphology from disorder. We have noted above that the presence of the chemical guiding stripes favors the formation of an aligned phase by about $0.04-0.09\ k_BT$ (per chain) compared to an orthogonally aligned or "sandwich" type morphology ; we therefore consider the appearance of the stitched morphology, which contains elements of both, to be kinetic in nature. Consequently, we generate a pseudo-dynamical trajectory initialized from a disordered state, with all constraints included, via a slightly modified Monte Carlo procedure in which the only Monte Carlo moves allowed are single-bead displacements. Additionally, we adjust the parameters of the model to enforce certain assumptions. Primarily, we enforce that the earliest dynamics are primarily surface driven, in accordance with the theoretical results of Müller et al. [89]. To do so, we initially set $\chi N = 0$ and $\sqrt{\overline{N}} = 5000$, the latter parameter being set high enough to dampen thermal fluctuations and approximate the mean-field limit. As we now consider pseudo-dynamical simulations, we also calculate the Rouse time (the time constant of the exponential decay of the end-to-end distance autocorrelation function for a melt of $N = 32$ homopolymers) and find that $\tau_R \approx 1000$ MC moves; we will quote simulations time henceforth in terms of τ_R.

It should be noted that the computational speed of the simulations is linearly proportional to $\sqrt{\overline{N}}$, and so this modification significantly slows down the calculations. Consequently, this state is simulated only for $20\tau_R$. After this, the system is quenched to $\chi N = 20$. While this is below the value of χN used to model the experimental system, it is above the ODT - we choose this value to allow the calculations to converge in a reasonable amount of time while simulation at such large $\sqrt{\overline{N}}$. After this initial quench (lasting $1\tau_R$), the system is simulated for an additional $20\tau_R$ before $\sqrt{\overline{N}}$ is reduced to 100 (approximately the value used elsewhere in this work, the value 100 chosen to simplify the procedure of deleting chains at random until the desired $\sqrt{\overline{N}}$ is reached). Finally, the system is simulated for $100\tau_R$. Structures at various points along the amalgamated trajectory are analyzed below and presented in

Figures 3.7, 3.8, and 3.9.

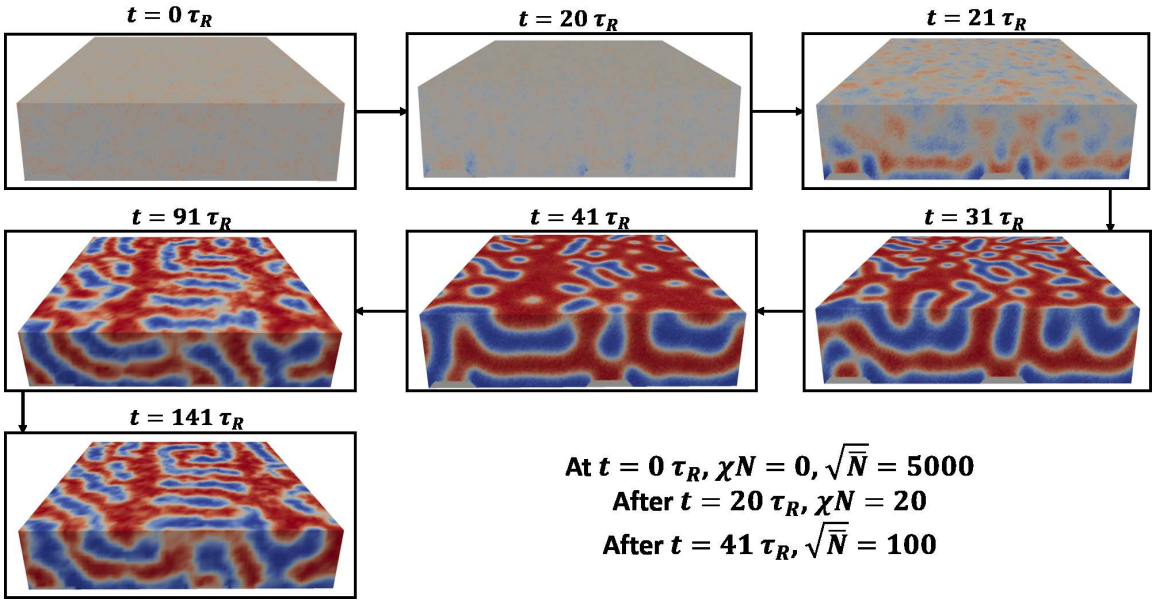

Figure 3.7: Morphologies along an amalgamated trajectory according to the procedure defined in the text. In these images, the y-axis runs into the plane of the figure, and the view is presented at a slight tilt so that the top of the film and the side may be viewed simultaneously.

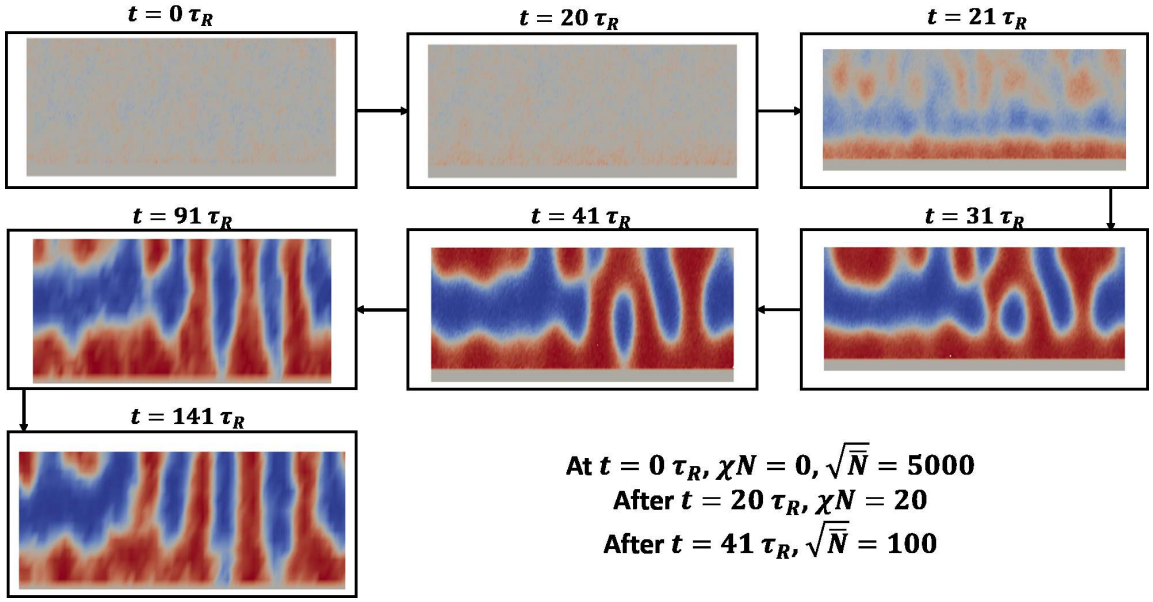

Figure 3.8: Morphologies along an amalgamated trajectory according to the procedure defined in the text. In these images, the x-axis runs into the plane of the figure, and the view is presented of a 2D slice taken over a guiding stripe.

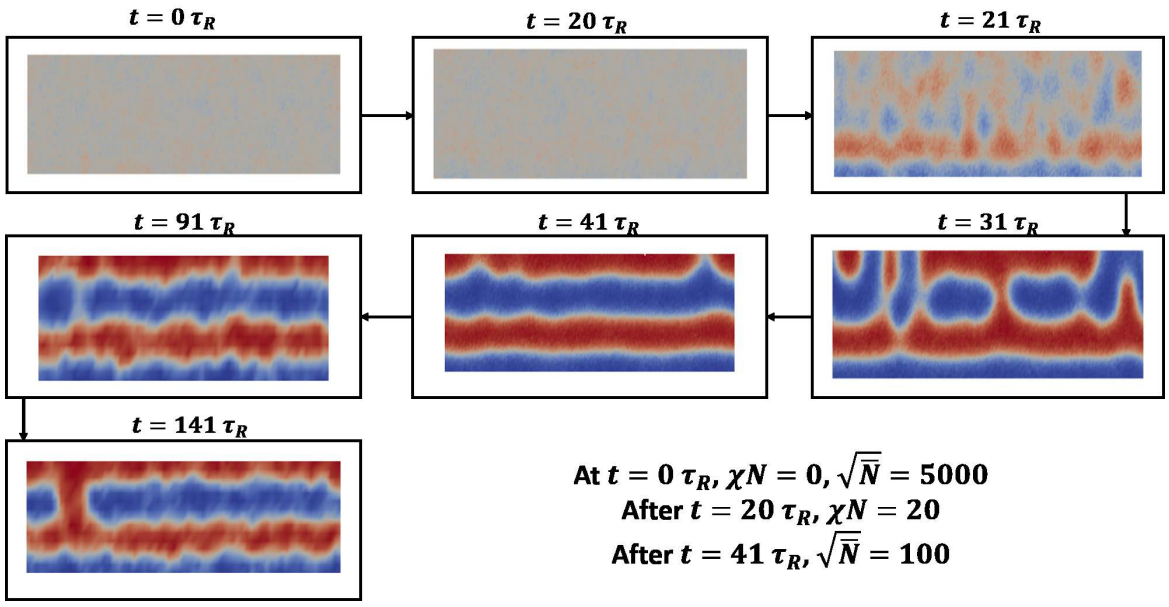

Figure 3.9: Morphologies along an amalgamated trajectory according to the procedure defined in the text. In these images, the x-axis runs into the plane of the figure, and the view is presented of a 2D slice taken over the background.

In the initial part of the trajectory, where $\chi N = 0$, a clear alignment of the block copolymer to the surface can be seen. In particular, around the guiding stripes, a layer of PS wets the top of the stripe and a layer of PMMA wets the guiding stripe sidewalls within $20\tau_R$. Meanwhile, some weak alignment of PMMA to the background layer can be observed just before the system is quenched. $1\tau_R$ after the quench to $\chi N = 20$ takes place, fairly strong alignment to the surface is seen in the lower half of the film. In particular, a well defined layer of PS wets the top of the stripe, while a well defined layer of PMMA wets the background layer, and even a well defined layer of PS can be seen to lay atop the PMMA on the background layer. Additionally, strong alignment of PMMA to the guiding stripe sidewalls can be seen in Figure 3.7. About $10\tau_R$ later, significant phase separation has occurred and the structures have become more well defined. Over the guiding stripe, there remains a layer of PS wetting the top of the stripe, but some structures resembling orthogonally oriented lamellae can be observed above this layer. The background layer continues to stratify into well defined parallel-oriented lamellae, and this continues until the

structure at $41\tau_R$.

At this point, parallel lamellae over the background are very well defined, and over the stripe, the structure resembling orthogonally oriented lamellae have grown. At this point, $\sqrt{\overline{N}}$ is reduced to 100, and the system evolves more dramatically because the free-energy barriers that are proportional to $\sqrt{\mathcal{N}}$ are reduced. After a further $50\tau_R$, over the guiding stripe, a clear region of fully orthogonally oriented lamellae have developed. Rather interestingly, PS has been displaced from wetting the guiding stripe in a few places in order to accommodate this orthogonal structure. A possible explanation for this phenomenon is that the orthogonally oriented lamellae over the guiding stripe can form an interface with the lamellae oriented parallel to the background which has the form of Scherk's first minimally periodic surface, which minimizes the interfacial area of the boundary. Lamellae which remained oriented aligned to the guide stripe would instead form a "T-junction" boundary, which is higher in interfacial energy [118]. Consequently, as it appears that the kinetics of the assembly process favor the formation of the parallel oriented lamellae over the background, it follows that the orthogonally oriented lamellae over the stripe form as the system tries to minimize the interfacial energy. By the final configuration shown, several orthogonally oriented regions are clearly visible, which extend down to the guiding stripe, with PMMA in direct contact with the stripe. Meanwhile, the background layer has remained well defined in a parallel orientation, with a small PS connection between the layers visible in Figure 3.9.

What is most remarkable about these results is simply that a morphology strikingly similar to the stitched morphology emerges in a simulation with only one assumption - that the early dynamics be surface driven. After making this assumption, the system naturally evolves into a state that combines aspects of the parallel, orthogonal, and aligned morphologies. Interestingly, at the end of the portion of the trajectory with $\chi N = 0$, the most noticeable feature is PMMA aligning to the guiding stripe sidewalls, suggesting this may be a key precursor to the stitched morphology. From this, it is clear that the formation of the

stitched morphology is consistent with theory, and should be regarded as an essential morphology along the pathway to fully aligned lamellae, given the topographical and chemical constraints of the system's pattern. Additionally, it can be noticed that some regions of the film appear to be aligning to the guiding patterns, suggesting that a mixture of stitched and aligned regions can be expected, consistent with experiments.

We do note one difference between the morphology which develops from this simulation and the one described experimentally [104]; here, we predict the background layer to be wet by PMMA (as the surface is attractive to PMMA), while experiments have suggested the background is wet by PS. We suggest that, if indeed the experimental surface is wet by PS, there must be some additional effect or unknown modification at the surface in experiments driving PS to wet the background substrate; however, this does not alter the fundamental result that the stitched morphology's formation is consistent with theoretical predictions. Alternatively, it may be that the experimental surface is wet by PMMA; further imaging experiments may reveal this to be so. Lastly, we comment that while PMMA wets the bottom substrate in our simulations, PS is in contact with air, consistent with experiments, and this occurs without making the the upper surface of the simulation box attractive to either block, as has been suggested [103] might be the case.

To summarize, after making the assumption that the early dynamics are surface driven, a morphology in which lamellae are found simultaneously in the parallel, orthogonal, and aligned orientation emerges from a pseudo-dynamical Monte Carlo simulation. This morphology bears a striking resemblance to the experimentally observed stitched morphology in contact with aligned lamellae. We consider this as essential validation that the stitched morphology cannot be considered an aberration arising from any experimental flaws but is instead predicted by a straightforward application of block copolymer theory. Furthermore, our results highlight the role of surface interactions in the early stages of structure formation, and suggest the possibility of tailoring the morphology induced by the surface interactions

in the earliest stages of DSA in order to template a defect-free morphology initially, rather than optimizing pathways of defect annihilation in the later stages.

3.4 Conclusions

We have simulated the experimentally observed stitched morphology as well as closely related morphologies with the aim of understanding how this morphology forms, why it is stable, and how it annihilates. By comparing the free energies of differently aligned phases under different constraints, we find that the template topography alone greatly reduces the preference for aligned lamellae over "sandwich" type lamellae and overall favors orthogonally oriented lamellae; however, the introduction of a chemical preference at the guiding stripes globally favors aligned lamellae by about $0.04 - 0.09\ k_BT$ (per chain) as compared to the orthogonally aligned or "sandwich" morphology, respectively, suggesting the formation of the stitched morphology is a purely kinetic phenomenon. We find that the stitched morphology faces substantially reduced free energy barriers toward annihilation when in contact with already aligned lamellae. These findings are in close agreement with the experiments of Raybin et. al[103] and Ren et al.[104]. We predict the stitched morphology to form from unbiased, pseudo-dynamical simulations resting only on the assumption that the early dynamics are surface driven, thus establishing the stitched morphology as a theoretically expected morphology given the constraints present in the system.

These results are expected to be highly dependent on the particular film thickness, as well as the particular guiding stripe topography used. The experimental observation of these relationships has been pointed out recently[104]. Further simulation work could focus on understanding how the assembly is affected by changing the film thickness as well as changing the height of the guiding stripes. Additionally, more complex guiding films could be considered which induce the global preference for alignment without seemingly inducing a preference for stitched-type morphologies to appear during the kinetic process of assembly. In

general, this work also underscores the need for carefully examining all sources of frustration to self-assembling materials. As the introduction of three different constraints on the self-assembly process of block copolymers gives rise to the unique stitched morphology, the addition of more or alternative constraints could further stabilize surprising, unexpected morphologies.

3.5 Methods

The theoretically informed coarse-grained (TICG) model for block copolymers used in this study has been detailed in prior literature [17]. In this model, the Hamiltonian of the system, H, consists of a term for the bonded energy (H_b), capturing interactions along the polymer backbone, as well as a term for the non-bonded energy (H_{nb}), capturing longer ranger intermolecular interactions. The bonded energy is given by:

$$\frac{H_b[\{\mathbf{r}_i(s)\}]}{k_B T} = \frac{3}{2b^2} \sum_{i=1}^{n} \sum_{s=1}^{N-1} [\mathbf{r}_i(s+1) - \mathbf{r}_i(s)]^2 \tag{3.1}$$

where the s^{th} bead on the i^{th} chain has position $\mathbf{r}_i(s)$. $b^2 = Re^2/(N-1)$ is the mean square bond length and R_e^2 is the mean squared end-to-end distance of the polymer chains; typically, a unit system is adopted for the simulations where the end-to-end distance is unity. k_B is Boltzmann's constant.

The non-bonded energy is given by:

$$\frac{H_{nb}[\phi_A, \phi_B]}{k_B T} = \frac{\sqrt{\overline{N}}}{R_e^3} \int_V d\mathbf{r} [\chi_{AB} N \phi_A \phi_B + \frac{\kappa N}{2} (1 - \phi_A - \phi_B)^2] \tag{3.2}$$

where $\sqrt{\overline{N}} = \frac{\rho_0 R_e^3}{N}$ is the interdigitation number, a measure of the number of chains each chain interacts with (ρ_0 is the average bulk number density of beads). The parameter χN is the Flory-Huggins parameter governing the incompatibility of the two blocks, and κ^{-1} is

proportional to the melt compressibility. Each term $\phi(r)$ is the local density of each type of bead. An order parameter $\Phi = \frac{\phi_A - \phi_B}{\phi_A + \phi_B}$ can be calculated in order to visualize a density field of the system using the software Paraview[2].

Additionally, substrate interactions may be added through terms of the form:

$$\frac{H_S}{k_B T} = \sum_{i=1}^{nN} f_s(x, y, K) \frac{\Lambda^K}{N d_s} \exp(\frac{-z^2}{2d_s^2}) \tag{3.3}$$

where K is the type of monomer bead; the term $f_s(x, y, K)$ adopts a value of either -1 or 1, depending on the value of K and the position of the bead. Λ^K defines the strength of interaction between the surface and the bead; when a bead of type A is in a position preferable to type B, the overall energy contribution should be positive, and $\Lambda^A = -\Lambda^B$. d_s is the decay length of the potential. In this work, we have three substrates - the PS-preferential guiding stripes, the PMMA-preferential sidewalls, and the PMMA-preferential background. Each polymer bead interacts with the surface which it is vertically above; z is therefore the vertical distance to the corrugated substrate.

Systems evolve via a Monte Carlo simulation; samples are generated and accepted or rejected based on the Metropolis criterion.

We chose the parameters $\sqrt{\overline{N}} = 83$, $N = 32$, $f_A = 0.5$, $\chi N = 35$, and $\kappa N = 25$ to describe symmetric PS-PMMA of approximate molecular weight 22K-22K g/mol and a bulk periodicity of 28 nm, annealed at 190 °C, following previous work with the model[53]. We find the bulk periodicity of the simulated system to be $L_0 = 1.72\ R_e$, establishing a conversion between real units and simulation units. The substrate is modeled with $\Lambda N_{stripe} = -0.1$, $\Lambda N_{sidewall} = 0.5$, and $\Lambda N_{background} = 0.1$ to capture a weakly PS-preferential top of the guiding stripe, a strongly PMMA-preferential sidewall, and a weakly PMMA-preferential background. The substrate is corrugated to capture the effect of guiding stripe topography; the tops of the stripes are $0.7L_0$ and are raised $0.14L_0$ off the background. Sidewalls are formed by adding right triangular prisms to the edges of the guiding stripes, the base of

which is $0.14L_0$, the hypotenuse meeting the top of the guiding stripe at a 45 $^\circ$ angle. The system is simulated with periodic boundary conditions in the x and y directions, but not in the z direction, to incorporate the effects of a real confinement on the system.

We use the string method in collective variables (CVs) [78, 90, 66] to compute minimum free energy pathways (MFEPs) from one state to another. A string is a series of images parameterized by α, the reaction coordinate - mathematically, $\mathbf{m}(\alpha)$ describes the string. Each $\mathbf{m}$ is a vector of CVs; our chosen CVs are the values of the order parameter Φ at each grid site defined on an identical but separate grid to the one used to calculate the non-bonded Hamiltonian. An image placed in CV-space experiences a force to reduce its free energy F. This free energy is defined as:

$$F(\mathbf{m}) = -k_B T \ln \int d\{\mathbf{r}^{nN}\} \exp(-\frac{H}{k_B T}) \delta[\mathbf{m} - \hat{\mathbf{m}}]. \tag{3.4}$$

With $\hat{\mathbf{m}}$ indicating the vector was constructed from the particle coordinates, while $\mathbf{m}$ is the value of the CVs associated with the string image. The condition for a path to be a MFEP is that $\nabla_\perp F(\mathbf{m}) = 0$. The string method algorithmically minimizes $\nabla_\perp F(\mathbf{m})$; first, a simulation system is constructed with the CVs associated with each string image and the system is simulated with a harmonic restraint (adding to the system Hamiltonian $\frac{H_c}{k_B T} = \frac{\lambda}{2} \int\limits_V d\mathbf{r}[\mathbf{m} - \hat{\mathbf{m}}]^2$; λ is a spring constant) to estimate the mean force on the image. The CVs of the image are updated in the direction that minimizes the force; the gradient of the free energy is $\frac{\delta F}{\delta \mathbf{m}} = \lambda \Delta L^3 k_B T[\mathbf{m} - \langle \hat{\mathbf{m}} \rangle_c]$, where $\langle \hat{\mathbf{m}} \rangle$ is a thermal average. The string is updated every iteration according to $\mathbf{m}_{k+1} = \mathbf{m}_k - \tau \lambda \Delta L^3 [\mathbf{m}_k - \langle \hat{\mathbf{m}} \rangle_c]$, where τ is a time constant controlling how aggressively the string is updated. Finally, a reparameterization algorithm is used, requiring that the images remain an equal arc length apart (in CV-space), preventing all the images from simply falling into a local free energy minimum. We make one adjustment to the method in this work; typically all images are free to move in CV-space. We find it useful to restrict the first image from moving. In the case of strings from

(meta)stable to states to other (meta)stable states, we find this improves the accuracy of the free energy calculation while not altering any of the information on the pathway, instead only adding a small (unphysical) region of the path where the provided morphology relaxes into a (meta)stable one. It is somewhat non-intuitive that this should be the case - we hypothesize that fixing the starting point in the initial stage of the calculation, when the string is not converged, may prevent string updates which "accidentally" move the string over the barrier that stabilizes the metastable state, leading to more consistent replicas of the string from iteration to iteration.

As a final note, we comment on estimating error within our string method calculations. We report all strings as the average of a set of strings obtained after the method has converged. In the main text, we provide a sense of the range of this set of strings by shading the region which encapsulates all strings within the set the averaging is performed over. In Figure 3.10, we provide another, more quantitative view of the error with an expanded discussion of possible sources of error. When we report differences in free energy in the main text, it is with this quantitative estimate of the error.

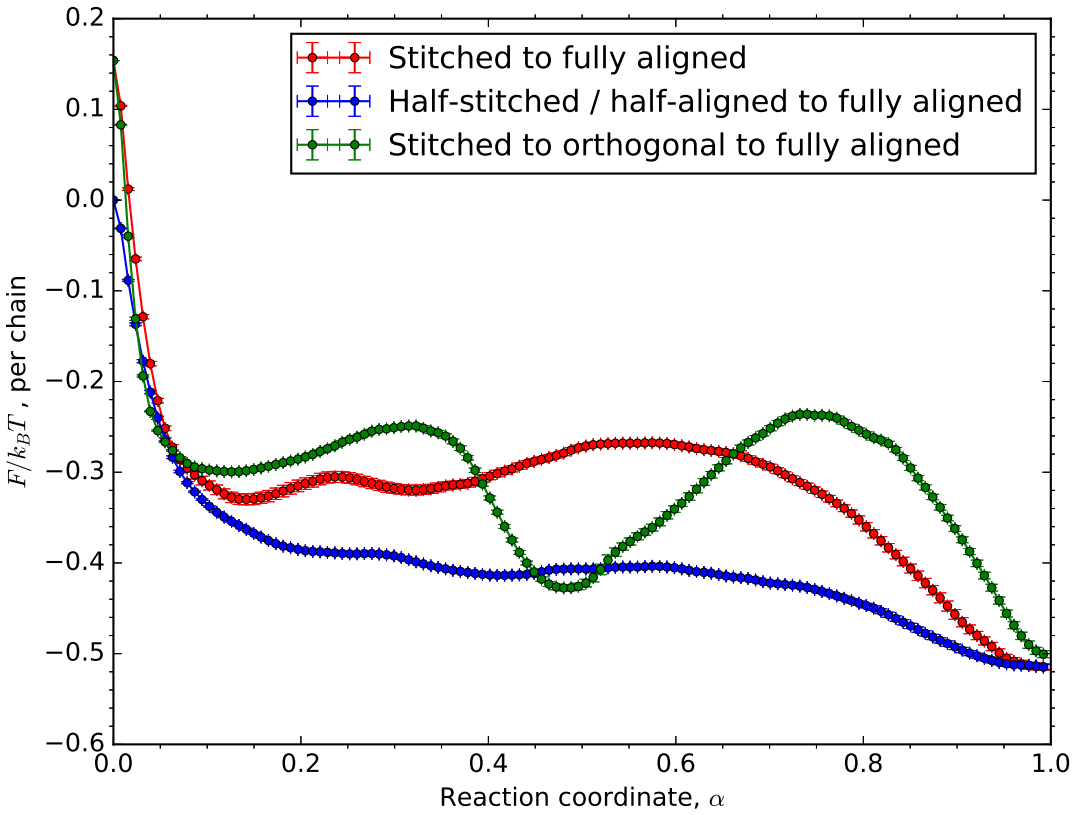

Figure 3.10: The minimum free energy pathways from the fully stitched to the fully aligned lamellae morphology (red), from the half-stitched / half-lamellae morphology (blue), and from the fully stitched to the fully aligned lamellae morphology with an intermediate state at $\alpha = 0.5$ of the orthogonally aligned lamellae (green). The value F at each value of α sampled from several iterations of the string method after convergence is averaged; the error bars are the standard deviation of the free energy from that same sample.

As discussed in the main text, we represent the MFEP as the average MFEP over a series of iterations run after the string has converged. Even post-convergence, there are small fluctuations iteration to iteration about some mean free energy profile, hence our decision to average the profile. Representing the error is a more challenging task. In the plot above, we have plotted the standard deviation of these free energy profiles. However, one could consider several other sources of error. For example, the value of free energy calculated at each image is dependent on the value calculated at the prior image; hence, there could be some propagation of error throughout the numerical integration process.

There are also such sources of error as finite sampling providing uncertainty to the free energy values obtained, as well as the finite spring constant used as a matter of practicality. As a general recommendation we advise against interpreting small free energy differences between different strings as meaningful but do point out the shape of each MFEP is quite consistent iteration-to-iteration, lending credibility to the interpretation of the features of each string.

CHAPTER 4

DYNAMIC SIMULATIONS OF THE "BRICKS-AND-MORTAR" MESOPHASE IN MIKTOARM BLOCK COPOLYMER/HOMOPOLYMER BLENDS

4.1 Abstract

A new mesophase in binary blends of $A-b-(BA')_3$ miktoarm star block copolymers and A homopolymers has recently been discovered experimentally and explored with field theoretic simulations. This mesophase evidently consists of aperiodic, visually discrete domains of A embedded in a continuous matrix of B up to very high concentrations of A. Because of the material's immense potential as a thermoplastic elastomer, deeper understanding of its dynamic properties, including its linear rheological behavior, response to shear, and response to uniaxial tension, is warranted. These properties are explored herein using dissipative particle dynamics in three dimensions, first establishing that the so-called "bricks-and-mortar" is predicted to form in such a simulation and then probing the dynamic and mechanical properties of the mesophase. It is established that the role of molecular bridging dominates the mechanical behavior and outweighs the influence of microphase segregation even at the highest homopolymer concentrations we study. Additionally, it appears that the bricks-and-mortar phase is destroyed by the application of sufficiently high shear, which may have ramifications for the processability of such materials.

4.2 Introduction

The self-assembly of block copolymers has attracted significant attention owing to their ability to form a rich variety of microphases at the nanoscale. Classically, the self-assembly of linear diblock copolymers has been studied for decades; the canonical phases formed

by such polymers include spheres, cylinders, gyroids, and lamellae [83]. More recently, increasing attention has been paid toward the self-assembly of block copolymers with multiple blocks or advanced architectures [7]. Precise control of these architectures enables continued engineering of block copolymers for a variety of applications [5], including photolithography [117, 86], photonic crystals [125], single molecule templates for nanofabrication [138], and thermoplastic elastomers [76, 116] (TPEs).

A key design goal for block copolymer TPEs is embedding a strong (glassy) reinforcing material in a flexible (rubbery) matrix for a material which is both strong and flexible [98, 76, 116]. Such a material would have both a high Young's modulus and high elastic recovery. At the microstructural level, these two quantities are most directly related to the overall volume fraction of the glassy phase in the material and the overall fraction of block copolymer chains which bridge evidently *discrete* microstructural domains, creating a physically cross-linked network [107, 97]. The simplest molecular architecture capable of producing the required microstructure is an ABA triblock copolymer; such an architecture is used for styrene-butadiene-styrene rubber, a common industrial product. Symmetric ABA triblock copolymers assemble into spherical, cylindrical, gyroidal, and lamellar mesophase (transitioning from one to the next with increasing f_A). The spherical and cylindrical phases (with visually A domains) are viable as elastomeric materials; the highest concentration at which a cylindrical phase with discrete A domains is observed is $f_A \approx 0.3$ [84]. The introduction of molecular asymmetry (up to a critical threshold above which the shorter A block is extracted from the A domains due to entropic considerations) to ABA triblocks leads to a deflection of the phase diagram such that the spherical and cylindrical phases with discrete A domains persist to higher f_A, up to $f_A \approx 0.4$ [82]. Fundamentally, this deflection is driven by the fact that a small bidispersity of the A blocks enables segregating more A polymer away from the AB interface without stretching the chains. It is also possible to deflect the phase boundaries through the introduction of non-linear architectures; for example, a

six-arm star polymer with one A block and five B blocks is predicted to yield a cylindrical phase with discrete A domains up to $f_A \approx 0.55$[33]. In this case, the deflection is driven by steric hindrance at the junction of the star polymers, which is eased in microstructures with curved interfaces. The results of combining these effects in $A(BA')_3$ was found[76] to yield cylindrical phases with discrete A domains up to $f_A \approx 0.6$ at extremely high asymmetry ratios between A and A'; the extraction of the A' block is suppressed by the increased preference for curved interfaces due to the star architecture.

Recently, it has been shown that blending this miktoarm copolymer with A type homopolymer which is intermediate in molecular weight between the short and long A blocks of the miktoarm yields a unique mesophase, dubbed the "bricks-and-mortar" (B&M) phase [115, 75], in which very high volume fractions of a dispersed phase remain evidently (visually) discrete in a continuous matrix of the low volume fraction phase, up to $f_A \approx 0.8$. That the homopolymer be intermediate in molecular weight between the short and long A blocks of the miktoarm is evidently essential to the phase behavior [115], which is attributed to the ability of the homopolymer to blend with the long blocks (wet-brush like [80]) while sequestering the shorter A blocks to the interface (dry-brush like [61]). The results of [75] suggest these two effects create an extremely close competition in terms of free energy for the lamellar and cylindrical phases; the coexistence between the two is destroyed by fluctuations, yielding the B&M phase. As a fluctuation stabilized mesophase, the B&M phase is similar to the more well known bicontinuous microemulsion [8, 41, 133, 87, 134, 28, 21, 26].

The architecture of this mesophase has considerable appeal as a TPE, necessitating detailed understanding of its structure and properties. The prior work reveals the existence and explores the thermodynamics of this phase while raising further questions. In particular, the existing experimental, theoretical, and simulated evidence regarding the B&M phase contains scarce information about three-dimensional structure. The experimental results rely primarily on cross-sectional TEM, while the existing theoretical and simulation results are

conducted in two dimensions. Through the use of dissipative particle dynamics, we explore the three-dimensional structure of the B&M phase, confirming its existence and approximate phase boundaries, exploring qualitative and quantitative properties of static structures (in particular, the fraction of bridging chains, a key quantity for elastomers, is calculated). Lastly, we explore a variety of dynamic properties of the phase, including the dynamic structure factor, its linear rheological behavior, response to nonequilibrium shear, and its response to uniaxial tension. We highlight the role of molecular bridging on the mechanical properties, and show that it plays a significant role up to the highest concentrations of homopolymer in the blend that we study. We also demonstrate the B&M phase is evidently destroyed by shear, an important consideration for processing such materials.

4.3 Results and discussion

The first essential task in exploring the properties of the B&M phase is to demonstrate that the phase exists using the chosen model in a 3D simulation. To this end, we simply allow large systems simulated using DPD (see below for full simulation details) to equilibrate in order to reveal the phase that exists at a variety of blend conditions.

Previous works studying the B&M phase [115, 75] demonstrate that the phase behavior of the miktoarm-homopolymer blends is most sensitive to the concentration of homopolymer (ϕ_h; in our work, the number density); hence, we study blend compositions from $\phi_h = 0.0$ to $\phi_h = 0.8$, in increments of $\Delta\phi_h = 0.1$. We also consider a slightly modified system in which the short A ends of the (BA') arms of the mitkoarm are replaced with B, resulting in a system with similar f_A yet which cannot form bridges (see below for further discussion of bridging and looping). We label this system $0.0, NB$ for non-bridging. Anticipating that as ϕ_h grows larger, so too will the domain sizes will grow quite large, we use a very large cubic simulation box (≈ 394 nm^3 per side, containing $\approx 3,000,000$ particles). Liu et al. [75] suggest that for a reference linear experimental polymer, the radius of gyration $R_g \approx 13.6$

nm; in our simulations we map a linear homopolymer of $N = 65$ to this reference linear polymer, and find that in simulation units $R_g = 3.56$. We can therefore relate all simulation units to experimental units through this correspondence. In particular, our estimate of the simulation box being ≈ 394 nm^3 per side is based on this measurement (in simulation units, the length per side is ≈ 103.5). The results of equilibrating for $1,500,000$ timesteps are presented in Figure 4.1 for representative homopolymer concentrations of $\phi_h = 0.0, 0.3$, and 0.6. The full range of ϕ_h values simulated is presented in Figure 4.2.

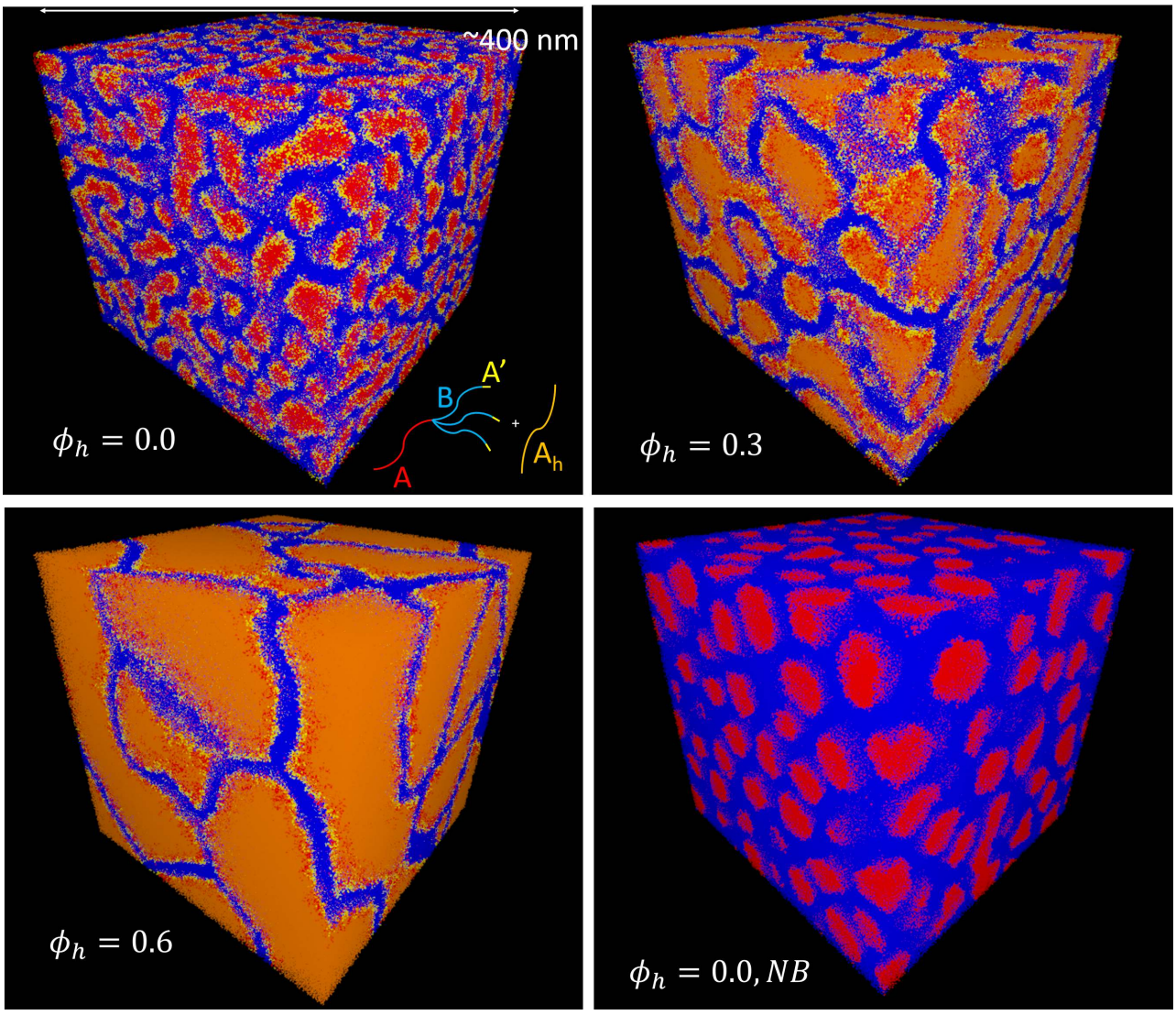

Figure 4.1: The phases resulting from long equilibration of selected blend compositions, as a function of the number density of homopolymer beads, ϕ_h. Bead identities are distinguishable by color - homopolymer beads are orange, long miktoarm tail beads are red, short miktoarm ends are yellow, and all type B beads are blue. The scale bar at the top of the figure indicates the dimension of the cubic simulation box, approximately 394 nm.

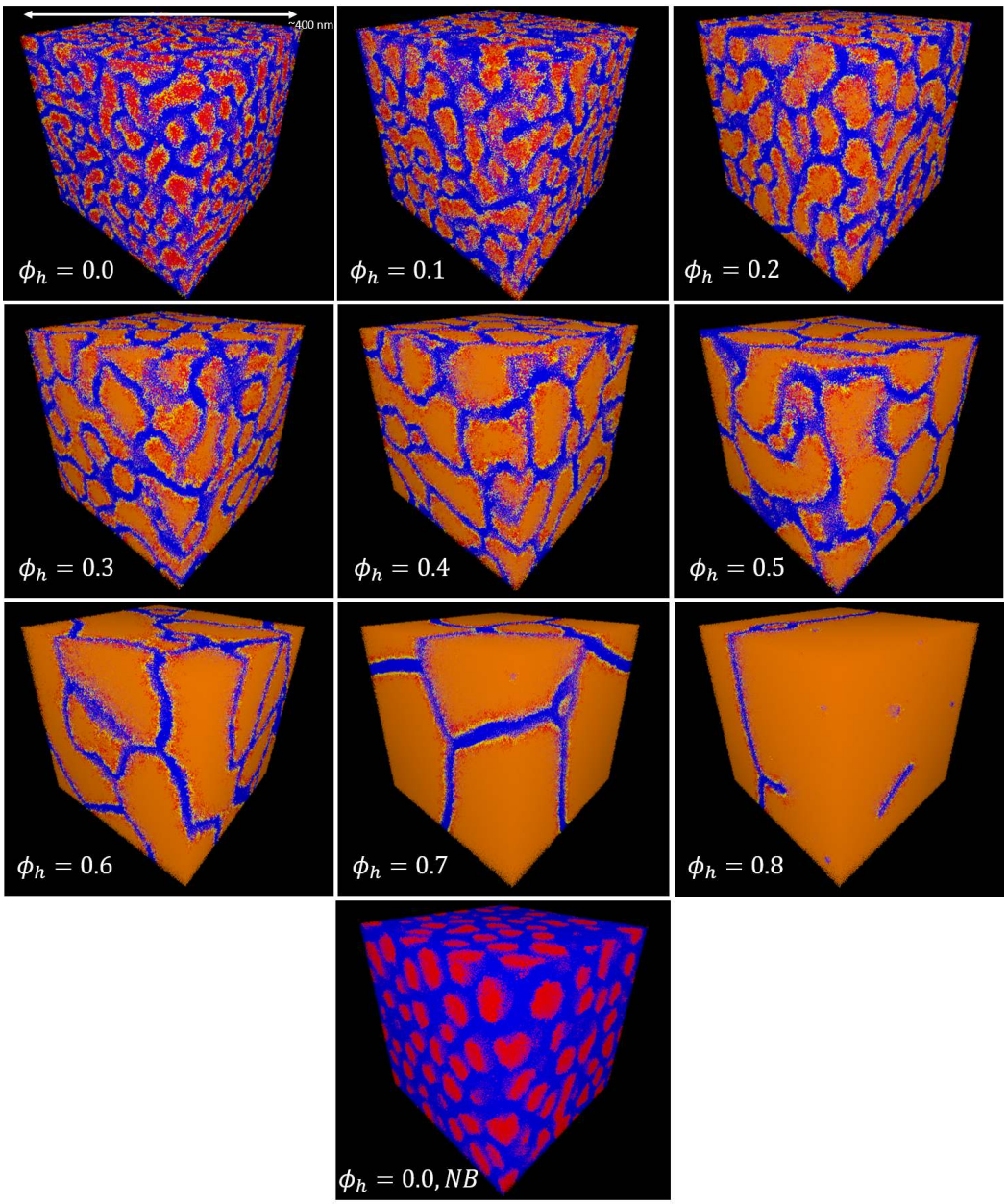

Figure 4.2: The phases resulting from long equilibration of all tested blend compositions, as a function of the number density of homopolymer beads, ϕ_h. Bead identities are distinguishable by color - homopolymer beads are orange, long miktoarm tail beads are red, short miktoarm ends are yellow, and all type B beads are blue.

4.3.1 Morphology classification

The first step is to understand the morphology of the self-assembled microphase separated melt. For mechanical properties there are two aspects to consider a) the connections es-

tablished via the network of chemical bonds and b) the load-bearing properties of the bulk phases. The diblock copolymer setup features two bulk phases with potentially different mechanical properties. The A phase is expected to be glassy and supports significantly more mechanical load as a result. If there is a continuous connection of the A phase through the entire system, the mechanical response of the system is dominated by this glassy component. Since this is pure bulk property perform the analysis with particle densities on a grid. For this purpose, we map the simulation configurations on a grid with the dimensions $50 \times 50 \times 50$. For each of the grid sites, the number of particles and their type is counted. The average number of particles per grid site is ≈ 26.59 and the fluctuations are small enough that none of the grid sites is empty. Subsequently, we can determine for each grid if it is dominated by A particles or by B particles.

To determine if the system exhibits structures of the glassy A material that can be load-bearing, we determine clusters of A grid sites. Sites that are A rich and are connected face-to-face are considered part of the same cluster. A cluster that connects through the simulation box along one of the axis is considered percolating and thus load-bearing in that direction. Further analysis can remove dead-ends from these clusters, which do not contribute to the mechanical response. The method employed here for this analysis is very similar to the method described in ref. [108].

Figure 4.3 plots the results of the percolation analysis. All morphologies investigated here feature a macroscopic cluster the is load-bearing in all three directions. Hence, the "bricks" are not truly disconnected from each other, but rather build a bicontinuous network that is load-bearing. The size of the percolating cluster is also large enough to contain almost all A particles of the system. This is reflected in the figure with the almost linear increase of the volume fraction with the fraction of A homopolymers. Only for the homopolymer free system, $\phi_h = 0$, shows a significantly smaller sized cluster. This indicates that the system indeed bricks from glassy A material but is still dominated by the percolating cluster. This

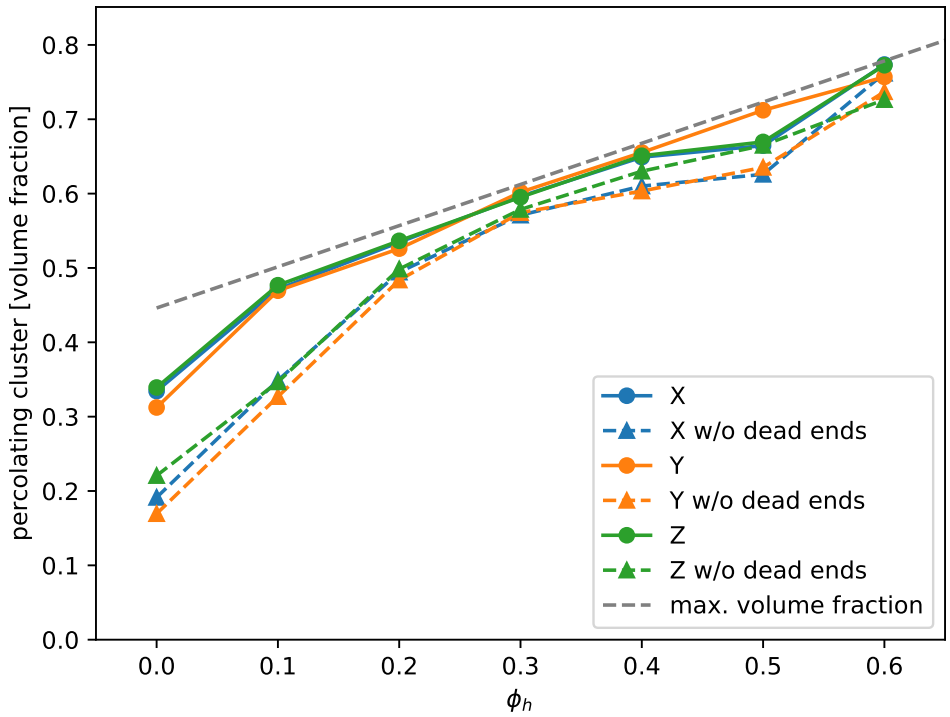

Figure 4.3: Size of percolating cluster of the glassy A phase in all three orthogonal directions. Results with dashed lines correct the volume fraction of the percolating cluster by subtracting dead-end that are not load-bearing. All morphologies have percolating clusters in all directions independent of homopolymer swelling ϕ_h. Hence, the "bricks" of the B&M phase are connected and do not form a true B&M phase, which does not necessarily impede the beneficial mechanical properties.

is consistent with early findings with simpler diblock copolymer architecture but similar volume fraction [108].

Even with the percolating clusters, the true load-bearing potential of these clusters is yet unclear. The DPD model we employ is soft and thus unable to form a glassy state. Instead, we use further analysis of the previously identified clusters by a bottleneck analysis. The mechanical response in one direction is dictated by the amount of glassy material that can support the load. Dividing the percolating cluster into slaps perpendicular to the load direction can identify the smallest amount of load-bearing material limiting the load-bearing. This bottleneck can be a single strand or it can be composed of multiple strands as long the strand forms a continuous connection in the direction of the load.

Figure 4.4 presents the results as a function of the fraction of the filling homopolymer

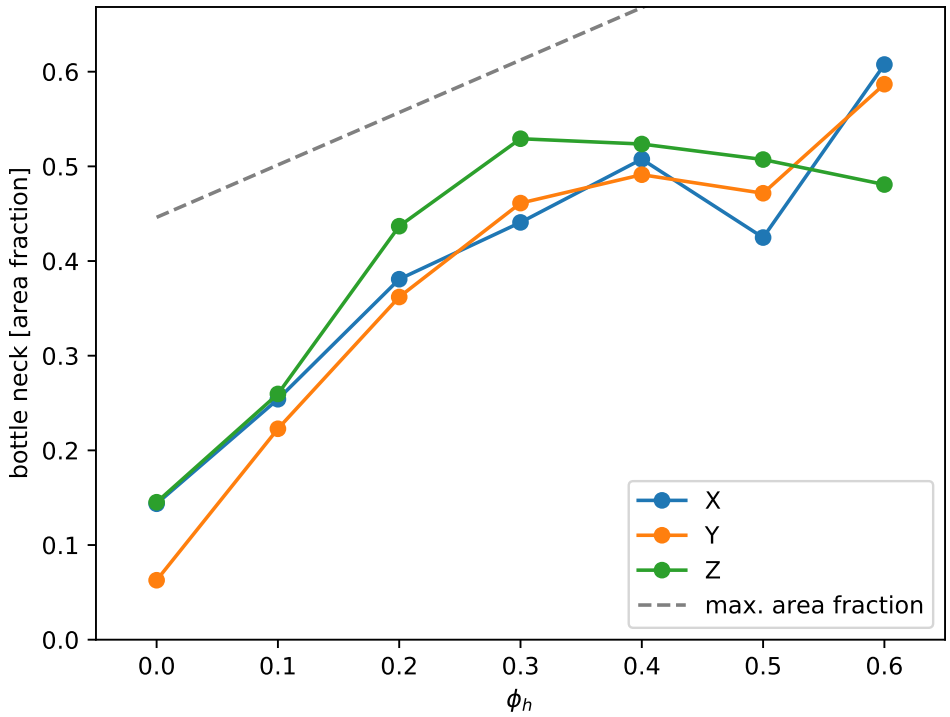

Figure 4.4: Area fraction of the smallest load-bearing connection perpendicular to the load direction of the glassy A material. Varying fraction of homopolymer ϕ_h leads to a linear increase of the bottle-neck size.

ϕ_h. The bottle-neck size increases with the homopolymer, hence the homopolymer not only swell the bricks in the morphology but also contribute to the strength of the glassy material. We expect the strength of the material to be proportional to the Young's-modulus of the bulk A material times the area fraction. Hence, we are predicting an increase in strength with the inclusion of the homopolymer to the miktoarm system.

The pure miktoarm melt ($\phi_h = 0.0$) assembles into a (defective) hexagonally packed cylinder phase. We validate that this is a regularly ordered, periodic phase through the calculation of the structure factor (considering only type A beads), $S(\boldsymbol{q})$ (see Figure 4.5 and Figure 4.6). The structure factor computed for $\phi_h = 0.0$ has a clear peak around $q = 0.18$ nm^{-1} (corresponding to a domain spacing $D = \frac{2\pi}{q} = 35$ nm). The same is true when a small amount of homopolymer ($\phi_h = 0.1$; Figure 4.6) is introduced into the blend, with the peak shifting to smaller q, consistent with the average domain size increasing. The low q peak flattens and becomes indistinct at ($\phi_h = 0.2$; Figure 4.6), and disappears entirely

for $\phi_h = 0.3$ and above, suggesting the lack of a regularly ordered periodic domain. It is also possible that, if a peak did exist, it has shifted too far to the left to be resolved using the current system size (the smallest value of q that can be probed is the linear system dimension). We therefore acknowledge the possibility that finite size effects could set in as early as $\phi_h = 0.3$. However, visual inspection of the phases that appear for $\phi_h = 0.3$ are consistent with prior observations of the B&M phase, with large, evidently (visually) discrete, irregularly shaped domains of bead type A embedded in a continuous matrix of bead type B. The above percolation analysis suggests, however, that while visually discrete, the A domains in fact form a percolating cluster. Such behavior persists up to $\phi_h = 0.7$ (Figure 4.6), at which point the A domains are so large the simulation box boundaries are certainly too small to properly capture these phases - hence, we will limit quantitative analysis of these phases to blends at or below $\phi_h = 0.6$. We note there is some visual suggestion of the appearance of micelles with a core of type B appearing at $\phi_h = 0.8$ (Figure 4.6), consistent with Liu et al.[75]

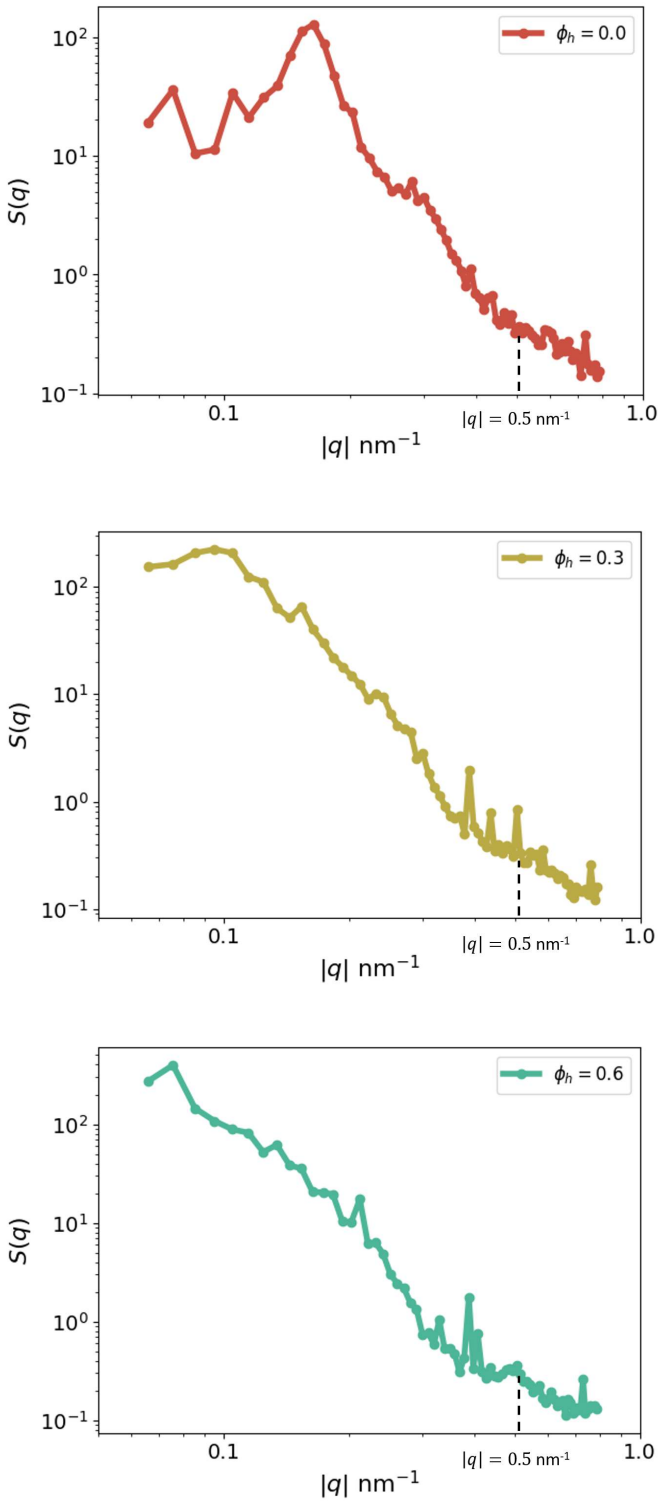

Figure 4.5: The structure factor $S(\boldsymbol{q})$ (computed from only type A beads) corresponding to the phases represented in Figure 4.1, as a function of the number density of homopolymer beads, ϕ_h, for selected ϕ_h.

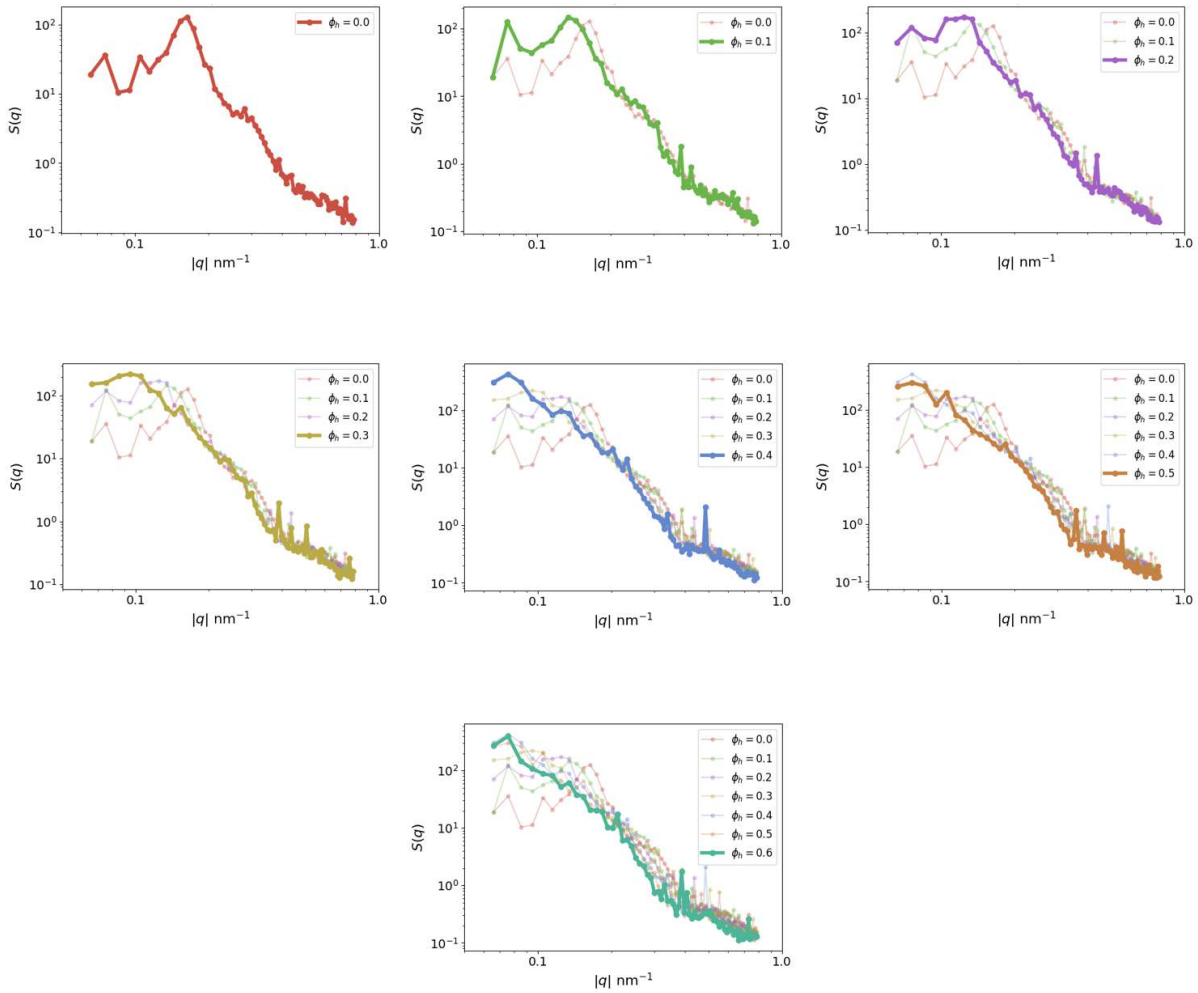

Figure 4.6: The structure factor $S(\boldsymbol{q})$ (computed only from type A beads) corresponding to the phases represented in Figure 4.1, as a function of the number density of homopolymer beads, ϕ_h. Each new structure factor is plotted in succession over the prior curves for comparison. Our analysis is limited up to $\phi_h = 0.6$ to avoid finite size effects.

In addition to the low q peaks in $S(\boldsymbol{q})$ present at low ϕ_h, there is also consistently a plateau region centered on $q = 0.45$ nm^{-1} (corresponding to ≈ 14 nm) present for all blend compositions. This suggests the existence of a common universal length scale associated with the miktoarm chains (as it is present at the $\phi_h = 0.0$ condition as well). We associate this plateau, or very diffuse peak, with the thickness of B domains. We can quantify this notion by calculating $\sqrt{\langle R_e \rangle^2}$ associated with the B blocks only; at $\phi_h = 0$, $\sqrt{\langle R_e \rangle^2}_B = 3.39\ r_{cut} = 12.9$ nm, corresponding to $q = 0.49$ nm^{-1}, agreeing well with the approximate

center of the plateau.

We also probe the distribution of miktoarm chain conformations (see below for details). As noted in our discussion of the calculation, we can identify both a bridging fraction based on the *fraction of arms bridging* (ν_b) and a different bridging fraction based on the *fraction of chains with at least one arm bridging* ($\nu_{b,chains}$). The latter quantity is most often cited as the "bridging fraction" for multiarm copolymers, though we note the former may be more relevant for understanding the impact of a bridge on the elastic properties. We show both quantities in Figure 4.7.

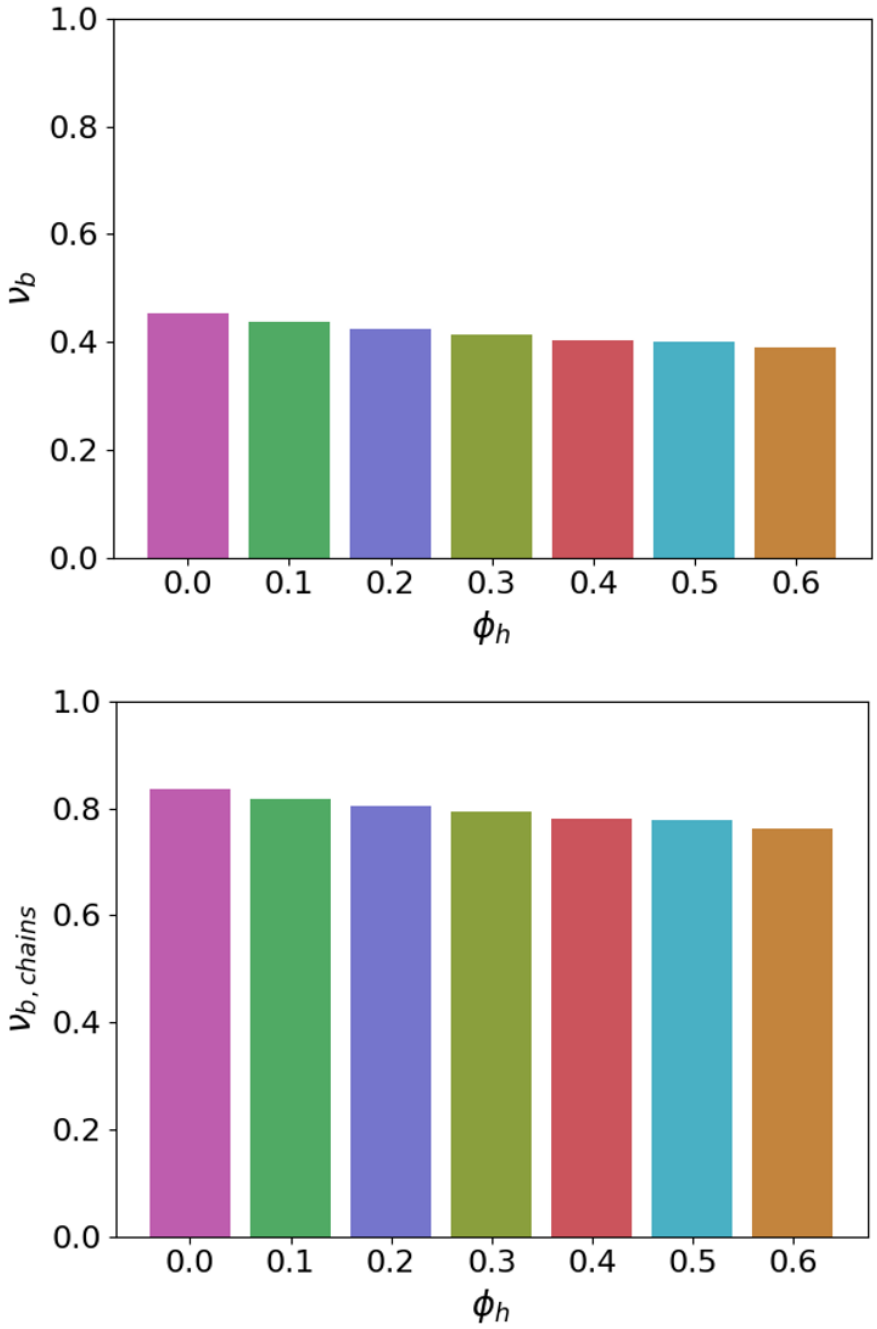

Figure 4.7: Relative bridging fractions consider as a fraction of arms bridging (above) and as a fraction of chains with at least one arm bridging (below), for each studied value of ϕ_h.

Interestingly, we find that there is a significant gap between ν_b and $\nu_{b,chains}$, suggesting there are many chains in which some arms bridge and some arms do not. If we consider $\nu_{b,chains}$, we find that for all phases, whether cylindrical or B&M, the *relative* proportion of

bridging chains is at least 70%; the absolute proportion of course decreases with increasing ϕ_h, as miktoarm chains are replaced by homopolymer chains. Some comparisons (at $\phi_h = 0.0$) can be made to calculations made for other block copolymer architectures; for four-arm star diblock copolymers forming lamellae, Hart et al. [40] found a bridging fraction of ≈ 80 %, quite similar to our estimate for the cylindrical phase formed from the miktoarms considered in this work. We note that the decrease in relative bridging proportion as the B&M phase forms may be considered similar to the trend previously shown in the literature[4] in which the bridging proportion decreases in copolymer mesophases as the interfaces flatten. Recently, using field theoretic simulations, the bridging fraction for two-dimensional bricks and mortar phases was computed by Lequieu et al. [62]; our results agree quite well, with similar values of the bridging fraction and the same trend of a slight decrease with the onset of the bricks and mortar phase. Of most importance, we note that the high relative bridging proportion that persists to the highest volume fraction we consider suggests that even at high ϕ_h the B&M should be expected to display significant elasticity.

Next, we also consider the discreteness of the A domains from a quantitative perspective. As noted above, for each ϕ_h considered, we perform a cluster analysis to determine the number of unique clusters. Interestingly, for each condition considered, we find only one cluster, suggesting the A domains are not discrete but are in fact continuous. While this observation contradicts prior understanding of the phase, it is worth considering the origins of this evident continuity further. Visual inspection (Figure 4.8) of the phases, in particular slice by slice visualization of thin, pseudo two-dimensional slices of the material, reveal that in any given 2D slice of the morphology, the "brick" domains are indeed visually discontinuous; which is compatible with the prior literature [115, 75]. However, our cluster analysis suggests that this two-dimensional picture is insufficient, and that in three domains there is one percolating cluster. We note that experimental stress-strain experiments on the bricks-and-mortar phase reveal some amount of plastic deformation at any blend composition;

we suggest this plastic deformation represents the breaking of the single large cluster into multiple smaller clusters. Furthermore, we also suggest that a mesoscopically continuous A domain does not prevent molecular bridging between locally discontinuous A domains, enabling the bulk behavior of an elastomer. From this perspective, we consider an analysis of the B&M phase dynamics with a special attention on the role of bridging to be critical. As a note, from this point forward, we continue to refer the B&M phase as such, despite the existence of a single percolating cluster suggesting that the "bricks" embedded in "mortar" picture is not quite accurate. We maintain this notation for simplicity and continuity with prior work.

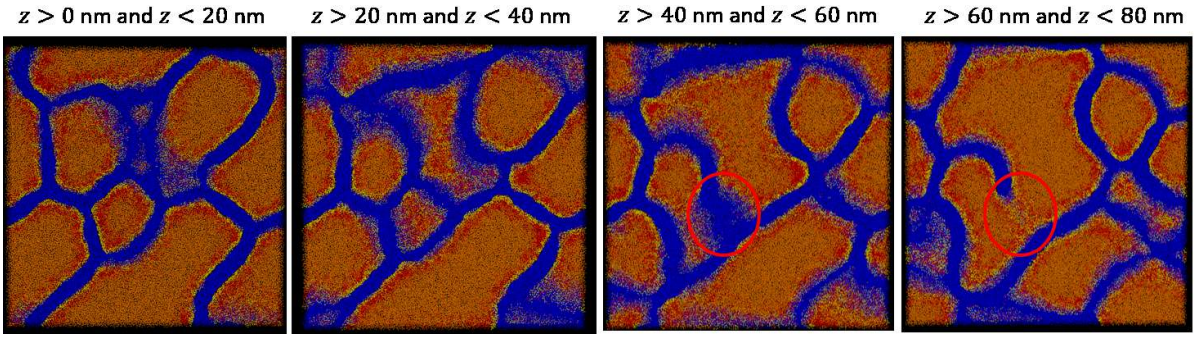

Figure 4.8: Pseudo-2D slices in the xy-plane of a bricks-and-mortar morphology at $\phi_h = 0.4$, starting from the middle of the morphology ($z = 0$) and moving upward in 20 nm increments. Red ellipses indicate a region where in one slice, two domains may appear disconnected, but in another slice, it is revealed that they were in fact connected by a homopolymer-depleted connection. Bead identities are distinguishable by color - homopolymer beads are orange, long miktoarm tail beads are red, short miktoarm ends are yellow, and all type B beads are blue. The x and y dimension of the slices is the same as the total x and y length of the simulation box.

Having established the existence of the B&M phase in our 3D model and having calculated some important (static) structural quantities of the B&M phase, we now consider its dynamic properties. We begin by calculating the viscosity of both the ordered phase as well as of blends in which $\chi N = 0$, to allow an understanding of the impact of microstructure formation on dynamic properties. As noted above, we also consider one additional system - a neat miktoarm blend in which the terminal A ends of the miktoarm are replaced by B, resulting in a miktoarm of the same architecture and similar f_A but incapable of bridging; This allows

ϕ_h	$\chi N = 0$		$\chi N \approx 160$	
	$\eta_{\text{Müller-Plathe}}$	$\eta_{\text{Green-Kubo}}$	$\eta_{\text{Müller-Plathe}}$	$\eta_{\text{Green-Kubo}}$
0.0	11.9	12.1	24.4	80.6
0.1	11.1	11.5	22.0	65.2
0.2	10.7	9.8	19.0	32.8
0.3	10.0	8.7	17.0	30.3
0.4	9.3	8.2	13.8	29.9
0.5	8.6	7.8	11.5	27.6
0.6	8.0	7.7	9.2	12.7
$0.0, NB$	-	-	19.8	53.4
1.0	-	5.1	-	-

Table 4.1: Viscosities calculated for various blend conditions with and without microphase separation. For viscosity calculated via nonequilibrium simulations with the MP method, a consistent shear rate ($\approx 0.005\ \tau^{-1}$) is applied (τ is the unit of DPD time). We note that the velocity profile resulting from the applied momentum flux is, in all cases, well fit to a linear function. Lastly, note that in the absence of microphase separation, the properties of 0.0 and $0.0, NB$ are identical.

us to probe the role of molecular bridges on the dynamic properties independent of the effects of molecular architecture or microphase separation. As described below, we obtain the viscosity η in two ways - via nonequilibrium simulations using the Müller-Plathe (MP) method [91] and via equilibrium simulations using the Green-Kubo (GK) method [70, 48]. This enables an understanding of the possible role of shear thinning. The viscosities obtained using both methods for both blends are included in Table 4.1.

In Figure 4.9, we provide representative velocity profiles and linear fits as well as raw auto-correlation function data with fits (see discussion below) to provide a qualitative representation of the errors associated with fitting and therefore the viscosity values presented here. The linear fit agrees excellently with the data, and thus obtained viscosities are precise. There are two sources of discrepancy between the fit and the raw data. First, the raw autocorrelation function displays oscillatory behavior in the time range between $t = 10^{-1}$ and $t = 10^0 = 1$. This oscillatory behavior is often associated with bond-length relaxation in systems where inertia is significant (underdamped dynamics). This is not typically the case in DPD simulations; in disordered melts, we do not observe these oscillations. We

therefore associate this behavior with the relaxation of bonds at interfaces. In any event, fitting this behavior is not expected to be important for estimating the viscosity, and so we fit to a purely multi-exponential model. The other source of potential error is in the long time relaxation beyond $t = 10^2$; there are progressively fewer and fewer samples separated by such long times from which to calculate the autocorrelation function, and the uncertainty in the autocorrelation function value grows. It is therefore difficulty to accurately fit in this region, and this will impact the accuracy with which viscosity can be estimated. Therefore our discussion of viscosities in the main text should be understood in the context of some uncertainty associated with fitting the long time relaxation modes.

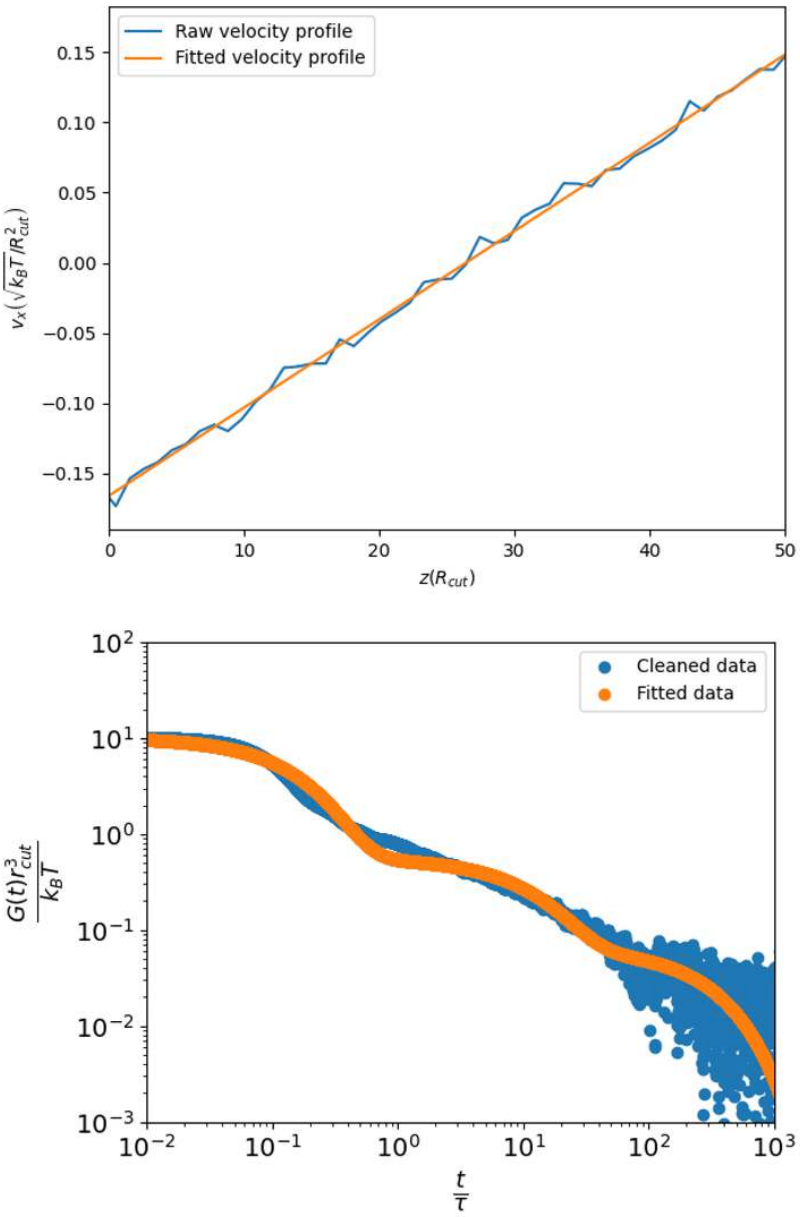

Figure 4.9: Above, a velocity profile of the upper half of the simulation box (both raw data and a fitted linear function) obtained from a Muller-Plathe simulation for the blend composition $\phi_h = 0.0$ and below the order-disorder temperature. Below, $G(t)$ (the autocorrelation function of the off-diagonal components of the stress tensor) both as raw data and a fit to the Generalized Maxwell Model is presented for the $\phi_h = 0.5$ blend at the same temperature.

We begin by noting there is a larger uncertainty associated with the Green-Kubo viscosities, as they are obtained by fitting to noisy data (especially at long times); we could also obtain the viscosity by direct numerical integration, but the noise would still create

uncertainty[132]. Therefore, when shear plays little to no role on the calculated quantity, we prefer the MP method. This is the case for the blends at $\chi N = 0$, where the influence of shear appears negligible; the value of viscosity of viscosity obtained from GK is sometimes higher, sometimes lower than the value obtained via MP. In either case, there is a clear trend toward decreasing viscosity as an increasing proportion of homopolymer constitutes the blend; this is natural, as DPD polymers essentially behave as Rouse polymers [120]. The observed Rouse behavior suggests the decomposition of shear-stress relaxation — a collective quantity — in terms of independent single-chain contributions. The viscosity will therefore scale with the longest relaxation time of the constituent polymers weighted by their relative proportions. Ergo, a higher proportion of (shorter) homopolymers in the blend leads to increasingly lower viscosity. We also include in our Green-Kubo based analysis the pure homopolymer case ($\phi_h = 1.0$) and note that the blend viscosities at $\chi N = 0$ agree very well with a standard mixing rule of $\log \eta = \phi_h \log \eta_{homopolymer} + (1 - \phi_h) \log \eta_{miktoarm}$.

By contrast, the influence of shear is, evidently, highly non-negligible for the case of the ordered mesophases. Visual inspection (Figure 4.11 and Figure 4.12) of the morphology of the blends after the application of shear quickly reveals why this is so. The cylindrical phases which form at low ϕ_h align to the direction of the shear; hence, the viscosity becomes anisotropic with respect to the shear direction. As we, of necessity, measure the viscosity parallel to the shear (or alignment) direction, this is associated with a significant reduction in the viscosity compared to the cylindrical phase we measure at equilibrium, in which the domains lack a regular alignment direction. Another phenomenon entirely seems to underlie the reduction in viscosity for at higher ϕ_h. Beginning at $\phi_h = 0.2$ (Figure 4.12), after the application of shear, the phases no longer resemble a B&M morphology at all, but instead a bicontinuous phase. This phenomenon fits into a broader category of shear induced phase transitions that has been observed in other systems, including blends of block copolymer and homopolymer [38]. That the B&M phase is apparently quite sensitive to shear may bear

relevance to the processability of materials trying to exploit this microstructure. Also of interest is that the role of bridging is apparently fairly weak for the viscosity of the ordered phases undergoing significant shear, as the viscosity of the $0.0, NB$ phase is nearly the same as the viscosity of the 0.0 phase. On the other hand, as discussed in more detail below, the equilibrium (or zero-shear) properties are strongly affected by molecular bridging.

To further contextualize these results, we calculate the dynamic structure factor $S(\boldsymbol{q}, t)$ for the $\phi_h = 0.0$ blend at $\chi N \approx 160$ at $|q| \approx \frac{2\pi}{10} = 0.63$ (in simulation units), corresponding to the peak in the static structure factor near $q = 0.18$ nm^{-1}. By fitting the structure factor to a sum of exponential functions, we calculate a morphological relaxation time from this function of $\tau_r \approx 1800\tau$, that is, a time scale on which composition fluctuations of the morphology relax (see Figure 4.10). In the case of $\phi_h = 0.0$, we can then contextualize the shear calculations as taking place at a Weissenberg number ($Wi = \tau_r \dot{\gamma}$)) of $Wi \approx 10$. As there is no peak in the static structure factor for most blend compositions, we do not calculate a morphological relaxation time for other compositions, but we can make some scaling arguments; the relaxation time should go as $\tau_r \approx \frac{\nu}{q^2}$, where q is the domain size. While the domain size becomes ill-defined, it certainly increases by up to an order of magnitude at the higher ϕ_h values. At the same time, the viscosity decreases by nearly an order of magnitude. We therefore expect that, as an upper bound, τ_r could increase by an order of magnitude overall for intermediate to high ϕ_h values. Consequently, $Wi \approx 100$ serves as an upper bound for contextualizing these dynamic calculations. From this we conclude our shear calculations are in a hypothetically experimentally accessible regime, though we note (with further discussion below) that the morphological relaxation time is likely higher in experiments due to the glassiness of the dispersed domains.

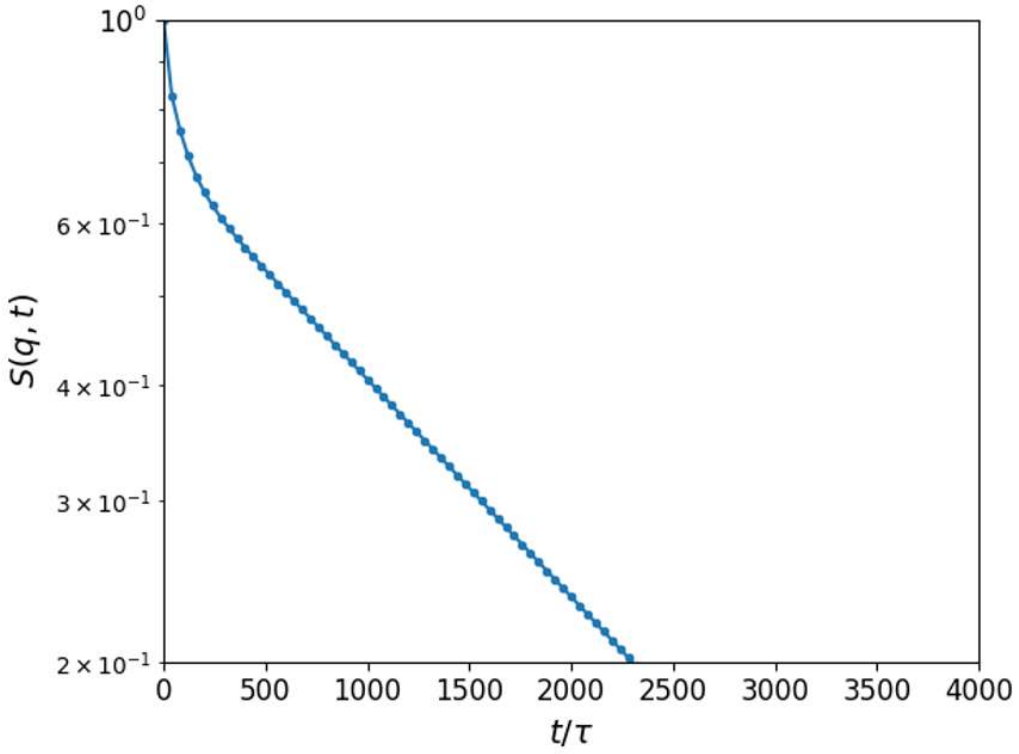

Figure 4.10: The fitted dynamic structure factor for the $\phi_h = 0.0$ blend at $\chi N \approx 160$. The fit is a sum of three exponential functions; the longest time constant of the fit is taken as the morphological relaxation time.

Interestingly, performing a cluster analysis similar to the one performed above, but now using the post-sheared configurations, reveals that there are now multiple truly discrete A domains. This is no surprise for the aligned cylindrical morphologies, where the shear has aligned them and annealed defects out such that discrete cylinders are now hexagonally packed. At higher blend compositions, the A domains appear visually somewhat more mesoscopically continuous; however, up to $\phi_h = 0.5$, there remain multiple A domains. We suggest this is mainly a function of the shear flow created a preferred aligned direction; as the A domains are driven to align to the shear direction, they will have difficulty maintaining complete percolation.

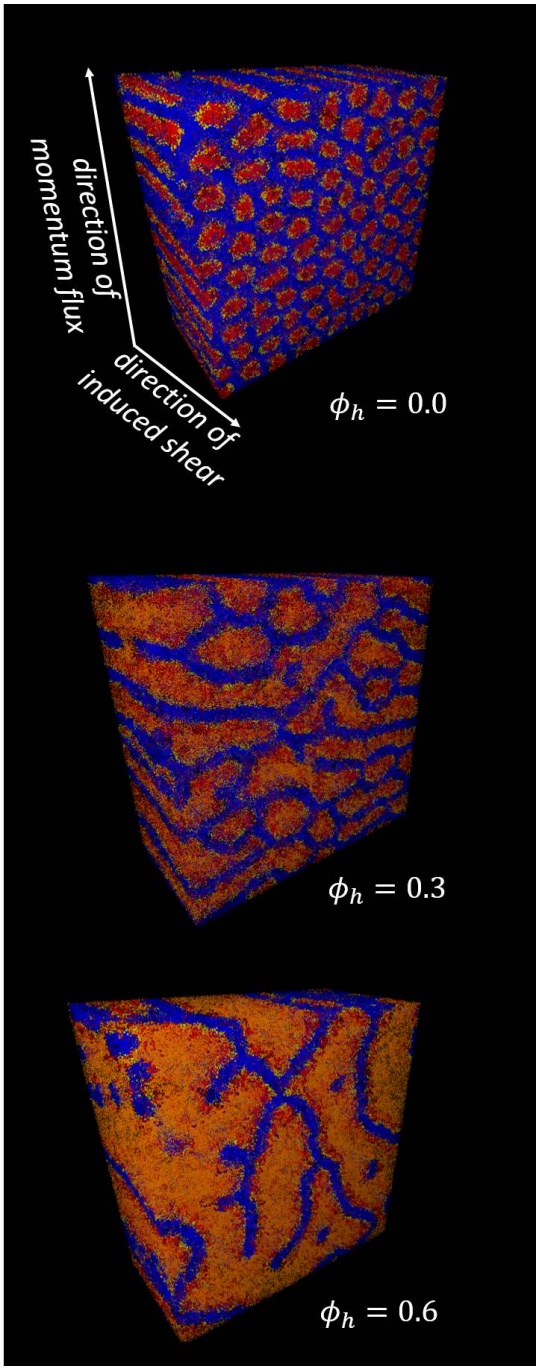

Figure 4.11: The phases resulting from long application of shear to select blend compositions, as a function of the number density of homopolymer beads, ϕ_h. The images are sliced along a plane perpendicular to the shear direction. Bead identities are distinguishable by color - homopolymer beads are orange, long miktoarm tail beads are red, short miktoarm ends are yellow, and all type B beads are blue.

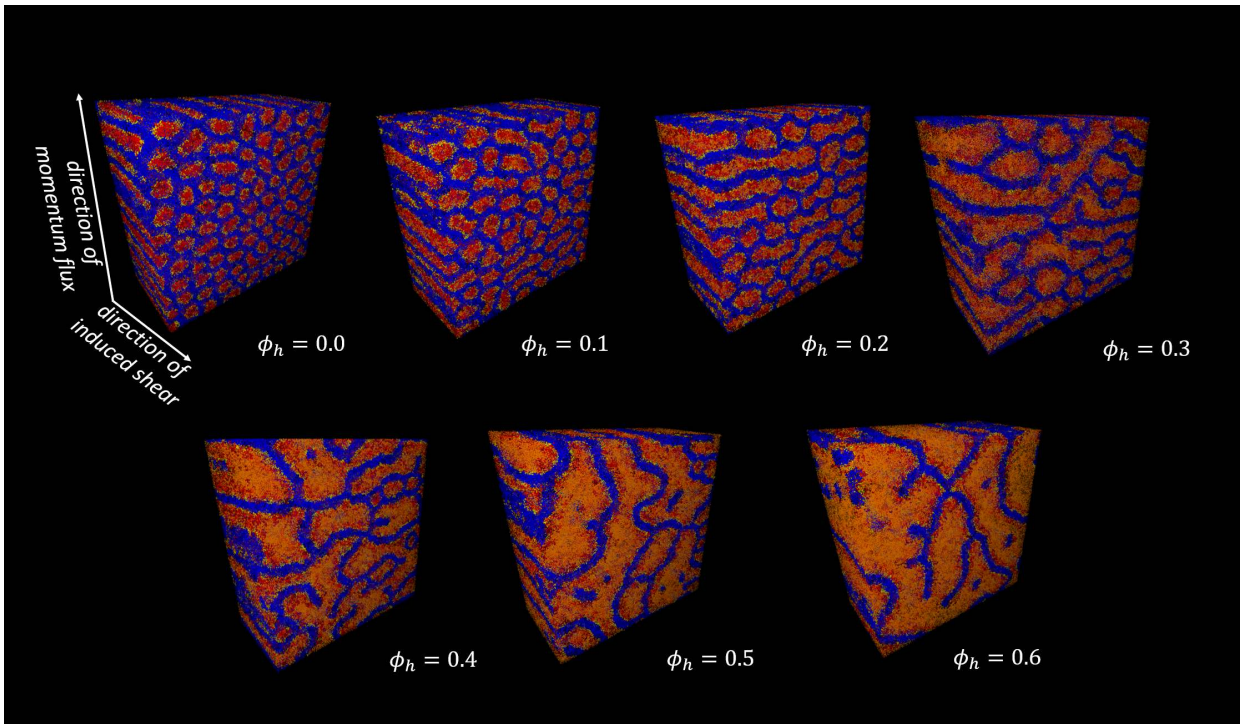

Figure 4.12: The phases resulting from long application of shear to all tested blend compositions, as a function of the number density of homopolymer beads, ϕ_h. The images are sliced along a plane perpendicular to the shear direction. Bead identities are distinguishable by color - homopolymer beads are orange, long miktoarm tail beads are red, short miktoarm ends are yellow, and all type B beads are blue.

Just as was done for nonequilibrium shear, to begin understanding the equilibrium dynamic properties of the B&M phase, we consider it important to establish the equilibrium behavior of the blends when phase separation has not occurred. In Figure 4.13 and in Figure 4.14, we present the relaxation modulus $G(t)$ over several decades of time, as well as the storage and loss moduli, $G'(\omega)$ and $G''(\omega)$, obtained from Fourier transforms of $G(t)$, over several decades of frequency.

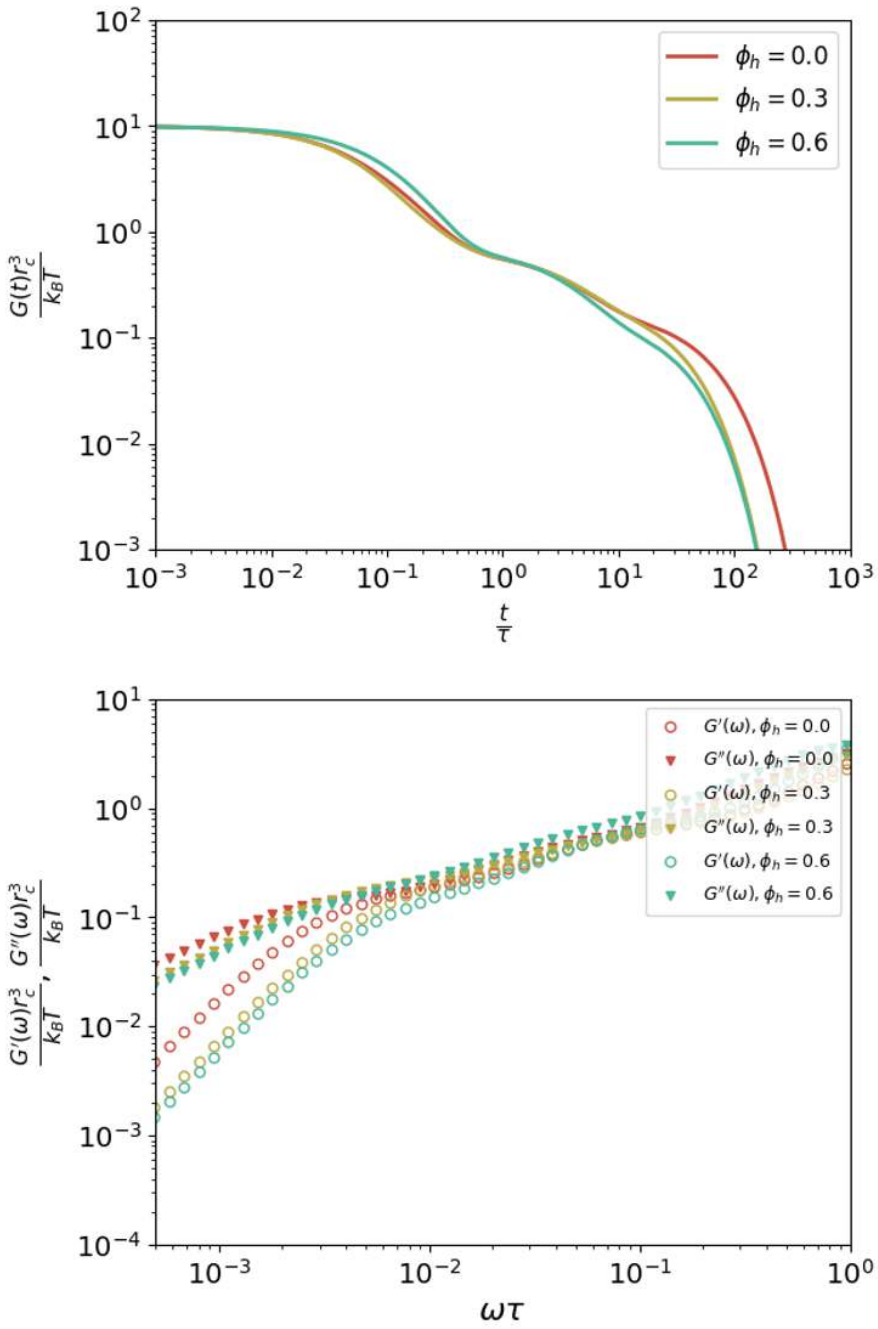

Figure 4.13: Upper, the relaxation moduli $G(t)$ for selected blend composition (we present here the final, fitted curves; see below for full details). Lower, the storage ($G'(\omega)$) and loss ($G''(\omega)$) moduli obtained for each blend composition. Both plots are for the labeled blend composition at an effective $\chi N = 0$.

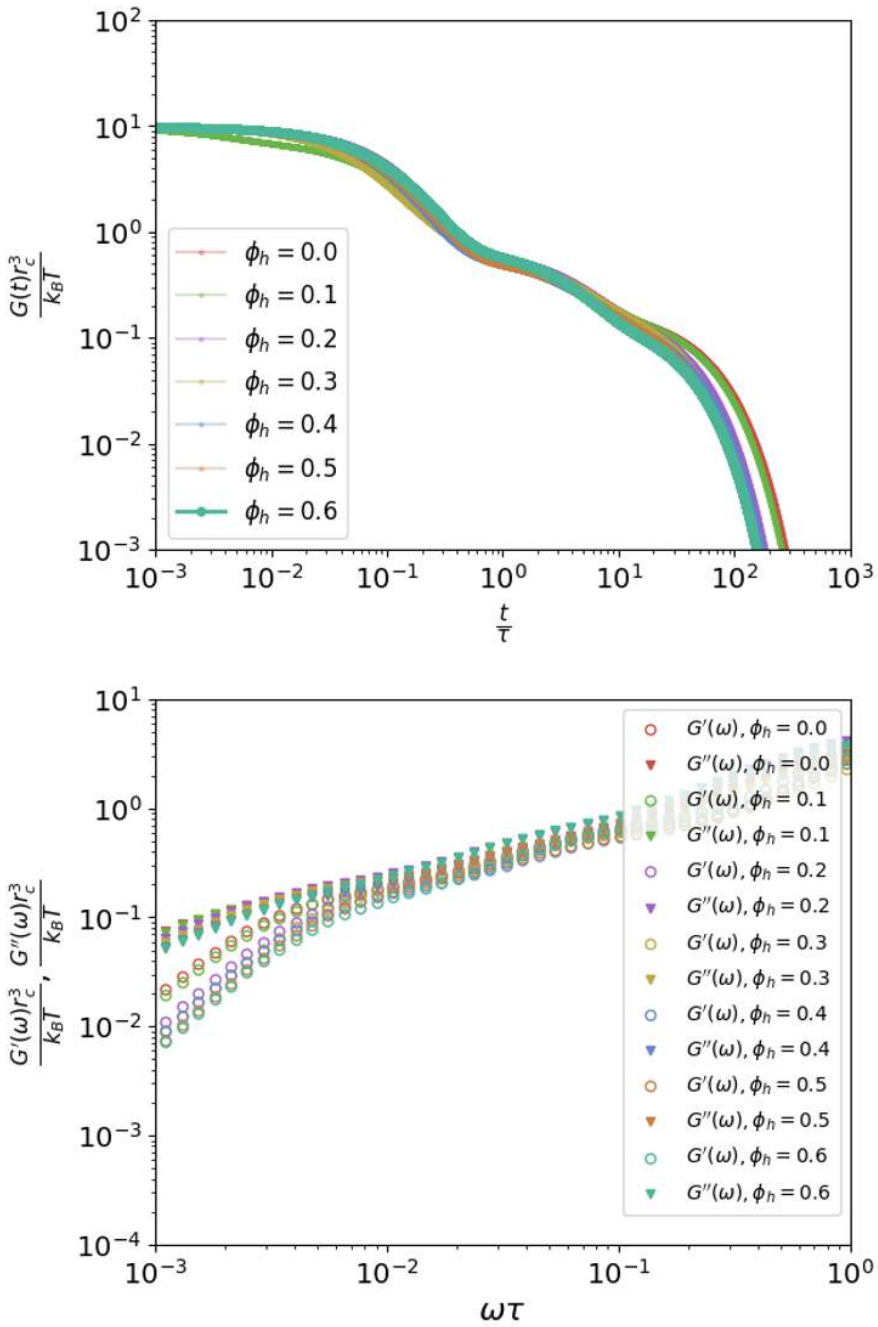

Figure 4.14: Upper, the relaxation moduli $G(t)$ for each blend composition (we present here the final, fitted curves; see below for full details). Lower, the storage ($G'(\omega)$) and loss ($G''(\omega)$) moduli obtained for each blend composition. Both plots are for the labeled blend composition at an effective $\chi N = 0$.

From $G(t)$ the viscosity can be obtained simply as the area under the curve. We have already discussed above that there is a clear decrease in the viscosity associated with an

increasing proportion of shorter chains in the blend. For the same reasons, there is a noticeable trend of decreasing $G'(\omega)$ at low ω as ϕ_h increases. We also note that, generally, each polymer blend shows the characteristic behavior of Rouse polymers; $G'(\omega)$ increases with ω with a slope of ≈ 2 at low frequency, while $G''(\omega)$ does so with a slope of ≈ 1; they approach each other in value and both begin to increase with a slope of $\approx \frac{1}{2}$ at intermediate ω. There are essentially three timescales of relaxation - of order 0.1τ, 10τ, and 100τ. We associate the smallest relaxation time scale with the relaxation of individual harmonic bonds. From independent simulations, we can fit a single exponential to the decay of the end-to-end distance autocorrelation function for either the individual arms of the miktoarm star or for the longest linear distance in the miktoarm (i.e. $N = 35$) (the longest single-molecule relaxation time we should observe). We find the average relaxation time of the individual arms of the stars is 32.5τ and the average relaxation time of the longest linear distance in the miktoarm is 130τ. We therefore associate the former with the intermediate relaxation mode of order 10τ and the latter with the longest relaxation mode of order 100τ. We also note the possibility that multiple relaxation modes of similar timescales are compressed into a single mode in the $G(t)$ fit.

Next we consider the equilibrium (linear) dynamic properties of the assembled mesophases. Just as above, in Figure 4.15 and in Figure 4.16, we present $G(t)$, $G'(\omega)$, and $G''(\omega)$.

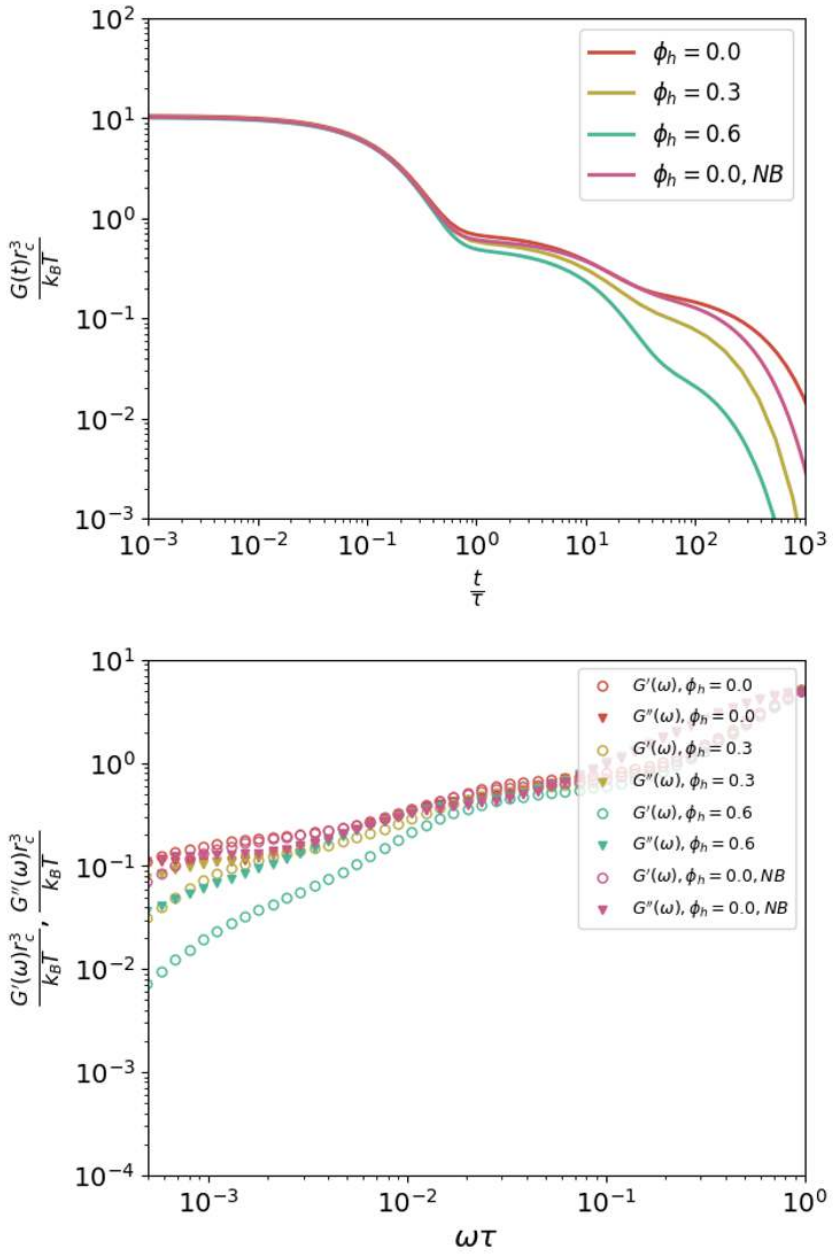

Figure 4.15: Upper, the relaxation moduli $G(t)$ for selected blend composition (we present here the final, fitted curves; see below for full details). Lower, the storage ($G'(\omega)$) and loss ($G''(\omega)$) moduli obtained for each blend composition; we note the slight expansion of the frequency axis to include lower frequencies, as the modes below $\omega = 10^{-3}\tau$ are important to the mesophases. Both plots are for the labeled blend composition at an effective $\chi N \approx 160$.

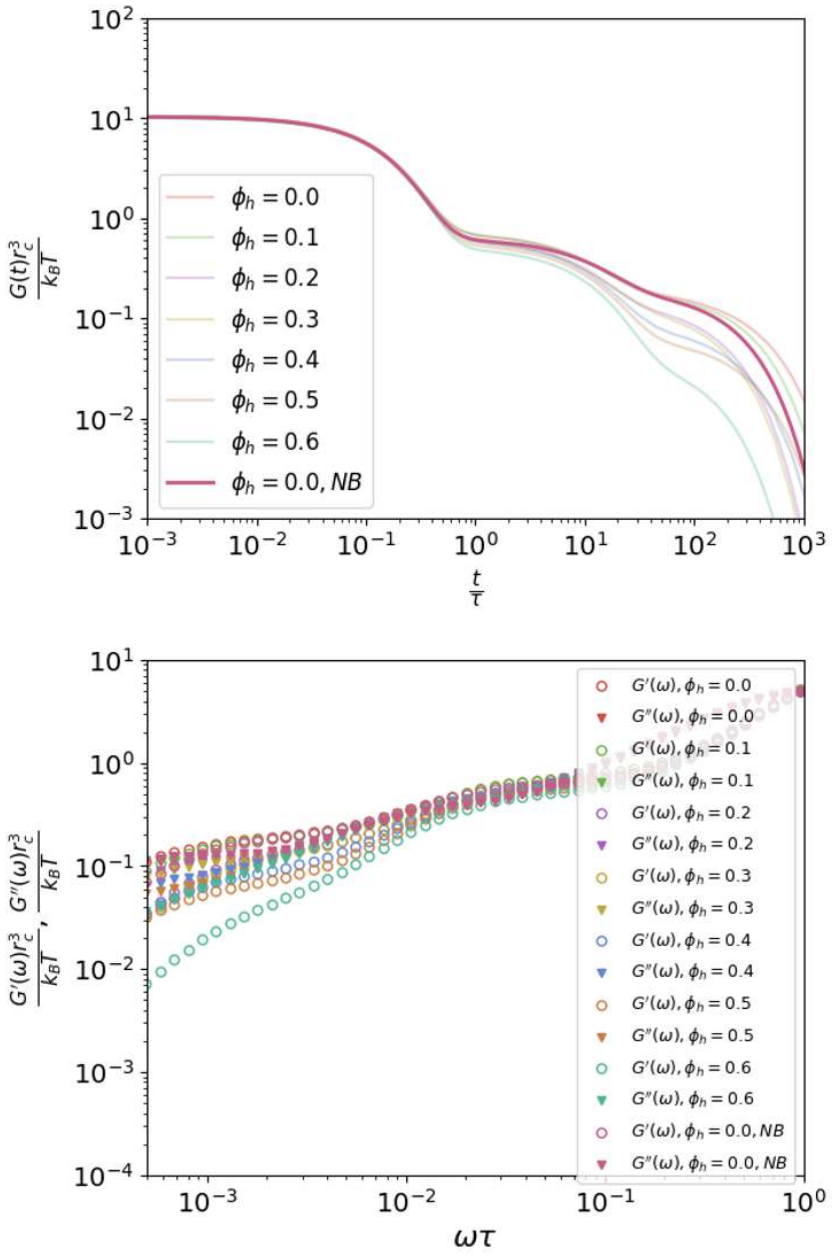

Figure 4.16: Upper, the relaxation moduli $G(t)$ for each blend composition (we present here the final, fitted curves; see below for full details). Lower, the storage ($G'(\omega)$) and loss ($G''(\omega)$) moduli obtained for each blend composition; we note the slight expansion of the frequency axis to include lower frequencies, as the modes below $\omega = 10^{-3}\tau$ are important to the mesophases. Both plots are for the labeled blend composition at an effective $\chi N \approx 160$.

The results included in Figure 4.13, Figure 4.15, Figure 4.14, Figure 4.16, and Table 4.1 can be compared together for an understanding of the dynamic behavior of the B&M phase.

As the results obtained via equilibrium simulation faithfully represent the properties of the B&M phase in a way the results obtained via nonequilibrium shear do not, the trend across these data points to a clear picture of the overall behavior. Compared to the disordered blends, the ordered phases (at $\phi_h = 0.0$ and $\phi_h = 0.1$ (see SI), a cylindrical phase, and at other conditions, the B&M phase) exhibit significantly higher viscosity, significantly longer relaxation times (the relaxation time being inferred from the time required for $G(t)$ to decay to zero), and significantly higher $G'(\omega)$ at low frequencies (a direct measure of the solid-like behavior or elasticity of the system). We note that this trend continues even to the highest blend concentration we study, though the effect of an increasing proportion of homopolymer and a lower absolute proportion of bridging chains is observable as the effect does weaken at high ϕ_h. As noted above, some of this effect could be attributed simply to the formation of a microphase separated phase even in the absence of molecular bridging, and therefore we also study the properties of the 'NB' system. That the longest relaxation time and low frequency G' are much lower than the comparable neat blend of miktoarms which are capable of bridging is clear from Figure 4.15; we also calculate the viscosity of the phase to be 53.4 (simulation units), comparable to a B&M phase with as much as 10-20% homopolymer in the blend. This last point underscores an important general point - that the B&M phases with significant amounts of homopolymer perform similarly to a mesophase composed solely of miktoarms which cannot bridges is clear evidence of the significant role that bridging plays on the dynamic properties of the B&M even at the highest homopolymer concentrations.

As a last perspective on the mechanical properties, we perform stress-strain simulations (see below for details) to understand the linear response of the B&M phase to strain. The curves are presented in Figure 4.17 and Figure 4.19. Additionally, representative images of the systems as they are being strained are presented in Figure 4.18.

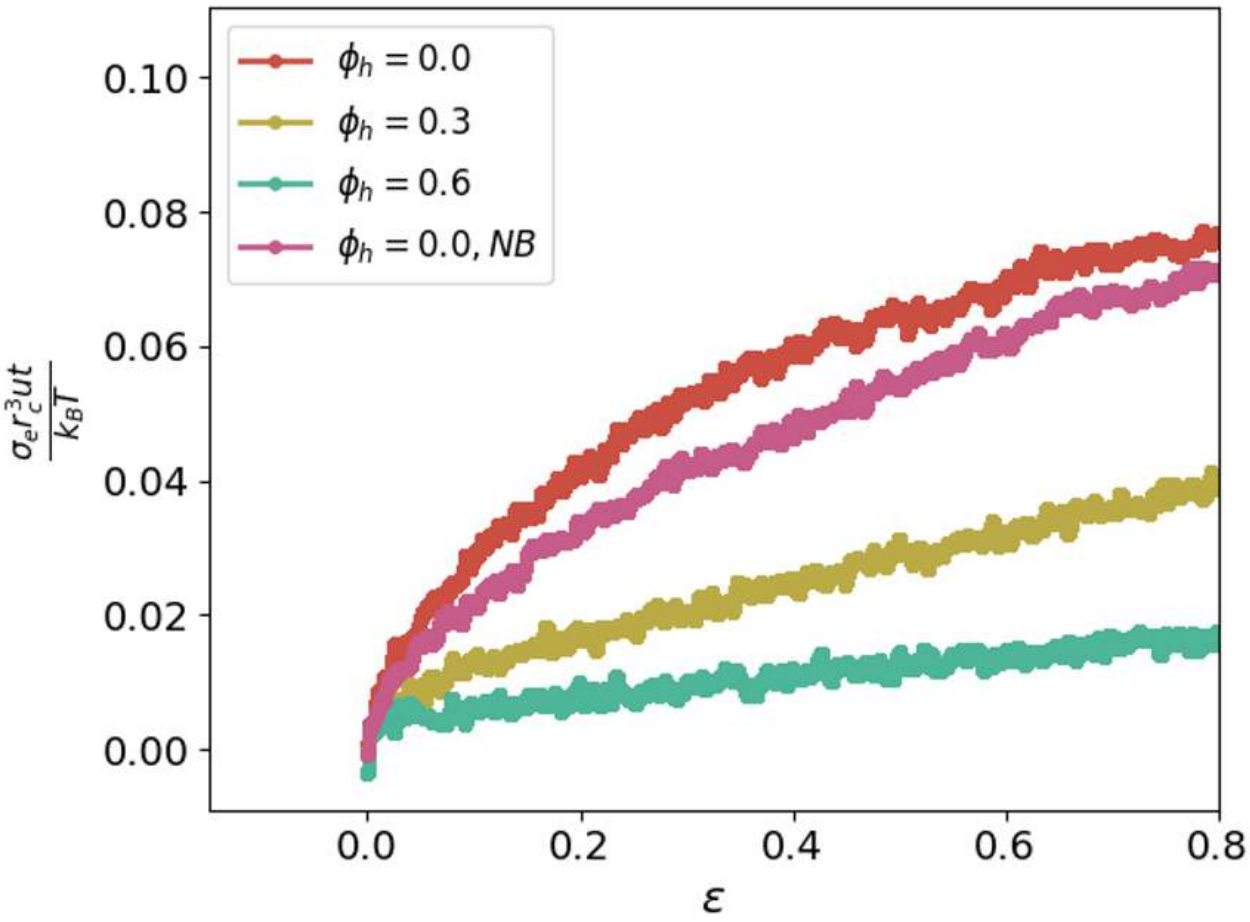

Figure 4.17: Stress strain curves up to a true strain of $\epsilon = 0.8$ for select blend compositions.

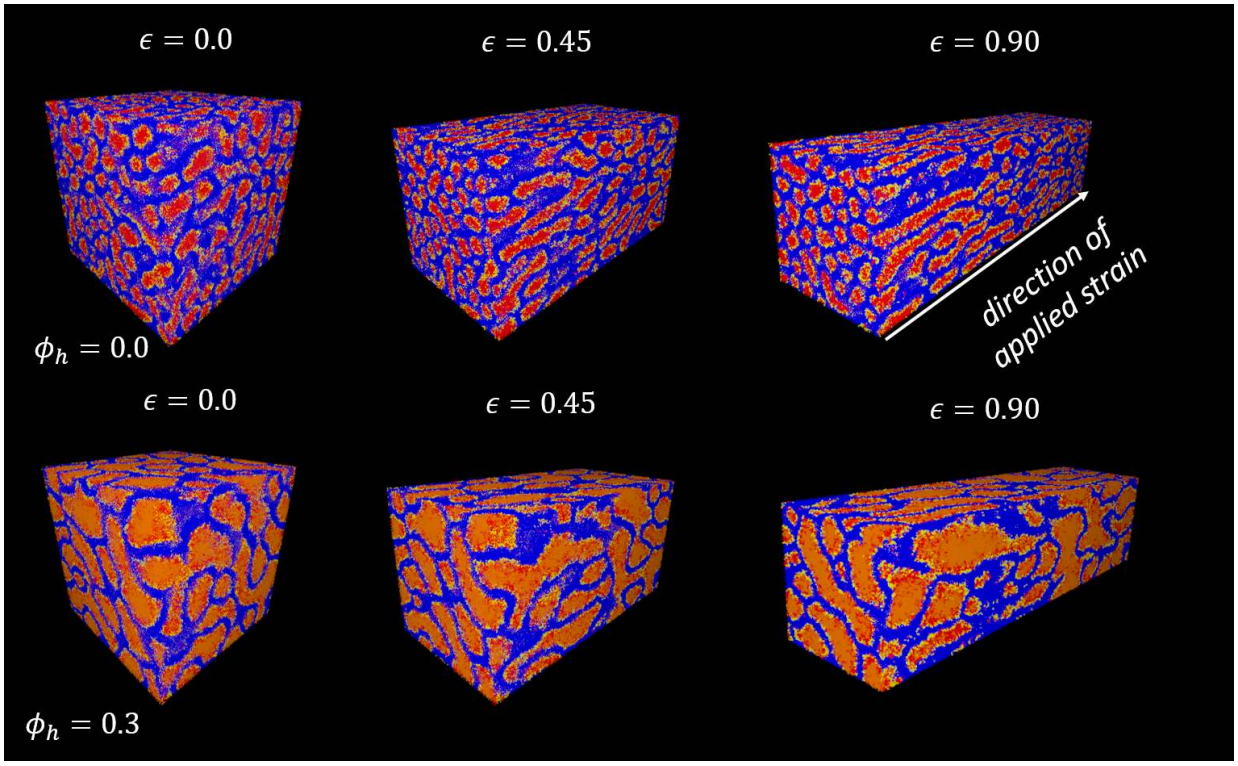

Figure 4.18: Visual representations of the phases having undergone strain up to $\epsilon = 0.90$. In both cases, the strain has not fundamentally altered the nature of the phase, merely deformed it.

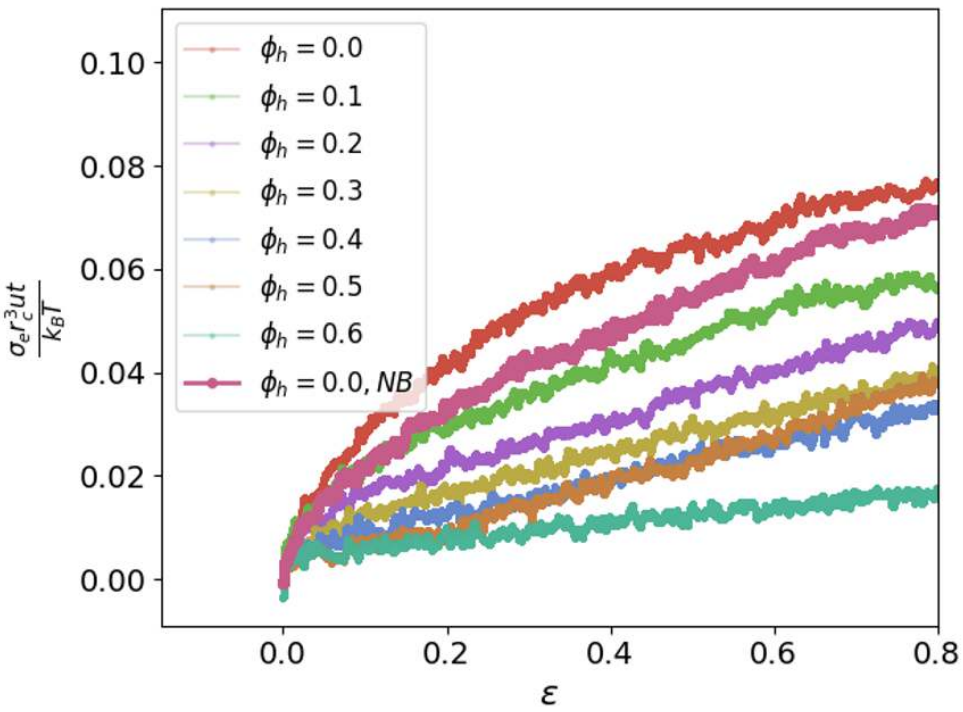

Figure 4.19: Stress strain curves up to a true strain of $\epsilon = 0.8$ for all tested blend compositions.

We first note that all the curves have the essential qualitative behavior of a classic unentangled rubber[105], with a two-slope behavior in the linear regime (a higher slope at low ϵ and a lower slope at larger ϵ). Furthermore, it is evident that the Young's modulus (the slope in the linear regime) consistently decreases with increasing ϕ_h. This agrees well with the data presented so far - that the increasing proportion of homopolymer in the blends and the decreasing absolute number of bridges decreases viscosity and the storage modulus, for example. On the other hand, the $0.0, NB$ case - which cannot bridge - has comparable Young's modulus to the 0.0 case which bridges significantly. We therefore consider that the molecular weight of the constituent polymers is also a significant factor in setting properties of the materials, especially, evidently, the Young's modulus. For example, the 0.6 case bridges but is composed of a majority of much lower molecular weight homopolymers as compared to the higher molecular weight miktoarms. The $0.0, NB$ case is entirely composed of miktoarms and has a higher Young's modulus, pointing toward the important role of molecular weight.

We suggest, however, that in such systems the elastic recovery would be significantly lower for the $0.0, NB$ case due to its lack of bridging. Our results also underscore an important limitation of the model used here. The experimental results of Shi et al.[115] shows exactly the opposite trend of what we present here - that an increasing proportion of homopolymer increases the Young's modulus (without a concomitant sacrifice in elasticity). The difference is easily understood by the fact that the experimental system is one in which polymer type A is polystyrene (a glassy polymer at the temperatures of interest) and polymer type B is polyisoprene (a rubbery polymer at the temperatures of interest). Hence, an increasing proportion of a strong, glassy reinforcing material like polystyrene has a significant role in increasing the Young's modulus of the material which overwhelms the decreasing absolute number of bridges and the lower molecular weight of the homopolymer. This effect cannot be captured by the DPD model, in which the friction coefficient (which would determine whether the polymers behave like rubbers or like glasses) is equal for both type A and type B polymer and is of necessity quite low[37]; our polymers will therefore all behave generally like rubbers. While computer simulations including the effect of glassiness in the type A domains are of great interest[4, 39], we note two important advantages of the current approach. Firstly, an approach such as ours based on pure DPD allows for faster simulation equilibration, providing access to the information contained herein on a meaningfully shorter time scale than a study conducted with a model accounting for glassiness. Secondly, through this work, we can isolate the purely morphological effects of the microstructure (e.g., bridging) on the dynamical properties of the phase, whereas including glassiness in the model would obscure all of the effects we have described herein. Hence, we consider it an interesting first step in understanding the behavior of these polymers to approach the problem with the present model, and note our future work will address the role of glassiness in the type A domains for comparison.

4.4 Conclusions

Using dissipative particle dynamics, the dynamic properties of the bricks-and-mortar phase, recently unveiled with experimental[115] and theoretical/simulation [75] studies, have been explored. We have first established that the B&M phase emerges in three-dimensional particle based simulations, expanding upon prior results which predicted it in two-dimensional field theoretic simulations. That the B&M phase observed in our simulations is aperiodic is confirmed via the calculation of structure factors, which show no peak indicating a regular domain spacing. The structure factors for all assembled phases, however, do show a common length scale associated with the thickness of the B domains. We calculate relative bridging fractions for each homopolymer concentration and find that all B&M phases display significant amounts of molecular bridging between domains. The influence of this bridging is clearly seen over the dynamic properties, including significant enhancement in viscosity and low frequency $G'(\omega)$ (a measure of elasticity) in the mesophases compared to disordered blends. In particular, we highlight that an ordered phase of non-bridging miktoarms with no homopolymer in the blend behaves similarly to a B&M phase with as much as 10-20% homopolymer in the blend, highlighting that even the decreasing relative proportions of bridges in these phases dominate the mechanical behavior. The calculation of stress-strain curves yields results consistent with these trends, but comparison to experiment highlights an important aspect of the chosen model - that the DPD method as implemented herein will not account for relative glassiness or rubberiness of the chains. Nonetheless, precisely because of these limitations, we are able to isolate the purely morphological influence on the dynamic properties, and demonstrate that molecular bridging dominates up to the highest ϕ_h values we study. Finally, we also note that the B&M phase is evidently destroyed by shear, which may have important ramifications for the processibility of such mesophases.

4.5 Methods

To efficiently simulate the very large systems required to capture the bricks-and-mortar domains, we turn to coarse grained dissipative particle dynamics [42, 56]. The dissipative particle dynamics (DPD) potential is composed a (purely repulsive) interaction potential, a pairwise drag force, and a pairwise random force. The force, F, on each coarse-grained bead is calculated as

$$F = F_C(r) + F_{R,ij}(r_{ij}) + F_{D,ij}(v_{ij}) \tag{4.1}$$

. r_{ij} is the inter-particle distance and v_{ij} is the inter-particle velocity. The conservative force, F_C, accounts for inter-particle interactions and is calculated as

$$F_C(r) = A_{ij} \cdot w(r_{ij}) \tag{4.2}$$

, with

$$w(r_{ij}) = \left(1 - \frac{r}{r_{cut}}\right) r < r_{cut}$$
$$0 \; r \geq r_{cut}$$

. A_{ij} scales the strength of the interaction and be tailored for each pair type. In our work, $A_{AA} = A_{BB} = 25 \; k_BT$ following Groot et al. [35, 36] We also follow Groot et al. and choose the system density $\rho = 3$; our choice of $A_{AB} = 40 \; k_BT$ therefore corresponds to a choice of $\chi_{AB}N \approx 160$, putting our results firmly in the strong segregation limit. As is typical in DPD simulations, we choose $r_{cut} = k_BT = m = 1$, where m is the particle mass (the unit of time, therefore, is $\tau = r_{cut}\sqrt{\frac{m}{k_BT}}$). The random and drag forces, $F_{R,ij}(r_{ij})$ and $F_{D,ij}(v_{ij})$, respectively, are calculated as

$$F_{R,ij}(r_{ij}) = -\theta_{ij}\sqrt{3}\sqrt{\frac{2k_B\gamma T}{\Delta t}} \cdot w(r_{ij}) \tag{4.3}$$

$$F_{D,ij}(v_{ij}) = -\gamma w^2(r_{ij}) \left(\hat{r}_{ij} \circ v_{ij}\right) \tag{4.4}$$

. θ_{ij} is a uniformly distributed random number in the range $[-1, 1]$, γ is a friction parameter for which we use a typical value of 4.5, and Δt is the simulation time-step, for which we typically use a value of 0.04 unless otherwise noted; $\hat{r}_{ij}$ is the inter-particle distance normalized to magnitude unity. Bonded beads are connected by a harmonic potential $V(r) = \frac{1}{2}k\,(r)^2$, with the spring constant $k = 4$. We perform all simulations using the HOOMD-blue software package [3, 32, 100]; visualizations are performed using Visual Molecular Dynamics (VMD) [43].

We choose the number of beads N of each block of the $A(BA')_3$ miktoarm polymer with $N_A = 20$, $N_B = 12$, and $N_{A'} = 3$, in approximate accordance with the experimental proportions [115, 75]. For blends, the appropriate proportion of $N = 16$ homopolymers of bead type A are inserted into the blend. To compare to field-theoretic approaches [75], it is also useful to note that, from the above parameters, the term $\sqrt{\bar{N}} = \frac{\rho R_e^3}{N} \approx 4$; $\sqrt{\bar{N}}$ is, roughly speaking, a Ginzburg parameter (the mean field limit applies as $\sqrt{\bar{N}} \to \infty$ [27]); therefore, our simulations are performed in a limit far from the mean-field condition and are able to capture thermal fluctuations well.

A summary of all of the parameter choices made for our DPD model is provided in Table 4.2.

1. Groot and Madden[35] discuss the correspondence of χN_{eff} from DPD simulation with finite-length chains to the mean field χN corresponding to infinite molecular weight. Their calculation shows that $\chi N_{eff} \approx \frac{\chi N}{1+3.9N^{-0.5}}$. As a point of reference, therefore, the mean-field result that $\chi N_c = 10.5$ for symmetric linear diblocks should be reproduced in the model used herein for, say, $N = 35$ (the longest end-to-end length in a miktoarm) at a value of $\chi N = 17.2$. That our choice of χN exceeds χN_c by an order of magnitude is solely to establish our calculations well into the strong segregation limit such that any phase behavior is well defined; we find that at χN of similar magnitude to χN_c, the phase boundaries can be ill defined for the fluctuation-stabilized bricks and mortar phase. The dynamics are not unduly inhibited as the viscosity

Parameter	Symbol	Numerical Value	Notes
Density	ρ	3	Standard [35, 36]
Type A-Type A self-interaction	A_{AA}	25	Standard [35, 36]
Type B-Type B self-interaction	A_{BB}	25	Standard [35, 36]
Type A-Type B cross-interaction	A_{AB}	40	$\chi N \approx 160$ [35]; see note [1]
Friction parameter	γ	4.5	HOOMD default

Table 4.2: DPD model parameter choices, with notes if necessary. Note that $r_{cut} = k_B T = m = 1$ and the DPD unit of time is $\tau = r_{cut}\sqrt{\frac{m}{k_B T}}$

To help quantify the nature of assembled structures, we calculate the structure factor, $S(\boldsymbol{q})$, using the following equation[109]:

$$S(\boldsymbol{q}) = \frac{\left(\sum_j \cos\left(\boldsymbol{q}\cdot\boldsymbol{r}_j\right)\right)^2 + \left(\sum_j \sin\left(\boldsymbol{q}\cdot\boldsymbol{r}_j\right)\right)^2}{N} \tag{4.5}$$

The index j runs over all type A particles in the system; $\boldsymbol{q}$ is the wave vector (for each magnitude of $\boldsymbol{q}$ we sample 100 randomly generated possible realizations of $\boldsymbol{q}$ and compute the average value of $S(\boldsymbol{q})$); $\boldsymbol{r}_j$ are the particles positions; lastly, N is the total number of particles.

In addition to static structure factors, we calculate the dynamic structure factor (the van Hove function), using the following equation:

$$S(\boldsymbol{q}, t) = \frac{\langle \psi(\boldsymbol{q}, t)\psi^*(\boldsymbol{q}, 0)\rangle}{V} \tag{4.6}$$

As before, $\boldsymbol{q}$ is the wave vector; t is time, and V is the system volume. The function $\psi(\boldsymbol{q}, t)$ is given as:

$$\psi(\boldsymbol{q}, t) = \sum_i c_\alpha \exp(i\boldsymbol{q}\cdot\boldsymbol{r}_j) \tag{4.7}$$

As before, the index j runs over all particles in the system. In our prior calculation of

of a DPD fluid absent of phase separation (and therefore, the primary relaxation time of the chains) is determined by γ rather than A [37].

the static structure factor, we only considered type A beads. Here, we let the coefficient c_α equal 1 for type A beads and -1 for type B beads. We implement this calculation using the Simpatico software package [1].

We also quantify the distribution of conformations of miktoarm chains following the method of Tang et al. [126] In brief, we consider that each junction on the miktoarm polymers should be relatively localized to the interface; we identify the positions of the four A beads associated with these junctions as $\boldsymbol{R}_k$, $k = 1, 2, 3, 4$. By defining a cutoff radius $R_c = 1.25$ (in simulation units), we can identify the center of mass of B-beads in the vicinity of the junction. Then a unit normal $\boldsymbol{n}_k$ of the interface can be calculated. We identify $\boldsymbol{n}_1$ as the unit normal associated with the long A tail and the center junction, whereas $\boldsymbol{n}_2$, $\boldsymbol{n}_3$, and $\boldsymbol{n}_4$ are associated with the short A ends terminating the $B - A'$ arms. It is possible for each arm of the star to independently bridge or loop, and so we calculate the dot product between $\boldsymbol{n}_1$ and each of $\boldsymbol{n}_2$, $\boldsymbol{n}_3$, and $\boldsymbol{n}_4$. This quantity, ζ_{ij} essentially measures whether the interfacial normals are parallel ($\zeta_{ij} > 0$) or anti-parallel ($\zeta_{ij} < 0$). If they are anti-parallel, this is indicative that the arm is forming a bridge. A bridging fraction can then be computed in two ways; the total fraction of arms which are bridging is ν_b, whereas the total number of chains with at least one arm bridging is $\nu_{b,chains}$. The latter is the quantity most frequently cited as the "bridging fraction" for multi-arm copolymers. We refer to Tang et al. for full details of the calculation and justification of the methodology.

We calculate a variety of viscoelastic properties using equilibrium and non-equilibrium simulations. From equilibrium sampling of the stress tensor, information about the storage and loss moduli, $G'(\omega)$ and $G''(\omega)$ can be obtained. The auto-correlation function of the off-diagonal components of the stress tensor (σ) is, according to a Green-Kubo relation, equivalent to the relaxation modulus $G(t)$:

$$G(t) = \frac{V}{k_B T} \langle \sigma_{\alpha,\beta}(t) \sigma_{\alpha,\beta}(0) \rangle \tag{4.8}$$

with $\alpha \neq \beta$ (V is the system volume). We find it necessary to reduce the time-step Δt to 0.004 (an order of magnitude reduction) to obtain fine enough sampling to accurately resolve $G(t)$; we further find that approximately 10^7 time-steps are necessary to suppress noise sufficiently. We fit the auto-correlation function to a sum of exponentially decaying terms (the generalized Maxwell model) [70, 48]:

$$G(t) = \sum_n G_n \exp\left(-\frac{t}{t_n}\right) \tag{4.9}$$

where G_n and t_n represent the amplitude and the relaxation time of the nth mode, respectively. The Fourier transform of $G(t)$ into the frequency domain yields the dynamic modulus $G^*(\omega)$, and the real and imaginary component of $G^*(\omega)$ are $G'(\omega)$ and $G''(\omega)$, respectively.

We apply shear using the HOOMD-blue implementation of the Müller-Plathe method [91]. A flow is induced in the following way: the system is divided into a number (100) of slabs and a desired flow magnitude and direction is chosen. The "bottom" slab is searched for the particle with the largest magnitude velocity component opposite the desired flow direction; the "middle" slab is searched for the particle with the largest magnitude velocity component in the desired flow direction. These velocity components are then swapped, inducing a flux of momentum (up to a desired target). The flux of momentum induces a shear flow; we target a shear rate of approximately 0.005 τ^{-1} for all blends to account for possible shear thinning effects. As the momentum flux is known exactly, the velocity gradient need only be measured (provided the velocity profile is linear) to determine the viscosity.

Lastly, we apply uniaxial tension by affinely deforming the box length L in the z-direction (at constant volume) according to[119] $L_z(t) = L_{0,z}e^{\dot{\epsilon}dt}$, where dt represents the total elapsed time up to time t. We choose a true strain rate $\dot{\epsilon} = 10^{-4}$ following Sirk et al. (we note the relaxation time of the longest linear part of the star is $\mathcal{O}(100\tau)$ and the morphological relaxation time is $\mathcal{O}(1000\tau)$, ergo the entirety of the curve in Figure 4.17 takes place in

about a single morphological relaxation time. The nonzero stress response is a consequence of the strain being too fast for the system to easily equilibrate.) The elongation stress σ_e is calculated from the stress tensor as

$$\sigma_e = -\sigma_{zz} + \frac{1}{2}\left(\sigma_{xx} + \sigma_{yy}\right) \tag{4.10}$$

.

REFERENCES

[1] Simpatico simulation package source code repository, located at https://github.com/dmorse/simpatico.

[2] James Ahrens, Berk Geveci, and Charles Law. ParaView: An End-User Tool for Large-Data Visualization. In *Visualization Handbook*, volume 836, pages 717–731. Elsevier, 2005.

[3] Joshua A. Anderson, Chris D. Lorenz, and A. Travesset. General purpose molecular dynamics simulations fully implemented on graphics processing units. *Journal of Computational Physics*, 227(10):5342–5359, may 2008.

[4] Takeshi Aoyagi, Takashi Honda, and Masao Doi. Microstructural study of mechanical properties of the ABA triblock copolymer using self-consistent field and molecular dynamics. *The Journal of Chemical Physics*, 117(17):8153–8161, nov 2002.

[5] Christopher M. Bates and Frank S. Bates. 50th Anniversary Perspective : Block Polymers—Pure Potential. *Macromolecules*, 50(1):3–22, jan 2017.

[6] Christopher M. Bates, Michael J. Maher, Dustin W. Janes, Christopher J. Ellison, and C. Grant Willson. Block Copolymer Lithography. *Macromolecules*, 47(1):2–12, jan 2014.

[7] F. S. Bates, Marc a. Hillmyer, Timothy P. Lodge, Christopher M. Bates, Kris T. Delaney, and Glenn H. Fredrickson. Multiblock Polymers: Panacea or Pandora's Box? *Science*, 336(6080):434–440, apr 2012.

[8] Frank S. Bates, Wayne W. Maurer, Paul M. Lipic, Marc A. Hillmyer, Kristoffer Almdal, Kell Mortensen, Glenn H. Fredrickson, and Timothy P. Lodge. Polymeric Bicontinuous Microemulsions. *Physical Review Letters*, 79(5):849–852, aug 1997.

[9] Cody T. Bezik and Juan J. De Pablo. Formation, Stability, and Annihilation of the Stitched Morphology in Block Copolymer Thin Films. *Macromolecules*, 53(23):10446–10456, oct 2020.

[10] Cody T. Bezik, Grant P. Garner, and Juan J. de Pablo. Mechanisms of Directed Self-Assembly in Cylindrical Hole Confinements. *Macromolecules*, 51(7):2418–2427, apr 2018.

[11] Cody T Bezik, Joshua A Mysona, Ludwig Schneider, Marcus Müller, and Juan J De Pablo. Dynamic Simulations of the " Bricks-and-Mortar " Mesophase in Blends of Miktoarm Block Copolymers and Homopolymers.

[12] Joy K. Cheng, Charles T. Rettner, Daniel P. Sanders, Ho Cheol Kim, and William D. Hinsberg. Dense self-assembly on sparse chemical patterns: Rectifying and multiplying lithographic patterns using block copolymers. *Advanced Materials*, 20(16):3155–3158, 2008.

[13] Joy Y. Cheng, Anne M. Mayes, and Caroline A. Ross. Nanostructure engineering by templated self-assembly of block copolymers. *Nature Materials*, 3(11):823–828, nov 2004.

[14] Joy Y. Cheng, Daniel P. Sanders, Hoa D. Truong, Stefan Harrer, Alexander Friz, Steven Holmes, Matthew Colburn, and William D. Hinsberg. Simple and versatile methods to integrate directed self-assembly with optical lithography using a polarity-switched photoresist. *ACS Nano*, 4(8):4815–4823, 2010.

[15] Xiuyuan Cheng, Ling Lin, Weinan E, Pingwen Zhang, and An-Chang Shi. Nucleation of Ordered Phases in Block Copolymers. *Physical Review Letters*, 104(14):148301, apr 2010.

[16] S.B. Darling. Directing the self-assembly of block copolymers. *Progress in Polymer Science*, 32(10):1152–1204, oct 2007.

[17] François a. Detcheverry, Huiman Kang, Kostas Ch Daoulas, Marcus Müller, Paul F Nealey, and Juan J. de Pablo. Monte Carlo Simulations of a Coarse Grain Model for Block Copolymers and Nanocomposites. *Macromolecules*, 41(13):4989–5001, jul 2008.

[18] François a. Detcheverry, Guoliang Liu, Paul F. Nealey, and Juan J. de Pablo. Interpolation in the Directed Assembly of Block Copolymers on Nanopatterned Substrates: Simulation and Experiments. *Macromolecules*, 43(7):3446–3454, apr 2010.

[19] Francois A. Detcheverry, Darin Q. Pike, Paul F. Nealey, Marcus Muller, and Juan J. de Pablo. Monte Carlo Simulation of Coarse Grain Polymeric Systems. *Physical Review Letters*, 102(19):197801, may 2009.

[20] Jan Doise, Joost Bekaert, Boon Teik Chan, Roel Gronheid, Yi Cao, SungEun Hong, Guanyang Lin, Daniel Fishman, Yuli Chakk, and Taisir Marzook. Implementation of surface energy modification in graphoepitaxy directed self-assembly for hole multiplication. *Journal of Vacuum Science & Technology B, Nanotechnology and Microelectronics: Materials, Processing, Measurement, and Phenomena*, 33(6):06F301, nov 2015.

[21] Dominik Düchs, Venkat Ganesan, Glenn H. Fredrickson, and Friederike Schmid. Fluctuation Effects in Ternary AB + A + B Polymeric Emulsions. *Macromolecules*, 36(24):9237–9248, dec 2003.

[22] Weinan E, Weiqing Ren, and Eric Vanden-Eijnden. String method for the study of rare events. *Physical Review B*, 66(5):052301, aug 2002.

[23] Weinan E, Weiqing Ren, and Eric Vanden-Eijnden. Finite Temperature String Method for the Study of Rare Events. *The Journal of Physical Chemistry B*, 109(14):6688–6693, apr 2005.

[24] Weinan E, Weiqing Ren, and Eric Vanden-Eijnden. Simplified and improved string method for computing the minimum energy paths in barrier-crossing events. *The Journal of Chemical Physics*, 126(16):164103, apr 2007.

[25] G H Fredrickson and F S Bates. Dynamics of Block Copolymers: Theory and Experiment. *Annual Review of Materials Science*, 26(1):501–550, aug 1996.

[26] G.H. H Fredrickson and F.S. S Bates. Stabilizing co-continuous polymer blend morphologies with ABC block copolymers. *EUROPEAN PHYSICAL JOURNAL B*, 1(1):71–76, jan 1998.

[27] Glenn Fredrickson. *The Equilibrium Theory of Inhomogeneous Polymers*. Oxford University Press, dec 2005.

[28] Glenn H. Fredrickson and Frank S. Bates. Design of bicontinuous polymeric microemulsions. *Journal of Polymer Science Part B: Polymer Physics*, 35(17):2775–2786, dec 1997.

[29] Grant P Garner. *Coarse Grained Modeling of Block Copolymer Lithography: the Effects of Pattern Design on the Thermodynamics and Kinetics of the Directed Self Assembly of Block Copolymers*. PhD thesis, 2017.

[30] T. Geisinger, M. Müller, and K. Binder. Symmetric diblock copolymers in thin films. I. Phase stability in self-consistent field calculations and Monte Carlo simulations. *Journal of Chemical Physics*, 111(11):5241–5250, 1999.

[31] Samuel P. Gido, Janelle Gunther, Edwin L. Thomas, and David Hoffman. Lamellar diblock copolymer grain boundary morphology. 1. Twist boundary characterization. *Macromolecules*, 26(17):4506–4520, aug 1993.

[32] Jens Glaser, Trung Dac Nguyen, Joshua A. Anderson, Pak Lui, Filippo Spiga, Jaime A. Millan, David C. Morse, and Sharon C. Glotzer. Strong scaling of general-purpose molecular dynamics simulations on GPUs. *Computer Physics Communications*, 192:97–107, jul 2015.

[33] Gregory M. Grason and Randall D. Kamien. Interfaces in Diblocks: A Study of Miktoarm Star Copolymers. *Macromolecules*, 37(19):7371–7380, apr 2004.

[34] Roel Gronheid, Jan Doise, Joost Bekaert, Boon Teik Chan, Ioannis Karageorgos, Julien Ryckaert, Geert Vandenberghe, Yi Cao, Guanyang Lin, Mark Somervell, Germain Fenger, and Daisuke Fuchimoto. Implementation of templated DSA for via layer patterning at the 7nm node. In Douglas J. Resnick and Christopher Bencher, editors, *Proceedings of SPIE*, volume 9423, page 942305, mar 2015.

[35] Robert D. Groot and Timothy J. Madden. Dynamic simulation of diblock copolymer microphase separation. *The Journal of Chemical Physics*, 108(20):8713–8724, may 1998.

[36] Robert D. Groot, Timothy J. Madden, and Dominic J. Tildesley. On the role of hydrodynamic interactions in block copolymer microphase separation. *The Journal of Chemical Physics*, 110(19):9739–9749, may 1999.

[37] Robert D. Groot and Patrick B. Warren. Dissipative particle dynamics: Bridging the gap between atomistic and mesoscopic simulation. *The Journal of Chemical Physics*, 107(11):4423–4435, sep 1997.

[38] Guo, Zhang, Wang, Wu, Sun, and Pan. Microphase transitions of block copolymer/homopolymer under shear flow. *Condensed Matter Physics*, 18(2):23801, jun 2015.

[39] Katsumi Hagita, Keizo Akutagawa, Tetsuo Tominaga, and Hiroshi Jinnai. Scattering Patterns and Stress-Strain Relations on Phase-separated ABA Block Copolymers under Uniaxial Elongating Simulations. *Soft Matter*, 15(5):926–936, 2019.

[40] Kyle E. Hart, Lauren J. Abbott, Martin Lísal, and Coray M. Colina. Morphology and molecular bridging in comb- and star-shaped diblock copolymers. *The Journal of Chemical Physics*, 141(20):204902, nov 2014.

[41] Marc A. Hillmyer, Wayne W. Maurer, Timothy P. Lodge, Frank S. Bates, and Kristoffer Almdal. Model bicontinuous microemulsions in ternary homopolymer/block copolymer blends. *Journal of Physical Chemistry B*, 103(23):4814–4824, 1999.

[42] P. J. Hoogerbrugge and J. M.V.A. V. A Koelman. Simulating Microscopic Hydrodynamic Phenomena with Dissipative Particle Dynamics. *Europhysics Letters (EPL)*, 19(3):155–160, jun 1992.

[43] William Humphrey, Andrew Dalke, and Klaus Schulten. VMD – Visual Molecular Dynamics. *Journal of Molecular Graphics*, 14:33–38, 1996.

[44] Su-Mi Hur, Vikram Thapar, Abelardo Ramírez-Hernández, Gurdaman Khaira, Tamar Segal-Peretz, Paulina A. Rincon Delgadillo, Weihua Li, Marcus Müller, Paul F. Nealey, and Juan J. de Pablo. Molecular pathways for defect annihilation in directed self-assembly. *Proceedings of the National Academy of Sciences*, 112(46):14144–14149, nov 2015.

[45] Su-Mi Hur, Vikram Thapar, Abelardo Ramírez-Hernández, Paul F Nealey, and Juan J. de Pablo. Defect Annihilation Pathways in Directed Assembly of Lamellar Block Copolymer Thin Films. *ACS Nano*, page acsnano.8b04202, sep 2018.

[46] Tatsuhiro Iwama, Nabil Laachi, Kris T. Delaney, and Glenn H. Fredrickson. Field-theoretic Simulations of Directed Self-assembly for Contact Multiplication. *Journal of Photopolymer Science and Technology*, 28(5):689–693, 2015.

[47] Tatsuhiro Iwama, Nabil Laachi, Kris T. Delaney, Bongkeun Kim, and Glenn H. Fredrickson. Computational studies of shape rectification in directed self-assembly. In Douglas J. Resnick and Christopher Bencher, editors, *SPIE Advanced Lithography*, volume 9049, page 904927, mar 2014.

[48] Nobuyuki Iwaoka, Katsumi Hagita, and Hiroshi Takano. Estimation of Relaxation Modulus of Polymer Melts by Molecular Dynamics Simulations: Application of Relaxation Mode Analysis. *Journal of the Physical Society of Japan*, 84(4):044801, apr 2015.

[49] Seong-Jun Jeong, Ji Eun Kim, Hyoung-Seok Moon, Bong Hoon Kim, Su Min Kim, Jin Baek Kim, and Sang Ouk Kim. Soft Graphoepitaxy of Block Copolymer Assembly with Disposable Photoresist Confinement. *Nano Letters*, 9(6):2300–2305, jun 2009.

[50] Seong-Jun Jeong, Ju Young Kim, Bong Hoon Kim, Hyoung-Seok Moon, and Sang Ouk Kim. Directed self-assembly of block copolymers for next generation nanolithography. *Materials Today*, 16(12):468–476, dec 2013.

[51] Shengxiang Ji, Lei Wan, Chi-Chun Liu, and Paul F. Nealey. Directed self-assembly of block copolymers on chemical patterns: A platform for nanofabrication. *Progress in Polymer Science*, 54-55:76–127, mar 2016.

[52] Hirokazu Kato, Yuriko Seino, Hiroki Yonemitsu, Hironobu Sato, Masahiro Kanno, Katsutoshi Kobayashi, Ayako Kawanishi, Tsubasa Imamura, Mitsuhiro Omura, Naofumi Nakamura, and Tsukasa Azuma. Sub-30nm via interconnects fabricated using directed self-assembly. *Microelectronic Engineering*, 110:152–155, oct 2013.

[53] Gurdaman Khaira, Manolis Doxastakis, Alec Bowen, Jiaxing Ren, Hyo Seon Suh, Tamar Segal-Peretz, Xuanxuan Chen, Chun Zhou, Adam F. Hannon, Nicola J. Ferrier, Venkatram Vishwanath, Daniel F. Sunday, Roel Gronheid, R. Joseph Kline, Juan J. de Pablo, and Paul F. Nealey. Derivation of Multiple Covarying Material and Process Parameters Using Physics-Based Modeling of X-ray Data. *Macromolecules*, 50(19):7783–7793, oct 2017.

[54] Ho-Cheol Kim, Sang-Min Park, and William D Hinsberg. Block Copolymer Based Nanostructures: Materials, Processes, and Applications to Electronics. *Chemical Reviews*, 110(1):146–177, jan 2010.

[55] Sang Ouk Kim, Harun H Solak, Mark P Stoykovich, Nicola J Ferrier, Juan J De Pablo, and Paul F Nealey. Epitaxial self-assembly of block copolymers on lithographically defined nanopatterned substrates. *Nature*, 424(6947):411–4, 2003.

[56] J M V A Koelman and P J Hoogerbrugge. Dynamic Simulations of Hard-Sphere Suspensions Under Steady Shear. *Europhysics Letters (EPL)*, 21(3):363–368, jan 1993.

[57] Nabil Laachi, Kris T. Delaney, Bongkeun Kim, Su-Mi Hur, Robert Bristol, David Shykind, Corey J. Weinheimer, and Glenn H. Fredrickson. Self-consistent field theory investigation of directed self-assembly in cylindrical confinement. *Journal of Polymer Science Part B: Polymer Physics*, 53(2):142–153, jan 2015.

[58] Nabil Laachi, Tatsuhiro Iwama, Kris T. Delaney, David Shykind, Corey J. Weinheimer, and Glenn H. Fredrickson. Directed self-assembly of linear arrays of block copolymer

cylinders. *Journal of Polymer Science Part B: Polymer Physics*, 53(5):317–326, mar 2015.

[59] Azat Latypov, Moshe Preil, Gerard Schmid, Ji Xu, He Yi, Kenji Yoshimoto, and Yi Zou. Exploration of the directed self-assembly based nano-fabrication design space using computational simulations. In William M. Tong and Douglas J. Resnick, editors, *Alternative Lithographic Technologies V*, volume 8680, page 868013, mar 2013.

[60] Ludwik Leibler. Theory of microphase separation in block copolymers. *Macromolecules*, 13(10):1602–1617, nov 1980.

[61] Ludwik Leibler. Emulsifying effects of block copolymers in incompatible polymer blends. *Makromolekulare Chemie. Macromolecular Symposia*, 16(1):1–17, mar 1988.

[62] Joshua Lequieu, Trenton Koeper, Kris T Delaney, and Glenn H Fredrickson. Extreme Deflection of Phase Boundaries and Chain Bridging in A(BA) n Miktoarm Star Polymers. *Macromolecules*, page acs.macromol.9b02254, jan 2020.

[63] Weihua Li and Marcus Müller. Directed self-assembly of block copolymers by chemical or topographical guiding patterns: Optimizing molecular architecture, thin-film properties, and kinetics. *Progress in Polymer Science*, 54-55:47–75, mar 2016.

[64] Weihua Li and Marcus Müller. Thermodynamics and Kinetics of Defect Motion and Annihilation in the Self-Assembly of Lamellar Diblock Copolymers. *Macromolecules*, 49(16):6126–6138, aug 2016.

[65] Weihua Li, Marcus Müller, and M Marcus. Defects in the Self-Assembly of Block Copolymers and Their Relevance for Directed Self-Assembly. *Annual Review of Chemical and Biomolecular Engineering*, 6(1):187–216, jul 2015.

[66] Weihua Li, Paul F. Nealey, Juan J. De Pablo, and Marcus Müller. Defect removal in the course of directed self-assembly is facilitated in the vicinity of the order-disorder transition. *Physical Review Letters*, 113(16):1–5, 2014.

[67] Weihua Li and Robert A Wickham. Self-Assembled Morphologies of a Diblock Copolymer Melt Confined in a Cylindrical Nanopore. *Macromolecules*, 39(24):8492–8498, 2006.

[68] Weihua Li and Robert A. Wickham. Influence of the Surface Field on the Self-Assembly of a Diblock Copolymer Melt Confined in a Cylindrical Nanopore. *Macromolecules*, 42(19):7530–7536, oct 2009.

[69] Weihua Li, Robert A. Wickham, and Robert A. Garbary. Phase Diagram for a Diblock Copolymer Melt under Cylindrical Confinement. *Macromolecules*, 39(2):806–811, jan 2006.

[70] Alexei E. Likhtman, Sathish K. Sukumaran, and Jorge Ramirez. Linear Viscoelasticity from Molecular Dynamics Simulation of Entangled Polymers. *Macromolecules*, 40(18):6748–6757, sep 2007.

[71] Chi Chun Liu, Eungnak Han, M. Serdar Onses, Christopher J. Thode, Shengxiang Ji, Padma Gopalan, and Paul F. Nealey. Fabrication of lithographically defined chemically patterned polymer brushes and mats. *Macromolecules*, 44(7):1876–1885, 2011.

[72] Chi Chun Liu, Abelardo Ramírez-Hernández, Eungnak Han, Gordon S.W. Craig, Yasuhiko Tada, Hiroshi Yoshida, Huiman Kang, Shengxiang Ji, Padma Gopalan, Juan J. De Pablo, and Paul F. Nealey. Chemical patterns for directed self-assembly of lamellae-forming block copolymers with density multiplication of features. *Macromolecules*, 46(4):1415–1424, feb 2013.

[73] Guoliang Liu, Abelardo Ramírez-Hernández, Hiroshi Yoshida, Kim Nygård, Dillip K Satapathy, Oliver Bunk, Juan J. de Pablo, and Paul F. Nealey. Morphology of Lamellae-Forming Block Copolymer Films between Two Orthogonal Chemically Nanopatterned Striped Surfaces. *Physical Review Letters*, 108(6):065502, feb 2012.

[74] Guoliang Liu, Abelardo Ramírez-Hernández, Hiroshi Yoshida, Kim Nygård, Dillip K Satapathy, Oliver Bunk, Juan J. de Pablo, and Paul F. Nealey. Morphology of Lamellae-Forming Block Copolymer Films between Two Orthogonal Chemically Nanopatterned Striped Surfaces. *Physical Review Letters*, 108(6):065502, feb 2012.

[75] Meijiao Liu, Weihua Li, and Xinping Wang. Order-order transitions of diblock copolymer melts under cylindrical confinement. *The Journal of Chemical Physics*, 147(11):114903, sep 2017.

[76] Nathaniel A. Lynd, Folusho T. Oyerokun, Donal L. O'Donoghue, Dale L. Handlin, and Glenn H. Fredrickson. Design of Soft and Strong Thermoplastic Elastomers Based on Nonlinear Block Copolymer Architectures Using Self-Consistent-Field Theory. *Macromolecules*, 43(7):3479–3486, apr 2010.

[77] Yuansheng Ma, J. Andres Torres, Germain Fenger, Yuri Granik, Julien Ryckaert, Geert Vanderberghe, Joost Bekaert, and James Word. Challenges and opportunities in applying grapho-epitaxy DSA lithography to metal cut and contact/via applications. In Uwe F. W. Behringer, editor, *Proceedings of SPIE*, volume 9231, page 92310T, oct 2014.

[78] Luca Maragliano, Alexander Fischer, Eric Vanden-Eijnden, and Giovanni Ciccotti. String method in collective variables: Minimum free energy paths and isocommittor surfaces. *The Journal of Chemical Physics*, 125(2):024106, 2006.

[79] Luca Maragliano and Eric Vanden-Eijnden. On-the-fly string method for minimum free energy paths calculation. *Chemical Physics Letters*, 446(1-3):182–190, sep 2007.

[80] M W Matsen. Stabilizing New Morphologies by Blending Homopolymer with Block Copolymer. *Physical Review Letters*, 74(21):4225–4228, may 1995.

[81] M W Matsen. Thin films of block copolymer. *The Journal of Chemical Physics*, 106(18):7781–7791, may 1997.

[82] M. W. Matsen. Equilibrium behavior of asymmetric ABA triblock copolymer melts. *The Journal of Chemical Physics*, 113(13):5539, 2000.

[83] M W Matsen and M Schick. Stable and Unstable Phases of a Linear Multiblock Copolymer Melt. *Macromolecules*, 27(24):7157–7163, nov 1994.

[84] M. W. Matsen and R. B. Thompson. Equilibrium behavior of symmetric ABA triblock copolymer melts. *The Journal of Chemical Physics*, 111(15):7139, oct 1999.

[85] Thomas F Miller, Eric Vanden-Eijnden, and David Chandler. Solvent coarse-graining and the string method applied to the hydrophobic collapse of a hydrated chain. *Proceedings of the National Academy of Sciences*, 104(37):14559–14564, sep 2007.

[86] Hiroki Minehara, Louis M. Pitet, Sangwon Kim, R. Helen Zha, E. W. Meijer, and Craig J. Hawker. Branched Block Copolymers for Tuning of Morphology and Feature Size in Thin Film Nanolithography. *Macromolecules*, 49(6):2318–2326, mar 2016.

[87] M. Müller and M. Schick. Bulk and interfacial thermodynamics of a symmetric, ternary homopolymer–copolymer mixture: A Monte Carlo study. *The Journal of Chemical Physics*, 105(19):8885–8901, nov 1996.

[88] Marcus Müller and Kostas Ch Daoulas. Calculating the free energy of self-assembled structures by thermodynamic integration. *The Journal of Chemical Physics*, 128(2):024903, jan 2008.

[89] Marcus Müller, Weihua Li, Juan Carlos Orozco Rey, and Ulrich Welling. Kinetics of directed self-assembly of block copolymers on chemically patterned substrates. *Journal of Physics: Conference Series*, 640(1):012010, sep 2015.

[90] Marcus Müller, Yuliya G. Smirnova, Giovanni Marelli, Marc Fuhrmans, and An-Chang Shi. Transition Path from Two Apposed Membranes to a Stalk Obtained by a Combination of Particle Simulations and String Method. *Physical Review Letters*, 108(22):228103, may 2012.

[91] Florian Müller-Plathe. Reversing the perturbation in nonequilibrium molecular dynamics: An easy way to calculate the shear viscosity of fluids. *Physical Review E*, 59(5):4894–4898, may 1999.

[92] Umang Nagpal, François A. Detcheverry, Paul F. Nealey, and Juan J. De Pablo. Morphologies of linear triblock copolymers from Monte Carlo simulations. *Macromolecules*, 44(13):5490–5497, 2011.

[93] Umang Nagpal, Marcus Müller, Paul F. Nealey, and Juan J. De Pablo. Free energy of defects in ordered assemblies of block copolymer domains. *ACS Macro Letters*, 1(3):418–422, mar 2012.

[94] Cheolmin Park, Joy Y. Cheng, Michael J. Fasolka, Anne M. Mayes, C. A. Ross, Edwin L. Thomas, and Claudio De Rosa. Double textured cylindrical block copolymer domains via directional solidification on a topographically patterned substrate. *Applied Physics Letters*, 79(6):848–850, aug 2001.

[95] Cheolmin Park, Jongseung Yoon, and Edwin L. Thomas. Enabling nanotechnology with self assembled block copolymer patterns. *Polymer*, 44(22):6725–6760, oct 2003.

[96] S. M. Park, Mark P. Stoykovich, Ricardo Ruiz, Ying Zhang, C. T. Black, and P. F. Nealey. Directed Assembly of Lamellae- Forming Block Copolymers by Using Chemically and Topographically Patterned Substrates. *Advanced Materials*, 19(4):607–611, feb 2007.

[97] Amanda J Parker and Jorg Rottler. Entropic network model for star block copolymer thermoplastic elastomers. *Macromolecules*, 2018.

[98] Rajen M. Patel, Stephen F. Hahn, Calvin Esneault, and Selim Bensason. Processing and properties of polyolefin elastomers and fully hydrogenated styrenic block copolymer elastomers. *Advanced Materials*, 12(23):1813–1817, 2000.

[99] Brandon L. Peters, Ben Rathsack, Mark Somervell, Takeo Nakano, Gerard Schmid, and Juan J. De Pablo. Graphoepitaxial assembly of cylinder forming block copolymers in cylindrical holes. *Journal of Polymer Science, Part B: Polymer Physics*, 53(6):430–441, 2015.

[100] Carolyn L. Phillips, Joshua A. Anderson, and Sharon C. Glotzer. Pseudo-random number generation for Brownian Dynamics and Dissipative Particle Dynamics simulations on GPU devices. *Journal of Computational Physics*, 230(19):7191–7201, 2011.

[101] G. T. Pickett, T. A. Witten, and S. R. Nagel. Equilibrium surface orientation of lamellae. *Macromolecules*, 26(12):3194–3199, jun 1993.

[102] Galen T. Pickett and Anna C. Balazs. Equilibrium orientation of confined diblock copolymer films. *Macromolecules*, 30(10):3097–3103, 1997.

[103] Jonathan Raybin, Jiaxing Ren, Xuanxuan Chen, Roel Gronheid, Paul F. Nealey, and S. J. Sibener. Real-Time Atomic Force Microscopy Imaging of Block Copolymer Directed Self Assembly. *Nano Letters*, 17(12):7717–7723, dec 2017.

[104] Jiaxing Ren, Chun Zhou, Xuanxuan Chen, Moshe Dolejsi, Gordon S W Craig, Paulina Alejandra Rincon Delgadillo, Tamar Segal-Peretz, and Paul F Nealey. Engineering the Kinetics of Directed Self-Assembly of Block Copolymers Toward Fast and Defect-Free Assembly. *ACS Applied Materials & Interfaces*, page acsami.8b05247, jun 2018.

[105] Michael Rubinstein and Ralph H. Colby. *Polymer Physics*. 2003.

[106] Ricardo Ruiz, Huiman Kang, François A Detcheverry, Elizabeth Dobisz, Dan S Kercher, Thomas R Albrecht, Juan J de Pablo, and Paul F Nealey. Density Multiplication and Improved Lithography by Directed Block Copolymer Assembly. *Science*, 321(5891):936–939, 2008.

[107] C. Y. Ryu, M. S. Lee, D. A. Hajduk, and T. P. Lodge. Structure and viscoelasticity of matched asymmetric diblock and triblock copolymers in the cylinder and sphere microstructures. *Journal of Polymer Science Part B: Polymer Physics*, 35(17):2811–2823, dec 1997.

[108] Ludwig Schneider and Marcus Müller. Engineering scale simulation of nonequilibrium network phases for battery electrolytes. *Macromolecules*, 52(5):2050–2062, 2019.

[109] Andrew J. Schultz, Carol K. Hall, and Jan Genzer. Obtaining concentration profiles from computer simulation structure factors. *Macromolecules*, 40(8):2629–2632, apr 2007.

[110] Rachel A. Segalman, Alexander Hexemer, and Edward J. Kramer. Edge Effects on the Order and Freezing of a 2D Array of Block Copolymer Spheres. *Physical Review Letters*, 91(19):196101, nov 2003.

[111] Rachel A. Segalman, Alexander Hexemer, and Edward J. Kramer. Effects of Lateral Confinement on Order in Spherical Domain Block Copolymer Thin Films. *Macromolecules*, 36(18):6831–6839, sep 2003.

[112] Rachel A. Segalman, Kathleen E. Schaefer, Glenn H. Fredrickson, Edward J. Kramer, and Sergei Magonov. Topographic Templating of Islands and Holes in Highly Asymmetric Block Copolymer Films. *Macromolecules*, 36(12):4498–4506, jun 2003.

[113] Rachel A. Segalman, H. Yokoyama, and E.J. Kramer. Graphoepitaxy of Spherical Domain Block Copolymer Films. *Advanced Materials*, 13(15):1152–1155, aug 2001.

[114] Yuriko Seino, Hiroki Yonemitsu, Hironobu Sato, Masahiro Kanno, Hikazu Kato, Katsutoshi Kobayashi, Ayako Kawanishi, Tsukasa Azuma, Makoto Muramatsu, Seiji Nagahara, Takahiro Kitano, and Takayuki Toshima. Contact hole shrink process using directed self-assembly. In William M. Tong, editor, *Proceedings of SPIE*, volume 8323, pages 83230Y–83230Y–7, mar 2012.

[115] Weichao Shi, Andrew L. Hamilton, Kris T. Delaney, Glenn H. Fredrickson, Edward J. Kramer, Christos Ntaras, Apostolos Avgeropoulos, Nathaniel A. Lynd, Quentin Demassieux, and Costantino Creton. Aperiodic "Bricks and Mortar" Mesophase: a New Equilibrium State of Soft Matter and Application as a Stiff Thermoplastic Elastomer. *Macromolecules*, 48(15):5378–5384, aug 2015.

[116] Weichao Shi, Nathaniel A. Lynd, Damien Montarnal, Yingdong Luo, Glenn H. Fredrickson, Edward J. Kramer, Christos Ntaras, Apostolos Avgeropoulos, and Alexander Hexemer. Toward Strong Thermoplastic Elastomers with Asymmetric Miktoarm Block Copolymer Architectures. *Macromolecules*, 47(6):2037–2043, mar 2014.

[117] Weichao Shi, Yuichi Tateishi, Wei Li, Craig J. Hawker, Glenn H. Fredrickson, and Edward J. Kramer. Producing Small Domain Features Using Miktoarm Block Copolymers with Large Interaction Parameters. *ACS Macro Letters*, 4(11):1287–1292, nov 2015.

[118] Dong Ok Shin, Bong Hoon Kim, Ju-Hyung Kang, Seong-Jun Jeong, Seung Hak Park, Yong-Hee Lee, and Sang Ouk Kim. One-Dimensional Nanoassembly of Block Copolymers Tailored by Chemically Patterned Surfaces. *Macromolecules*, 42(4):1189–1193, feb 2009.

[119] Timothy W. Sirk, Yelena R. Slizoberg, John K. Brennan, Martin Lisal, and Jan W. Andzelm. An enhanced entangled polymer model for dissipative particle dynamics. *The Journal of Chemical Physics*, 136(13):134903, apr 2012.

[120] N. A. Spenley. Scaling laws for polymers in dissipative particle dynamics. *Europhysics Letters (EPL)*, 49(4):534–540, feb 2000.

[121] M P Stoykovich, M Muller, S O Kim, H H Solak, E W Edwards, J J de Pablo, and P F Nealey. Directed assembly of block copolymer blends into nonregular device-oriented structures. *Science*, 308(5727):1442–1446, 2005.

[122] Mark P. Stoykovich, Huiman Kang, Kostas Ch. Daoulas, Guoliang Liu, Chi-Chun Liu, Juan J. de Pablo, Marcus Muller, and Paul F. Nealey. Directed Self-Assembly of Block Copolymers for Nanolithography: Fabrication of Isolated Features and Essential Integrated Circuit Geometries. *ACS Nano*, 1(3):168–175, oct 2007.

[123] Mark P. Stoykovich and Paul F. Nealey. Block copolymers and conventional lithography. *Materials Today*, 9(9):20–29, sep 2006.

[124] Deepak Sundrani, S. B. Darling, and S. J. Sibener. Guiding Polymers to Perfection: Macroscopic Alignment of Nanoscale Domains. *Nano Letters*, 4(2):273–276, feb 2004.

[125] B. R. Sveinbjornsson, R. A. Weitekamp, G. M. Miyake, Y. Xia, H. A. Atwater, and R. H. Grubbs. Rapid self-assembly of brush block copolymers to photonic crystals. *Proceedings of the National Academy of Sciences*, 109(36):14332–14336, sep 2012.

[126] Q. Tang, J. Tang, and M. Müller. Process-directed self-assembly of multiblock copolymers: Solvent casting vs spray coating. *European Physical Journal: Special Topics*, 225(8-9):1785–1803, 2016.

[127] Christina L Ting, Daniel Appel, and Zhen-Gang Wang. Minimum Energy Path to Membrane Pore Formation and Rupture. *Physical Review Letters*, 106(16):168101, apr 2011.

[128] R. Tiron, a. Gharbi, M. Argoud, X. Chevalier, J. Belledent, P. Pimmenta Barros, C. Navarro, G. Cunge, S. Barnola, L. Pain, M. Asai, and C. Pieczulewski. The potential of block copolymer's directed self-assembly for contact hole shrink and contact multiplication. *Proc. of SPIE*, 8680(November):868012–868012–11, mar 2013.

[129] R. Tiron, A. Gharbi, P. Pimenta Barros, S. Bouanani, C. Lapeyre, S. Bos, A. Fouquet, J. Hazart, X. Chevalier, M. Argoud, G. Chamiot-Maitral, S. Barnola, C. Monget, V. Farys, S. Berard-Bergery, L. Perraud, C. Navarro, C. Nicolet, G. Hadziioannou, and G. Fleury. Template affinity role in CH shrink by DSA planarization. In Douglas J. Resnick and Christopher Bencher, editors, *Proceedings of SPIE*, volume 9423, page 942317, mar 2015.

[130] J. Andres Torres, Kyohei Sakajiri, David Fryer, Yuri Granik, Yuansheng Ma, Polina Krasnova, Germain Fenger, Seiji Nagahara, Shinichiro Kawakami, Benjamen Rathsack, Gurdaman Khaira, Juan de Pablo, and Julien Ryckaert. Physical verification and manufacturing of contact/via layers using grapho-epitaxy DSA processes. *Proceedings of SPIE*, 9053:90530R, mar 2014.

[131] Eric Vanden-Eijnden and Maddalena Venturoli. Revisiting the finite temperature string method for the calculation of reaction tubes and free energies. *The Journal of Chemical Physics*, 130(19):194103, may 2009.

[132] Mihail Vladkov and Jean-Louis Barrat. Linear and Nonlinear Viscoelasticity of a Model Unentangled Polymer Melt: Molecular Dynamics and Rouse Modes Analysis. *Macromolecular Theory and Simulations*, 15(3):252–262, apr 2006.

[133] Newell R. Washburn, Timothy P. Lodge, and Frank S. Bates. Ternary polymer blends as model surfactant systems. *Journal of Physical Chemistry B*, 104(30):6987–6997, 2000.

[134] A. Werner, F. Schmid, and M. Müller. Monte Carlo simulations of copolymers at homopolymer interfaces: Interfacial structure as a function of the copolymer density. *The Journal of Chemical Physics*, 110(11):5370–5379, mar 1999.

[135] Akihisa Yoshida, Kenji Yoshimoto, and Masahiro Ohshima. Effect of wall potential on morphology of symmetric diblock copolymers in nanotrench. *Japanese Journal of Applied Physics*, 55(6S1):06GE01, jun 2016.

[136] Todd R. Younkin, Roel Gronheid, Paulina Rincon Delgadillo, Boon Teik Chan, Nadia Vandenbroeck, Steven Demuynck, Ainhoa Romo-Negreira, Doni Parnell, Kathleen Nafus, Shigeru Tahara, and Mark Somervell. Progress in directed self-assembly hole shrink applications. In Mark H. Somervell, editor, *Advances in Resist Materials and Processing Technology XXX*, volume 8682, page 86820L, mar 2013.

[137] Bin Yu, Pingchuan Sun, Tiehong Chen, Qinghua Jin, Datong Ding, Baohui Li, and An-Chang Shi. Confinement-Induced Novel Morphologies of Block Copolymers. *Physical Review Letters*, 96(13):138306, apr 2006.

[138] Mingfu Zhang, Markus Drechsler, and Axel H. E. Müller. Template-Controlled Synthesis of Wire-Like Cadmium Sulfide Nanoparticle Assemblies within Core-Shell Cylindrical Polymer Brushes. *Chemistry of Materials*, 16(3):537–543, feb 2004.